WARSAW UNIVERSITY OF TECHNOLOGY

DISCIPLINE OF SCIENCE – PHYSICAL SCIENCES/
FIELD OF SCIENCE – NATURAL SCIENCES

# Ph.D. Thesis

Wojciech Bryliński, M.Sc.

**Study of $K^0_S$ Meson Production in Central Ar+Sc Collisions at SPS Energies**

Supervisor
Professor Katarzyna Grebieszkow, Ph.D., D.Sc.

WARSAW 2023

## Acknowledgments

*I would like to express my enormous gratitude to my supervisor Katarzyna Grebieszkow for a huge amount of work she has done to guide me along the analysis process and preparation of this thesis.*

*This thesis could not be completed without the wonderful NA61/SHINE Collaboration. I am very grateful to all of my colleagues for many discussions during the official and non-official meetings. Special thanks to Marek Gaździcki, Seweryn Kowalski and the whole V0 team for a lot of valuable advice.*

*I wish to thank all friends I met at the Faculty of Physics as well as during my stay at CERN. Thank you for many lunches and coffees we had together. I would like to thank the NA61/SHINE group at the Warsaw University of Technology, especially Justyna Cybowska for sharing the struggles of studies.*

*It was a great experience to contribute to the NA61/SHINE upgrade, developing the data acquisition software. Especially, I would like to thank Oskar Wyszyński, Piotrek Podlaski, Darek Tefelski and Giovanna Lehmann Miotto (and the whole DT-DI section at CERN). Working on such an exciting project and putting everything together for the first data-taking will be an unforgettable experience.*

*Last but not least, I would like to thank my parents and my brothers (Piotr, Paweł, Krzysztof and Łukasz) for the support. I am the most lucky person in the world to have such a great fiancée as Ania Kawęcka. Thank you for being my inspiration and the most supportive person in my life.*

*Dla Ani*

## Abstract

"Study of $K^0_S$ meson production in central Ar+Sc collisions at SPS energies"

This thesis presents the results of the analysis of $K^0_S$ meson production in central Ar+Sc collisions at the SPS energies. The data has been recorded by the NA61/SHINE experiment located at CERN. The analysis was performed on the data from collisions of $^{40}$Ar ion beam with $^{45}$Sc target at two different beam momenta (per nucleon): $40A$ GeV/$c$ and $75A$ GeV/$c$. The production of $K^0_S$ mesons in Ar+Sc collisions was never studied before.

The $K^0_S$ mesons are neutral particles and can be studied by the analysis of the charged decay products that can be detected. The most abundant decay channel of $K^0_S$ with branching ratio of 69.2% is the decay into a pair of charged pions. The presented analysis is based on the reconstruction of invariant mass of pairs of particles that are assumed to be candidates for decay products. The obtained results were corrected for the detection and reconstruction inefficiencies using simulated data.

The main results of this thesis are the double-differential spectra in rapidity and transverse momentum space. The good quality of the analysis was confirmed by reconstruction of the lifetime of $K^0_S$ and comparison with tabulated value. The obtained results on $K^0_S$ production were compared with the results on the charged kaon production. This comparison revealed a large, unexpected isospin symmetry breaking effect that was never discussed before. The results were also compared with various theoretical models as well as available world data.

The study of the strange particles is the main point of the NA61/SHINE strong interactions programme. The experiment has undergone a major upgrade during the Long Shutdown 2 at CERN. It allows for tenfold increase of the data-taking rate. The better quality, high-statistics data of different ion collisions at different energies will shed more light on the discovered effect of large isospin symmetry breaking.

Key words: $K^0_S$, strangeness, isospin, high-energy heavy-ion collisions, physics, NA61/SHINE, CERN

## Streszczenie

*(abstract in Polish)*


„Badanie produkcji mezonów $K^0_S$ w centralnych zderzeniach Ar+Sc przy energiach akceleratora SPS”

Niniejsza rozprawa doktorska przedstawia wyniki analizy produkcji mezonów $K^0_S$ w centralnych zderzeniach Ar+Sc przy energiach akceleratora SPS. Dane zostały zebrane przez eksperyment NA61/SHINE w ośrodku badawczym CERN. Analiza została przeprowadzona na danych pochodzących ze zderzeń wiązki jonów $^{40}$Ar z tarczą $^{45}$Sc przy dwóch pędach wiązki (na nukleon): 40$A$ GeV/$c$ oraz 75$A$ GeV/$c$. Produkcja mezonów $K^0_S$ w zderzeniach Ar+Sc została zbadana po raz pierwszy.

Mezony $K^0_S$ to cząstki neutralne, które mogą być badane poprzez detekcję naładowanych produktów ich rozpadu. Najbardziej faworyzowany kanał rozpadu mezonów $K^0_S$ to rozpad na dwa naładowane piony. Przedstawiona analiza bazuje na rekonstrukcji masy niezmienniczej dla par cząstek, które uznane zostały za kandydatów na produkty rozpadów. Otrzymane wyniki zostały poprawione na wydajność detekcji i rekonstrukcji z użyciem danych symulowanych.

Głównym wynikiem niniejszej pracy doktorskiej są dwuwymiarowe (podwójnie różniczkowe) widma krotności mezonów $K^0_S$ wyznaczone w funkcji pośpieszności oraz pędu poprzecznego. Jakość przeprowadzonej analizy została potwierdzona przez zrekonstruowanie czasu życia mezonów $K^0_S$ i potwierdzenie zgodności z wartością stabularyzowaną. Otrzymane wyniki produkcji mezonów $K^0_S$ zostały także porównane z produkcją kaonów naładowanych. Porównanie to wykazało niespodziewane, duże łamanie symetrii izospinu. Wyniki zostały także porównane z wybranymi modelami teoretycznymi oraz z dostępnymi wynikami eksperymentalnymi.

Badanie cząstek dziwnych wpisuje się w główną część programu fizycznego eksperymentu NA61/SHINE, dotyczącą badania oddziaływań silnych. Eksperyment przeszedł gruntowną modernizację podczas tzw. Long Shutdown 2 w ośrodku badawczym CERN. Modernizacja pozwoliła na dziesięciokrotne zwiększenie szybkości zbierania danych. Wyższa statystyka danych lepszej jakości, pochodzących ze zderzeń różnych systemów przy różnych energiach, pozwoli na bardziej precyzyjne zbadanie odkrytego scenariusza dużego łamania symetrii izospinu.



Słowa kluczowe: $K^0_S$, dziwność, izospin, wysokoenergetyczne zderzenia ciężkich jonów, fizyka, NA61/SHINE, CERN

# Contents

Chapter 1

# Introduction

## 1.1 Standard Model

Standard Model (SM) [1] is a quantum field theory which describes the elementary particles and the interactions between them. It was developed in the 20th century as the result of work of many scientists. The majority of the phenomena predicted by the SM have been confirmed experimentally, including the discovery of the Higgs boson.

Standard Model assumes the existence of elementary constituents of matter (fermions), and carriers of the interactions (bosons). The overall summary of all particles including their mass, electric charge and spin is presented in Fig. 1.1.

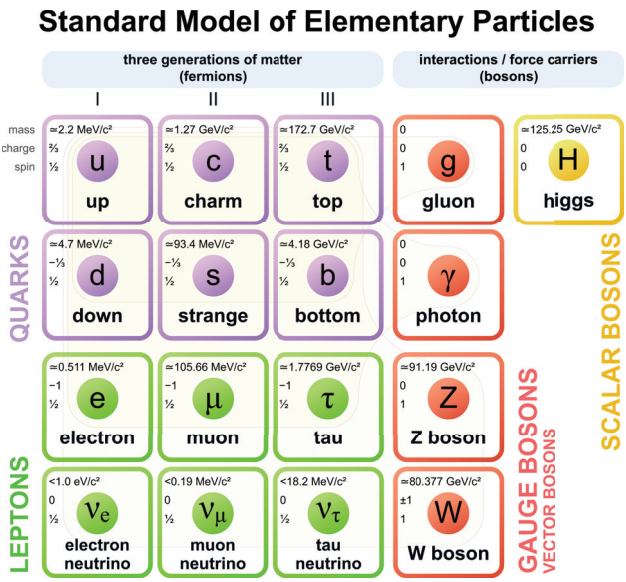


**Figure 1.1:** Table of all elementary particles included in Standard Model. Figure from Ref. [2]. Values based on Ref. [3].

The group of fermions consists of 6 quarks: up – $u$, down – $d$, charm – $c$, strange – $s$, top/true – $t$, bottom/beauty – $b$, and 6 leptons: electron – $e$, electron neutrino – $\nu_e$, muon – $\mu$, muon neutrino – $\nu_\mu$, tau – $\tau$, tau neutrino – $\nu_\tau$. Fermions are divided into three families/generations (I, II, III in Fig. 1.1), each containing two quarks and two leptons. Each fermion has a correspond-

ing anti-particle with an opposite electric charge and baryon or lepton number. Stable matter in the Universe is built out of particles from the first family. In normal conditions quarks are confined into hadrons. Hadrons consist of *valence* quarks which determine the quantum numbers of hadrons and infinite number of *sea* quarks that are constantly being created and destroyed and do not change the quantum numbers of hadrons. Hadrons which are built out of three valence quarks are called baryons (qqq or $\overline{\mathrm{qqq}}$) and these built out of two valence quarks (quark and anti-quark) are called mesons ($\mathrm{q\bar{q}}$). Recent discoveries at the Large Hadron Collider (LHC) at the European Organization for Nuclear Research (CERN) confirm the existence of particles built out of four valence quarks (tetraquarks) and five valence quarks (pentaquarks) [3, 4].

Standard Model explains three fundamental interactions: strong, weak and electromagnetic. Every interaction is defined as the exchange of proper interaction carriers called bosons. The electromagnetic interaction is carried by photons – $\gamma$. Bosons $W^+$, $W^-$, and $Z^0$ are responsible for the weak interactions and gluons are the carriers of the strong interactions. Additionally, the SM predicts the existence of one scalar boson – Higgs boson. It is responsible for the mass of elementary particles.

The nature of the strong interactions is explained in the Standard Model within Quantum Chromodynamics (QCD). It assumes that quarks and gluons carry the strong charge which is called colour. Quarks can carry one out of tree colours (red, green, blue) or three anti-colours for anti-quarks. The potential of the strong interaction increases with the distance between the interacting particles. When trying to separate two strongly interacting particles, at some point the accumulated energy is high enough to produce another $\mathrm{q\bar{q}}$ pair. Thus, it is not possible to separate two quarks. This effect is called quark confinement and is schematically presented in Fig. 1.2. On the other hand, when quarks are extremely squeezed, the strong interaction becomes negligible and quarks behave like quazi-free particles. This effect is called asymptotic freedom.

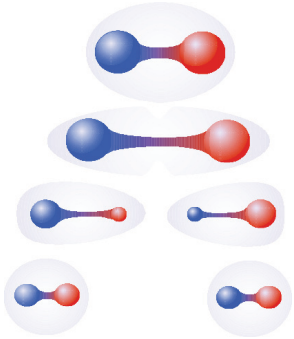

**Figure 1.2:** Schematic picture of confinement effect. Figure from Ref. [5].

The Standard Model is believed to be the most reliable particle physics theory. However, it is not complete. It does not explain the gravitational interaction, nor the dark matter or dark energy. Moreover, in SM neutrinos are assumed to be massless whereas there is an evidence of their

mixing [6]. In addition, it has at least 19 free parameters for which the values are not predicted and have to be measured (e.g. the particle masses).

## 1.2 Quark-gluon plasma

Quark-gluon plasma (QGP) is a state of matter in which partons (quarks and gluons) can move freely. It is believed that such a state was present at the very beginning of the existence of the Universe, right after the Big Bang. When expanding, the matter cooled down and quark-gluon plasma hadronized creating hadrons and then freezed-out. The QGP state can be created in laboratory when the energy density is high enough. The proper conditions can be obtained during heavy-ion collisions at sufficiently high energies. The production of QGP was confirmed in heavy-ion collisions at CERN [7, 8] and Brookhaven National Laboratory (BNL) [9].

### 1.2.1 Heavy-ion collisions

High-energy particle collisions are a unique tool which allows to study the basic constituents of matter and the interactions between them. At first, the particles (electrons, hadrons or ions) are accelerated to the velocities close to the speed of light. Then, they are smashed into each other (collider experiments) or against a target (fixed-target experiments). The schematic picture of the collision is shown in Fig. 1.3. Depending on the distance between the centers of colliding nuclei in the transverse plane, which is called impact parameter ($b$ in the presented Fig. 1.3), the collision can be central for small impact parameter values or peripheral for higher impact parameter values. Nucleons which do not interact with each others are named spectators, whereas nucleons that interact (elastically and/or inelastically) are called participants. Participants which interact inelastically are named wounded nucleons. The numbers for each type of particles (spectators, participants and wounded nucleons) vary between collisions, depending on the centrality.

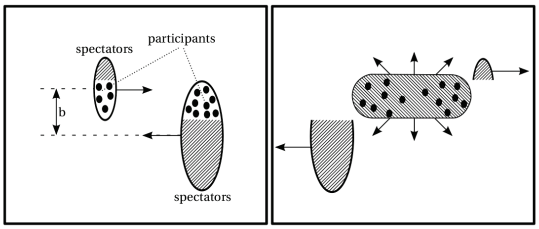


**Figure 1.3:** Schematic picture of inelastic ion-ion collision. Figure from Ref. [10].

The space-time evolution of the high-energy heavy-ion collision is presented in Fig. 1.4. Two scenarios are taken into account: with and without quark-gluon plasma production. For the first scenario, right after the collision, the non-equilibrium state is created. The matter thermalises and QGP is formed. System expands and cools down. At some point the hadronization occurs and quarks and gluons merge into hadrons. The created hadrons can still interact elastically

and inelastically. The moment when hadrons stop interacting inelastically is called chemical freeze-out. Although the chemical composition of the system is fixed in the moment of chemical freeze-out, the produced particles can still exchange their momenta. When the kinetic (thermal) freeze-out occurs, the momenta of all particles are fixed. Such particles can be registered in the detectors of high-energy experiments. In the scenario without QGP formation, a hot and dense hadron gas is formed after collision. It freezes-out to the particles that can be measured.

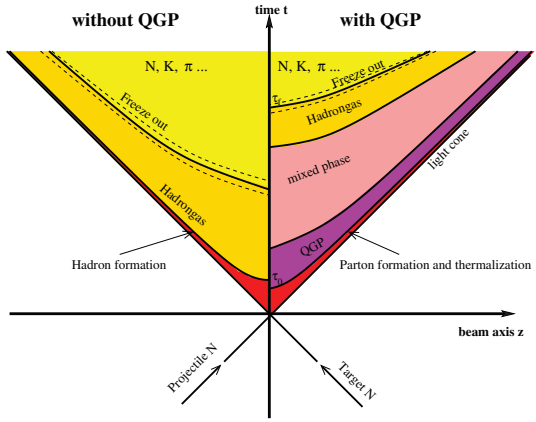


**Figure 1.4:** Space-time evolution of heavy-ion collision. Figure from Ref. [11].

### 1.2.2 Signatures of quark-gluon plasma

The research on quark-gluon plasma properties is the main motivation of all experiments dedicated to study the high-energy heavy-ion collisions. However, it is not possible to measure QGP directly due to its extremely high temperature and energy density as well as very short lifetime ($\sim 10^{-23}$ s). The heavy-ion experiments are technically able to register only the particles after kinetic freeze-out. Thus, a set of observables, so-called QGP signatures, was established. They are poorly sensitive to hadronization and can provide the information about QGP properties. The most popular QGP signatures are:

- strangeness enhancement [12] – Strangeness is a property of particles expressed as a quantum number. In high-energy collisions strangeness is measured as a number of strange hadrons. Due to strangeness conservation in strong interactions, the production of $s$ quark is always associated with the production of $\overline{s}$ quark. In two phases of matter – QGP and hadron gas (HG) – the strangeness carriers are different. In QGP, strangeness is carried by strange and anti-strange quarks whereas in HG, the most abundant strangeness carriers are kaons, which are the lightest strange hadrons. Thus, to produce one pair of strange carriers in HG, one needs more energy in comparison to QGP ($2M_{kaon} \approx 2 \cdot 500$ MeV, $2m_s \approx 2 \cdot 100$ MeV). In addition, comparing to the temperature of the phase transition ($T_c \approx 150$ MeV at baryochemical potential $\mu_B = 0$ [13, 14]), strange quarks are considered to be light par-

ticles, whereas kaons are heavy. Due to its properties, strangeness production is sensitive to the phase transition between hadron gas and quark-gluon plasma and is expected to be enhanced in QGP scenario.

- jet quenching [15] – Jets are collimated streams of particles produced by the hadronization of high-energy quark or gluon. Jets that are produced in pairs moving in the opposite directions are called di-jets. When such pair of jets is produced close to the surface of QGP, one jet has to propagate through the QGP. The propagation through very dense medium, causes the significant quenching of one of the jets.
- charmonia suppresion [16] – Charmonia are the particles that contain charm and anti-charm quarks. The lightest charmonium is the $J/\psi$ meson. When the $c\bar{c}$ pair is produced in the QGP, the strong interaction between charm and anti-charm quarks is screened by the medium. Thus, it is less probable for charm and anti-charm quarks to stay bounded. As a result, the suppression of charmonia production in the QGP scenario is expected.
- elliptic flow [17, 18] – Flow is a fluid-like expansion of the dense matter created after the collision. In non-central collisions, the initial spatial anisotropy transfers to the anisotropic flow of the matter and thus the anisotropy in the momentum space. The anizotropy can be measured by the Fourier coefficients of the azimuthal angle distributions. The second Fourier coefficient – $v_2$ measures the elliptic flow. The $v_2$ coefficient scales with the number of constituent quarks (three for baryons and two for mesons) in the QGP scenario. It means that the matter flows already on the level of quarks and gluons which is considered as the signature of the QGP formation.

### 1.2.3 Phase diagram of strongly interacting matter

Quark-gluon plasma and hadron gas are the two known phases of the strongly interacting matter. They can be visualised on the phase diagram, which determines the phase that is expected under defined conditions. The phase diagram of strongly interacting matter is usually presented as a two-dimentional plot with temperature on the $y$-axis and baryochemical potential on the $x$-axis ($T$–$\mu_B$ coordinate system). The baryochemical potential characterises the asymmetry between baryons and anti-baryons. Higher value of $\mu_B$ means bigger asymmetry between produced matter and anti-matter. The visualisation of the phase diagram of strongly interacting matter is presented in Fig. 1.5. For low temperatures and low values of baryochemical potential the hadron gas phase is expected. When increasing $T$ and/or $\mu_B$, the phase transition to quark-gluon plasma occurs. The character of the phase transition is still under discussion. The most popular approach predicts the first-order phase transition for higher baryochemical values. When decreasing $\mu_B$, the phase transition changes the character to cross-over with the continuous (but rapid) change of physical parameters. The first-order phase transition line is expected to end up with a critical point (CP). The experimental confirmation of the CP would verify the phase diagram predictions, however, at the time of writing this thesis, there are no consistent results proving the discovery of the critical point.

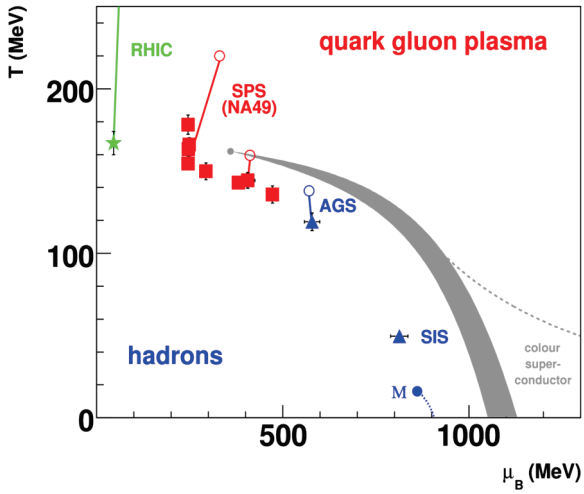


**Figure 1.5:** Phase diagram of strongly interacting matter. Gray band corresponds to first-order phase transition finished by critical point. Closed points correspond to chemical freeze-out and open points to hypothetical points of early stage of collision. Figure from Ref. [19].

## 1.3 Strangeness carriers

The lightest strangeness carrying hadrons are kaons [3]. Kaons are the bound states of strange (or anti-strange) quark and up or down anti-quark (or quark). There are four types of kaons:

- $\mathrm{K}^+$ – contains strange anti-quark and up quark ($u\bar{s}$), positively charged
- $\mathrm{K}^-$ – contains strange quark and up anti-quark ($\bar{u}s$), negatively charged
- $\mathrm{K}^0$ – contains strange anti-quark and down quark ($d\bar{s}$), neutrally charged
- $\overline{\mathrm{K}^0}$ – contains strange quark and down anti-quark ($\bar{d}s$), neutrally charged

Although the neutrally charged kaons are usually produced via the strong interactions, they decay weakly. The $\mathrm{K}^0$ meson has two weak eigenstates, differentiated by their lifetime: $\mathrm{K}^0_\mathrm{S}$ (short-lived) and $\mathrm{K}^0_\mathrm{L}$ (long-lived) [20]:

$$|\mathrm{K}^0_\mathrm{S}\rangle = \frac{|\mathrm{K}^0\rangle + |\overline{\mathrm{K}^0}\rangle}{\sqrt{2}},$$
$$|\mathrm{K}^0_\mathrm{L}\rangle = \frac{|\mathrm{K}^0\rangle - |\overline{\mathrm{K}^0}\rangle}{\sqrt{2}}.$$

The mass of the $\mathrm{K}^0_\mathrm{S}$ meson is equal to $497.611 \pm 0.013$ MeV [3]. Its mean lifetime is $\tau = (0.8954 \pm 0.0004) \cdot 10^{-10}$ s [3], which gives $c\tau = 2.6844$ cm. The most abundant decay channel of the $\mathrm{K}^0_\mathrm{S}$ mesons is the decay into a pair of charged pions (with the branching ratio of 69.2%): $\mathrm{K}^0_\mathrm{S} \to \pi^+ + \pi^-$.

## 1.4 Production of kaons

According to statistical approach, in the high-energy collisions one expects equal production of $u$ ($\overline{u}$) and $d$ ($\overline{d}$) quarks (anti-quarks). This is because the difference between their (small) masses is judged insignificant with respect to the collision energy. In nucleus-nucleus reactions, the two colliding nuclei are made of two types of nucleons: protons, made of two up and one down valence quarks ($uud$), and neutrons, made of one up and two down valence quarks ($udd$). When the number of protons and neutrons in the two nuclei is comparable, the number of created mesons containing $u$ and $d$ quarks, and $\overline{u}$ and $\overline{d}$ anti-quarks, should be closely equal.

The reasoning presented above goes in line with the concept of *isospin symmetry* [21, 22] (equivalence of physical phenomena occurring for $u$ and $d$ quarks, or corresponding anti-quarks) in the theory of strong interactions, QCD. It is also supported by quantitative predictions of *statistical models*. Finally, it also reflects in numerous other phenomenological models available in the field, up to the point of being considered a universal rule for particle production phenomena in the high-energy domain.

The rule of equal production of $u$ and $d$ quarks implies the following rule for the multiplicities (number of particles per event) of produced kaons [22, 23, 24]:

$$\mathrm{K}^+ + \mathrm{K}^- = \mathrm{K}^0 + \overline{\mathrm{K}^0}. \tag{1.1}$$

The above equation can also be derived from Smushkevich rule: “For all particle involved in isospin-conserving relation all members of isospin multiplets are produced in equal numbers if and only if the initial population is uniform” [25, 21, 26]. The kaons form two isospin doublets: $\mathrm{K}^+$ – $\mathrm{K}^0$ and $\mathrm{K}^-$ – $\overline{\mathrm{K}^0}$, therefore for isospin symmetric initial states the multiplicities should follow the equations:

$$\begin{aligned} \mathrm{K}^+ &= \mathrm{K}^0, \\ \mathrm{K}^- &= \overline{\mathrm{K}^0}. \end{aligned} \tag{1.2}$$

By summing up the Eq. (1.2) one gets Eq. (1.1).

The $\mathrm{K}^0$ and $\overline{\mathrm{K}^0}$ mesons are not directly measured in detectors, since the physical neutral states are the $\mathrm{K}^0_\mathrm{S}$ and $\mathrm{K}^0_\mathrm{L}$. The production of $\mathrm{K}^0_\mathrm{S}$ is given by [27, 22, 23, 24]:

$$\mathrm{K}^0_\mathrm{S} = \frac{\mathrm{K}^0 + \overline{\mathrm{K}^0}}{2}. \tag{1.3}$$

Thus, one can estimate the $\mathrm{K}^0_\mathrm{S}$ production to be the mean production of charged kaons:

$$\mathrm{K}^0_\mathrm{S} = \frac{\mathrm{K}^+ + \mathrm{K}^-}{2}. \tag{1.4}$$

The deviation from the above equation can be interpreted as the violation of isospin symmetry.

## 1.5 Armenteros-Podolanski plot

In heavy-ion experiments, the neutral strange particles can be studied via the analysis of the decay products (daughter particles). One of the ways to verify what type of neutral particle was reconstructed is the Armenteros-Podolanski plot [28]. It is a two-dimensional distribution of Armenteros transverse momentum $p_T^{Arm}$ and longitudinal momentum asymmetry $\alpha^{Arm}$ of oppositely charged decay products. The variables used in the formulas are explained in the left panel of Fig. 1.6. The variables are calculated in the local coordinate system of decaying particle (neutral hadron rest frame). The $p_T^{Arm}$ is defined as a daughter particle momentum component transverse to the decaying neutral particle momentum (variables defined in the left panel of Fig. 1.6):

$$p_T^{Arm} = p^{+/-} \cdot \sin(\varphi^{+/-}). \tag{1.5}$$

The $\alpha^{Arm}$ can be calculated from the following formula:

$$\alpha^{Arm} = \frac{p_L^+ - p_L^-}{p_L^+ + p_L^-}. \tag{1.6}$$

The possible values of $p_T^{Arm}$ and $\alpha^{Arm}$ for the daughter particles draw half ellipses on the Armenteros-Podolanski plot with a center defined by the daughter particle mass difference. For $K_S^0$ mesons decaying into two pions: $K_S^0 \to \pi^+ + \pi^-$ the mass difference is zero, thus the ellipse is centered at 0. The theoretical values of $p_T^{Arm}$ and $\alpha^{Arm}$ for strange neutral particle decays are shown in the right panel of Fig. 1.6.

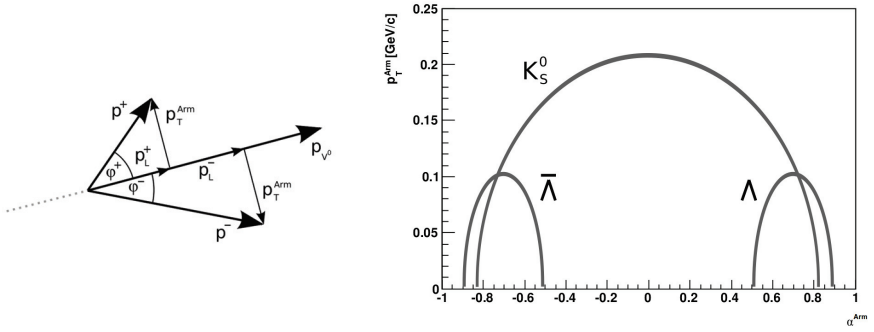


**Figure 1.6:** *Left*: Definition of variables used to calculate $p_T^{Arm}$ and $\alpha^{Arm}$. *Right*: Theoretically allowed $p_T^{Arm}$ and $\alpha^{Arm}$ values for strange neutral particles. Figures from Ref. [29].

## 1.6 Onset of deconfinement

The beginning of the quark-gluon plasma formation is called *onset of deconfinement*. The experimental studies of this phenomena were motivated by the predictions of the Statistical Model of

the Early Stage (SMES) [30]. It predicted several signatures of the phase transition which were observed at first by the NA49 experiment [31] and later confirmed by STAR [32]. The signatures as well as the details of the SMES model are discussed in the following subsections.

### 1.6.1 Statistical Model of the Early Stage

SMES decribes the early stages of the relativistic nucleus-nucleus collisions. It is based on the assumption, that the production of new particles at the early stage of the collisions is fully statistical process. It means that all microscopic states allowed by conservation laws are equally probable. At the end, the maximum entropy equilibrium state is always created. Moreover, the production of matter at the early stage of the collision is defined by the available energy and volume. However, only a fraction of the total available energy is transformed into the energy of new degrees of freedom (new particles), as the other part is carried by the net baryons escaping the collision region.

SMES assumes the existance of the two phases of the strongly-interacting matter: hadron gas which is confined state and quark-gluon plasma which is deconfined state. The formation of the mixed state is also possible, depending on which configuration gives the maximum entropy. In the confined state the ideal gas equation is used to describe the properties of equilibrated matter. The non-strange particles are assumed to be massless bosons. They dominate the entropy production. The mass of the strange particles is assumed to be equal to 500 MeV, which is the mass of kaon – the most abundant strange meson. In the deconfined state, the "bag model" equation of state [33] is used to describe the matter in equilibrium. This state is composed out of gluons, $u$, $d$, $s$ quarks and their anti-quarks. The contribution from the heavier quarks is neglected due to their large masses. The non-strange quarks and gluons are assumed to be massless and the strange quark mass is equal to 175 MeV.

In the SMES model, the early-stage created matter expands, hadronizes and freezes-out. The total entropy and the number of strange quarks and anti-quarks is postulated to be (approximately) conserved. Moreover, the number of internal degrees of freedom is significantly higher in QGP in comparison to the HG. Thus, depending on which phase was present at the early stage of the collision, the differences in the properties of the produced particles are expected.

### 1.6.2 Signatures of the onset of deconfinement

The SMES model predicts several signatures of the onset of deconfinement. The most important ones are presented in Fig. 1.7. The top row shows the model predictions and bottom row shows the corresponding experimental results.

The left column in the Fig. 1.7 shows the *kink* structure. The structure is revealed in the energy dependence of the ratio of the total entropy to the number of nucleons participating in the collision. This ratio is expected to be a linear function of the Fermi energy with the slope proportional to the number of effective degrees of freedom $g^{1/4}$. As in the QGP phase SMES

assumes higher number of degrees of freedom, the dependency is steeper for the QGP state. The entropy produced in the early stage is proportional to the multiplicity of produced pions. Thus, by measuring the mean pion production (divided by the mean number of wounded nucleons), the *kink* structure was experimentally confirmed in central Pb+Pb collisions (bottom left plot in Fig. 1.7).

The middle column of Fig. 1.7 presents the *step* structure. SMES predicts the linear increase of the temperature with the energy of the collisions for pure HG and QGP states. However, in the mixed phase, the temperature is supposed to be constant and equal to the temperature of the phase transition. In the experiment, the temperature can be estimated from the exponentially-shaped transverse mass spectra [(a)]. In fact, the inverse slope parameter of the spectrum corresponds to kinetic freeze-out temperature plus additional component related to the transverse flow velocity of the system. The energy dependence of the inverse slope parameter of positively charged kaons measured in the Pb+Pb and Au+Au collisions at mid-rapidity [(b)] (presented in the bottom middle plot in Fig. 1.7) confirms the *step* structure.

The most spectacular structure predicted by SMES as the signature of the onset of deconfinement is called *horn*. It is shown in the right column of Fig. 1.7. The structure is present in the strangeness to entropy ratio. SMES predicts a steep increase of this ratio when increasing the collision energy for the HG state. At the onset of deconfinement, the ratio starts to drop and then saturates and slightly increases in the QGP state. The *horn* structure can be measured experimentally in the $K^+/\pi^+$ ratio which is proportional to the ratio of strangeness to entropy. It was observed in the Pb+Pb and Au+Au collisions (see the bottom right plot in Fig. 1.7).

## 1.7 Onset of fireball

*Onset of fireball* is the beginning of creation of large clusters of strongly interacting matter when increasing the size of the colliding system [37]. Experimentally, it can be observed as a rapid change of particle production characteristics when going from small to intermediate and big systems, for example a sudden increase of the strangeness production when increasing the size of the colliding system. This phenomenon was observed for the first time by the NA61/SHINE experiment. The example results are presented in Fig. 1.8 and compared with different dynamical (left) and statistical (right) models. The plot reveals the sudden increase of $K^+/\pi^+$ with the size of the colliding system which is not reproduced by any of the models. The dynamical models

[(a)] Transverse mass of the particle can be calculated (assuming $c \equiv 1$) from the following formula: $m_T = \sqrt{p_T^2 + m_0^2}$, where $p_T$ is the transverse momentum (momentum of the particle in the plane perpendicular to the beam axis) and $m_0$ is the particle rest mass.

[(b)] Rapidity is defined as: $y = \frac{1}{2} \ln \left( \frac{E+p_L}{E-p_L} \right)$, where $E$ and $p_L$ are total energy and longitudinal momentum (momentum of the particle along the beam axis), respectively ($c \equiv 1$ is assumed). The phase space corresponding to rapidity values close to 0 ($y = 0$) in the collision center-of-mass reference system (CMS) is called mid-rapidity. The regions of positive ($y > 0$) and negative ($y < 0$) rapidity are called forward and backward rapidity regions, respectively. The rapidity values used in this thesis are calculated in the collision CMS.

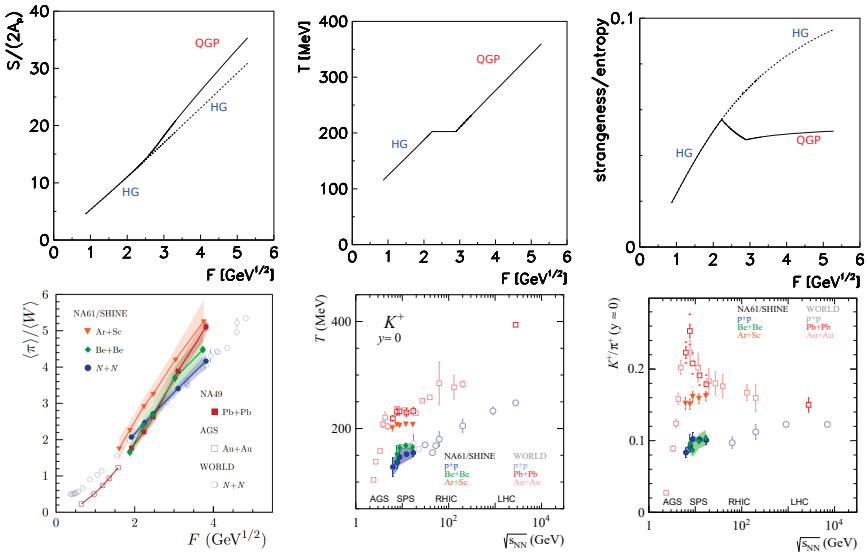


**Figure 1.7:** *Top row*: Signatures of phase transition predicted by SMES. *Bottom row*: Experimental results corresponding to presented signatures. *Left*: enhancement of entropy production (kink), *Middle*: plateau in inverse slope parameter (step) measured at mid-rapidity, *Right*: non-monotonic behaviour of strangeness to entropy production ratio (horn) measured at mid-rapidity. Signatures are displayed as collision energy dependence ($F \approx \sqrt[4]{s_{NN}}$ in SPS energy range; $\sqrt{s_{NN}}$ denotes available energy in collision center-of-mass system per nucleon pair). Figures from Refs. [30, 34, 35, 36].

that do not include the phase transition (EPOS [38] – NA61/SHINE analysis, UrQMD [39], and SMASH [40] – NA61/SHINE analysis) describe the data for small systems (p+p and Be+Be), but fail to describe the data for heavier systems (Ar+Sc and Pb+Pb). On the other hand, PHSD [41] which includes the phase transition, describes the data for heavier systems but overestimates the results for small systems. Both statistical models that were taken into account (HRG [39] and SMES [42]), overestimate the $K^+/\pi^+$ ratio for small systems. As none of the models correctly reproduces the data, the origin of the onset of fireball phenomenon is not yet fully understood.

## 1.8 Motivation of $K^0_S$ studies

Kaons are the mesons that contain strange or anti-strange valence quarks. The strange valence quarks are not present in the initial conditions of collisions between nucleons and nuclei. Thus, kaon formation implies the creation of strange and anti-strange quark pair. The strange hadron production is believed to be an important tool to study the dynamics of high-energy collisions. The mass of the strange quark is close to the temperature of the phase transition between the hadron gas and the quark-gluon plasma, which makes strangeness production very sensitive to the phase transition. The yields of the produced $K^0_S$ mesons may also be used to calculate the

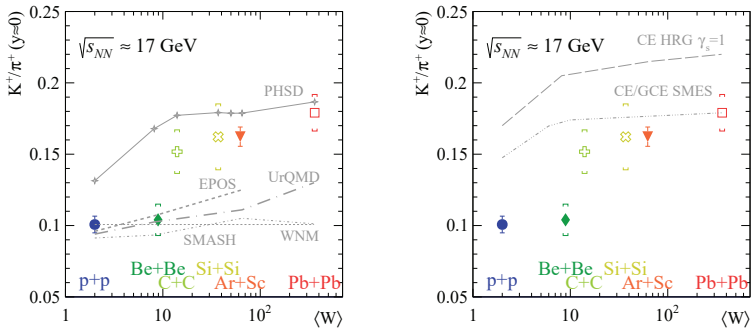


**Figure 1.8:** System size (mean number of wounded nucleons) dependence of $K^+/\pi^+$ ratio at mid-rapidity obtained at beam momenta of 150(8)$A$ GeV/$c$ compared with dynamical (*Left*) and statistical (*Right*) models. Figures from Ref. [35, 36].

$E_s$ factor [30] – strange (kaons, lambdas) to non-strange (pions) particle ratio – which is predicted to show a sharp maximum at the onset of deconfinement energy (horn). In contradiction to some model predictions [42], the horn structure was not observed in Ar+Sc collisions in the $K^+/\pi^+$ ratio [43] (see also Fig. 1.7). Studying different strange particles may bring some more information to this intriguing result. The measurement of $K^0_S$ production can also shed more light on the phenomenon of the onset of fireball. Moreover, the transverse mass distributions and mean multiplicities can be used as the inputs for the Blast-Wave (BW) models (determining kinetic/thermal freeze-out temperature and transverse flow velocity; see for example Ref. [44]) and Hadron Resonance Gas (HRG) models (determining chemical freeze-out temperature, baryochemical potential, strangeness under-saturation factor, system volume, etc.; see for example Ref. [45]).

## 1.9 $K^0_S$ measurements

The $K^0_S$ mesons have never been measured in the Ar+Sc collisions at the energies of the Super Proton Synchrotron (SPS) at CERN. The example results on $K^0_S$ meson production in heavy-ion collisions come from the following interactions:

- Al+Al by FOPI [46],
- Ar+KCl and Au+Au by HADES [47, 48],
- Au+Au by STAR [49, 50, 51, 52],
- Pb+Pb by NA49 [53] and ALICE [54],
- Pb+Au by CERES [55],
- S+S and S+Ag by NA35 [56, 57].

The example measurements are shown in Fig. 1.9. The left panel presents the yields of $K^0_S$ at mid-rapidity region as a function of collision energy in Au+Au, Pb+Au and Pb+Pb collisions. In

the right panel the example rapidity spectra of $K^0_S$ mesons in Pb+Pb collisions are plotted.

Moreover, there are many measurements of $K^0_S$ production in p+p collisions at the SPS energy range. The energy dependence of mean multiplicity of $K^0_S$ mesons produced in p+p collisions is presented in Fig. 1.10. The presented compilation includes two high-precision points measured by the NA61/SHINE experiment.

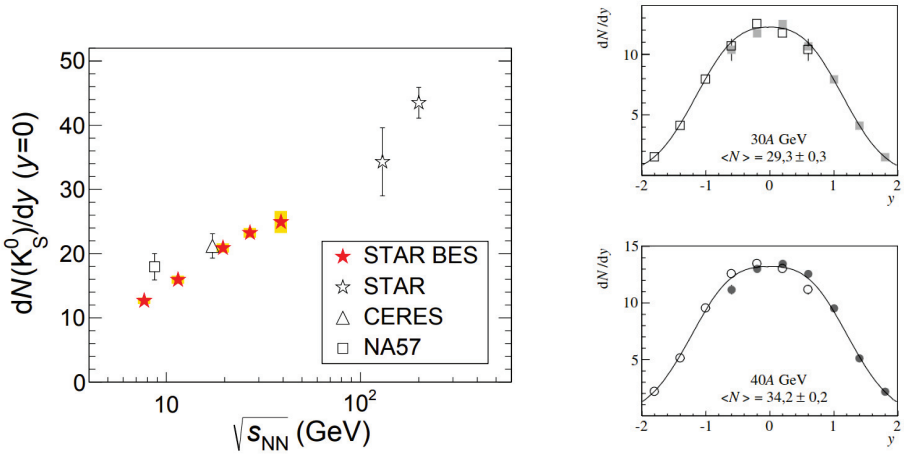


**Figure 1.9:** *Left*: Yields of $K^0_S$ mesons at mid-rapidity as function of collision energy in Au+Au, Pb+Au, and Pb+Pb collisions. Figure from Ref. [49]. *Right*: Fitted rapidity spectra of $K^0_S$ mesons produced in Pb+Pb collisions at $30A$ GeV/$c$ ($\sqrt{s_{NN}} = 7.62$ GeV) (*Top*) and $40A$ GeV/$c$ ($\sqrt{s_{NN}} = 8.77$ GeV) (*Bottom*). Open points are mirror reflection of measured closed points with respect to zero. Figures from Ref. [53].

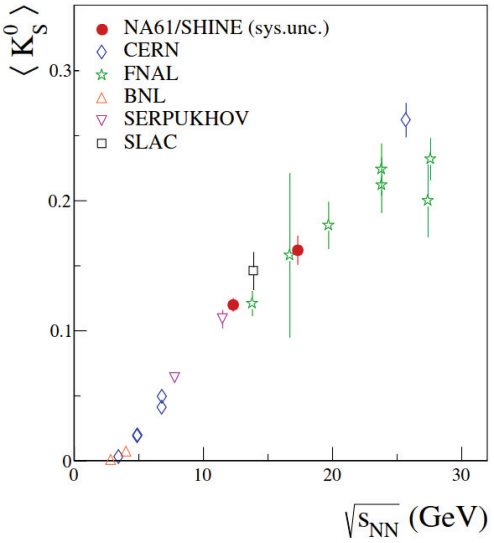


**Figure 1.10:** Mean multiplicity of $K^0_S$ mesons produced in p+p collisions as function of energy. Figure from Ref. [58].

## 1.10 Thesis outline

The main motivation of this thesis was the study of the $K^0_S$ production in the $^{40}$Ar+$^{45}$Sc collisions at beam momenta of 40$A$ GeV/$c$ and 75$A$ GeV/$c$ (the available energy in the collision center-of-mass system per nucleon pair: $\sqrt{s_{NN}} = 8.77$ GeV and $\sqrt{s_{NN}} = 11.94$ GeV, respectively).

The thesis consists of 8 chapters. Chapter 1 is the introduction. It describes the Standard Model as well as the quark-gluon plasma. At the end, the motivation of the studies is presented. Chapter 2 describes the details of the NA61/SHINE experimental setup. Chapter 3 presents the software that was used for the data reconstruction and Monte Carlo simulations. The Ar+Sc datasets used in the analysis are characterized in details in Chapter 4. Chapter 5 presents the analysis procedure used to obtain the results. The main results of this thesis are discused in Chapter 6. The results are also compared with theoretical models as well as other experimental data. Chapter 7 reports the details of the NA61/SHINE experiment upgrade and its impact on future analyses of $K^0_S$ in ion collisions. Chapter 8 is the summary of the most important results and outlook for future studies.

The units in this thesis follow the Particle Data Group (PDG) [3] convention, namely the mass is given in GeV, the momentum is given in GeV/$c$, and the energy in GeV.

**Author's contribution**

The author of this thesis has been an active member of the NA61/SHINE Collaboration since 2017. He participated in many data-taking campaigns as Detector Control System (DCS) on-call expert, Vertex Detector (VD) on-call expert, Data AcQuisition system (DAQ) on-call expert as well as run coordinator.

The code for the data analysis and plotting the results of this thesis were prepared by the author himself. He also developed the procedure of the optimization of rapidity dependent cuts and systematic uncertainty estimation. The results for Ar+Sc collisions at 75$A$ GeV/$c$ were accepted by the NA61/SHINE Collaboration and released as preliminary. They have been already presented at the WWND 2023 conference [35] and are planned to be reported at the Quark Matter conference in Semptemer 2023 by the NA61/SHINE Collaboration. The initial plan for the thesis was to analyse only the data on Ar+Sc collisions at 75$A$ GeV/$c$. However, the interesting results of large isospin symmetry breaking inspired the author to perform also the analysis of Ar+Sc collisions at 40$A$ GeV/$c$. Except of the analysis presented in this thesis, the author had a significant input to the analysis of the data collected for the feasibility studies of the new open charm programme of the experiment. The author developed the algorithm for the alignment of the silicon sensors of the Vertex Detector as well as the algorithm for track matching of the VD tracks and Time Projection Chamber (TPC) tracks.

Moreover, the author played a key role in the upgrade of the NA61/SHINE experiment. He spent 4 years of his Ph.D. studies at CERN. The author was responsible for the development of the software framework for the new DAQ system, called pteroDAQtyl. He implemented the code for collecting the data from TPC read-out electronics as well as software for building the full events and saving them to files. He also participated in many tests of the new read-out electronics and analysed the data, proving the benefits of the upgrade. The author participated in the campaigns for the installation of the new electronics and partially coordinated the electronics installation of Main TPCs.

Chapter 2

# NA61/SHINE experiment

SPS Heavy Ion and Neutrino Experiment (SHINE) [59] is a fixed target hadron spectrometer operating at the CERN Super Proton Synchrotron (SPS). It is a successor of the NA49 experiment [60]. The main physics motivations of the NA61/SHINE experiment are to study the dynamics of nuclear collisions as a part of the strong interactions programme, as well as to perform the reference measurements for the neutrino and cosmic rays experiments. This chapter summarises the physics programme of the NA61/SHINE experiment and the main components of the detector setup. The detector setup is optimised before each data-taking campaign to meet the data specific requirements. This chapter characterizes the full possible detector setup as it was available in 2018, before the upgrade during the Long Shutdown 2 (LS2) at CERN (see Chapter 7). In the detailed description of each subsystem, it is clarified if it was used during the Ar+Sc data-taking campaign and in which configuration.

## 2.1 Physics Programme

NA61/SHINE experiment has a very broad physics programme. One of the main points is the strong interactions programme which includes the study of the phase transition between the hadron gas and the quark-gluon plasma. Additionally, NA61/SHINE performs a range of reference measurements for neutrino and cosmic-rays experiments, including:

- precise hadron production measurements in p+C collisions for long-baseline neutrino experiments (T2K, NO$\nu$A) in order to better estimate the neutrino fluxes [61, 62, 63, 64],
- cross-section and hadron production measurements in $\pi$+C collisions in order to better simulate the cosmic-ray shower propagation through the atmosphere. The simulations are used to understand the properties of the primary cosmic-ray particles [65, 66, 67],
- nuclear fragmentation cross-section measurements of intermediate-mass nuclei in order to better simulate the propagation of the cosmic rays in galaxies as well as seach for the candidates of the dark matter particles [68, 69].

Within the strong interactions programme, the NA61/SHINE experiment performed a unique two-dimensional scan in the size of the colliding system and the beam momentum. The summary of collected data is presented in the left panel of Fig 2.1. The size of the squares corresponds to the collected statistics for a given system. Gray colour illustrates the plan for the future data-taking. NA61/SHINE collected data for p+p, p+Pb, Be+Be, Ar+Sc, Xe+La, and Pb+Pb collisions at up to six different beam momenta from 13$A$ GeV/$c$ to 150/158$A$ GeV/$c$ (158 is for p+p collisions,

$A$ GeV/$c$ means the momentum per nucleon of the beam ion).

The presented scan allows for the large coverage of the phase diagram of strongly interacting matter illustrated schematically in the right panel of Fig. 2.1. The values of chemical freeze-out temperatures and bariochemical potentials were estimated based on the fits within one of HRG models [45].

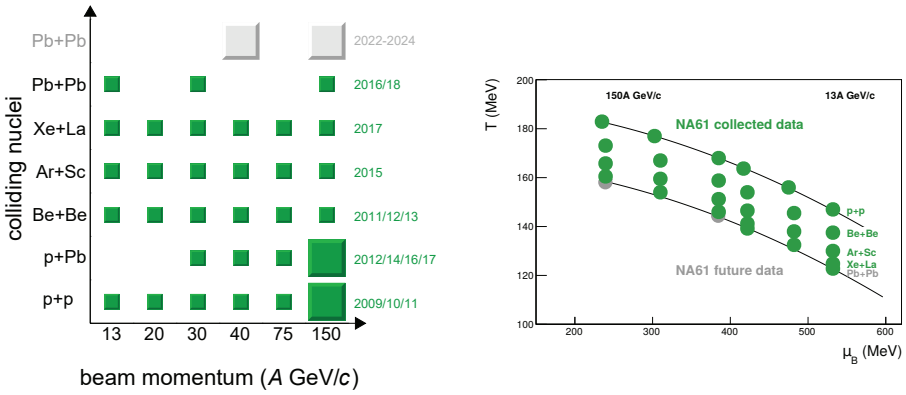


**Figure 2.1:** *Left*: Summary of data collected within system size – beam momentum scan performed by NA61/SHINE. Pb+Pb data at 150$A$ GeV/$c$ were partially collected in 2022. *Right*: Coverage of phase diagram of strongly interacting matter by NA61/SHINE data. Figures from Ref. [70].

## 2.2 NA61/SHINE detector

The NA61/SHINE detector is a multi-purpose spectrometer optimised to study the hadron production in various types of collisions (hadron-proton, hadron-nucleus and nucleus-nucleus). The schematic picture of the setup as it was in 2018, before the upgrade during the Long Shutdown 2, is presented in Fig 2.2. The main tracking devices of the NA61/SHINE spectometer are the Time Projection Chambers (TPCs). Two Vertex TPCs (VTPC-1 and VTPC-2), placed in the magnetic field, together with two large volume Main TPCs (MTPC-L and MTPC-R) are able to register a large number of particle tracks (up to 1500 in central Pb+Pb collisions). The measurement is complemented by the four smaller chambers (GAP TPC and three Forward TPCs – FTPC-1/2/3) located along the beam axis. Such a setup gives an excellent capabilities in the charged particle trajectories and momenta measurements. The information about the energy losses ($\mathrm{d}E/\mathrm{d}x$) together with Time-of-Flight (ToF) measurements allow for the particle identification in wide momenta range. The last detector on the beamline is the Projectile Spectator Detector (PSD). It is used to measure the energy of the spectators and determine the centrality in nucleus-nucleus collisions. Right after the target, the Vertex Detector (VD) is installed. It allows for the high accuracy reconstruction of the interaction primary vertex and decay vertices of short-lived particles. The incoming beam particles are measured by an array of beam detectors (see the inset in

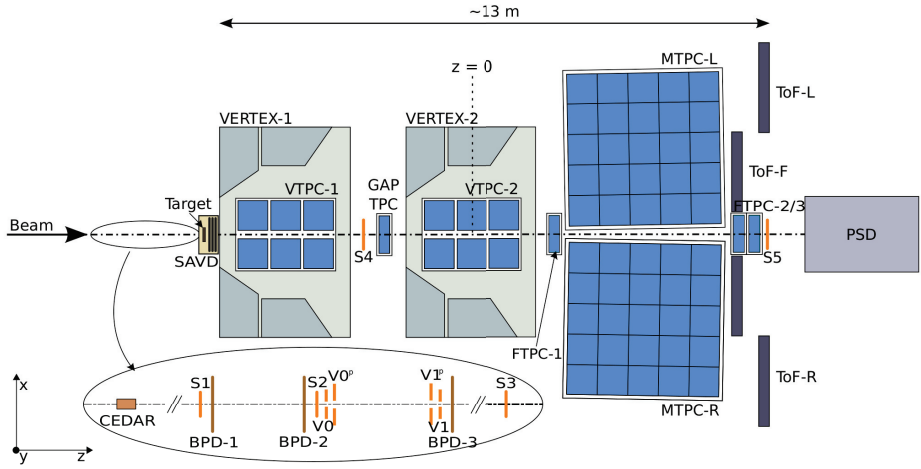


**Figure 2.2:** Schematic picture of NA61/SHINE detector. S3 detector is placed after target. Figure from Ref. [70].

Fig. 2.2), used to identify and measure the trajectory of the beam particles as well as trigger the data acquisition of the whole spectrometer.

Figure 2.2 defines also the coordinate system of the NA61/SHINE. The origin of the system is located in the center of VTPC-2 on the beamline. The coordinate system is right-handed. The $z$ axis is horizontal and goes along the beam axis. The $x$ axis is horizontal and perpendicular to the $z$ axis. The $y$ axis is vertical and points up.

## 2.3 Beamline and trigger system

### 2.3.1 Accelerator complex

NA61/SHINE performs the experiments with various types of beams – from hadrons to heavy-ions in broad momentum range – from 13$A$ GeV/$c$ to 150$A$ GeV/$c$ for ions and 13 GeV/$c$ to 400 GeV/$c$ for hadrons. The experiment can utilize the primary beams as well as secondary beams created in the primary beams fragmentation. Before reaching the experiment, the beams are accelerated in few stages in the CERN accelerator complex which is presented in Fig. 2.3. The elements relevant to the NA61/SHINE experiment are highlighted. The initial steps of the acceleration of hadrons and ions are different.

**Proton beams**

The acceleration chain for proton beam is presented in blue colour in the left panel of Fig. 2.3. The beam is generated from hydrogen gas by a duo-plasmatron ion source. Then, before reaching LINAC2, it is focused, bunched and accelerated to 750 keV/$c$ by the Radio-Frequency Quadrupole RFQ2. LINAC2 (replaced by LINAC4 during the Long Shutdown 2) accelerates the beam to

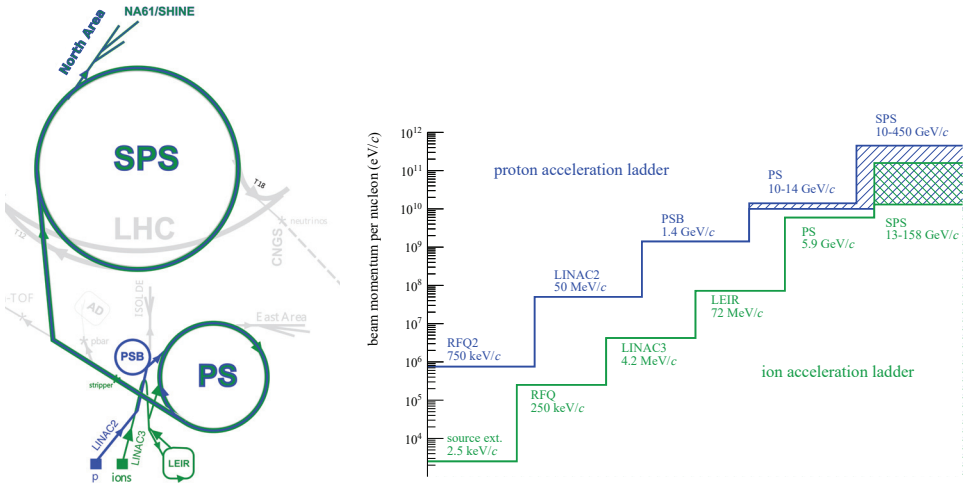


**Figure 2.3:** *Left:* Schematic picture of CERN accelerator chain relevant to NA61/SHINE (top view, not to scale). *Right:* Quantitative visualization of consecutive steps of beam acceleration for protons (blue) and ions (green). Figures from Ref. [70].

50 MeV/$c$ and then distributes the beam in the four rings of the Proton Synchrotron Booster (PSB). Accelerated to 1.4 GeV/$c$ beam is extracted to the Proton Synchrotron (PS). After this stage, the beam reaches the momentum of 14 GeV/$c$. The next step is the Super Proton Synchrotron (SPS) which accelerates the protons up to 450 GeV/$c$. Then, the beam is extracted to the North Area in so-called *slow extraction* process. The slow extraction debunches the beam and allows for the constant flux of the particles within several seconds. It results in an approximately constant beam intensity delivered to the experiments during the single extraction, referred to as a *spill*. The following steps of proton beam acceleration chain with corresponding beam momenta are shown in blue colour in the right panel of Fig. 2.3.

**Ion beams**

The acceleration chain for ion beams is presented in green colour in the left panel of Fig. 2.3. The primary lead beam is created by evaporating isotopically pure $^{208}$Pb sample and the beams originating from nuclei of gases like argon or xenon are created in the gas sources. The atoms are ionized in an electron cyclotron resonance (ECR) source and then electrostatically extracted with the energy of 2.5$A$ keV/$c$ into the separator. It selects particular charge state for a given beam type. Then, the beam is accelerated to 250$A$ keV/$c$ by RFQ and injected into LINAC3 linear accelerator. After this stage, the beam reaches the momentum of 4.2$A$ MeV/$c$. Then, it is extracted to the Low Energy Ion Ring (LEIR), in which it reaches the momentum of 72$A$ MeV/$c$. The next step is the PS, which accelerates the beam to 5.9$A$ GeV/$c$. After the PS, the beam undergoes a final stripping

to produce a fully ionized ion beam. Then, it is injected into the SPS for final acceleration up to 158$A$ GeV/$c$ and slowly extracted to the North Area. The following steps of primary ion beam acceleration chain with corresponding beam momenta are shown in green colour in the right panel of Fig. 2.3.

### 2.3.2 H2 beamline

The accelerated primary beam extracted from the SPS is transported to the primary target station, where the secondary beam can be produced. Then, the primary or secondary beam is transferred to the area of the NA61/SHINE experiment via H2 beamline, which is schematically presented in Fig. 2.4. If the primary beam is used, the T2 target is removed from the beam trajectory. The H2 beamline allows for the selection of the desired momentum and type of the beam. There are two spectrometers which are used to select the rigidity of the beam (momentum to charge ratio), built out of dipole magnets and collimators. The H2 beamline is equipped with dipole magnets (to bend the beam), quadrupole magnets (to focus the beam) and collimators (to reduce the transverse size and decrease the beam intensity). A set of detectors is installed along the H2 beamline, providing the information about the beam characteristics, for example: position, intensity and particle identification. For the data-taking with ion beams, NA61/SHINE used Be secondary beam and Ar, Xe, Pb primary beams.

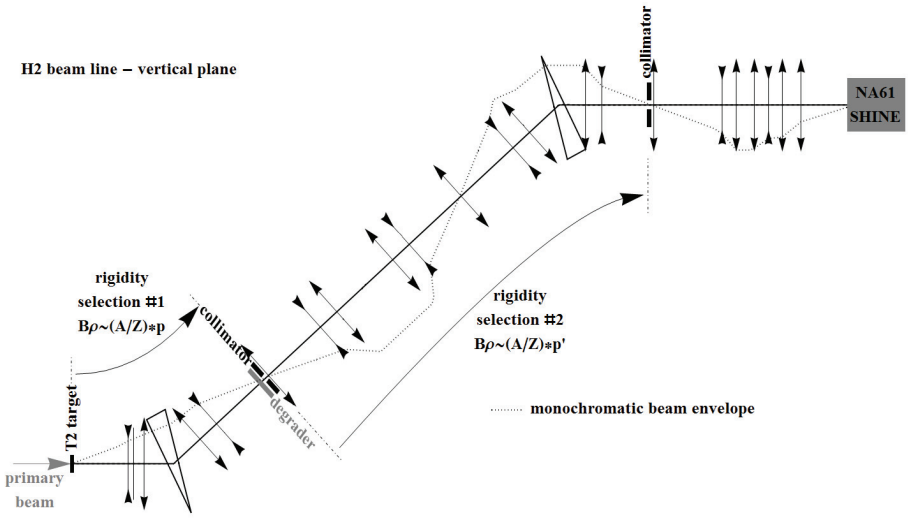


**Figure 2.4:** Schematic view of vertical plane of H2 beamline. Dimensions are not to scale (e.g. beamline is approximately 600 m long and height difference between target station and NA61/SHINE is about 12 m). Figure from Ref. [59].

| detector | dimensions (mm) | hole (mm) | position (m) |
|---|---|---|---|
| S1 | $60 \times 60 \times 5$ | | -36.42 |
| S2 | $\phi = 28 \times 2$ | | -14.42 |
| S3 | $\phi = 26 \times 5$ | | -6.58 |
| S4 | $\phi = 20 \times 5$ | | -2.11 |
| S5 | $\phi = 20 \times 5$ | | 9.80 |
| V0 | $\phi = 80 \times 10$ | $\phi = 10$ | -14.61 |
| V0$^{\mathrm{p}}$ | $300 \times 300 \times 10$ | $\phi = 20$ | $\approx$ -14 |
| V1 | $100 \times 100 \times 10$ | $\phi = 8$ | -6.72 |
| V1$^{\mathrm{p}}$ | $300 \times 300 \times 10$ | $\phi = 20$ | -6.74 |
| BPD-1 | $48 \times 48 \times 32.6$ | | -36.20 |
| BPD-2 | $48 \times 48 \times 32.6$ | | -14.90 |
| BPD-3 | $48 \times 48 \times 32.6$ | | -6.70 |
| Typical thin target position | | | -5.81 |

**Table 2.1:** Summary of typical beam detector parameters: dimensions, positions along beamline ($z$ coordinate) [59]. Positions of most of these detectors varied in time by few cm due to dismounting and remounting in subsequent runs. Positions of detectors are surveyed before each run. For circular detector, diameter ($\phi$) $\times$ thickness is provided.

### 2.3.3 Beam Detectors

The NA61/SHINE beamline is equipped with many beam detectors providing the information about the beam position, charge and timing. The beam detectors are shown in Fig. 2.2 in the enlarged panel in the left bottom corner. There is a set of scintillators (S1, S2, V0, V0$^{\mathrm{p}}$, V1, V1$^{\mathrm{p}}$) placed along the beamline upstream of the target as well as a beam telescope of three precise Beam Position Detectors (BPDs). Three other scintillators (S3, S4, S5) are installed downstream of the target. They are used for triggering on inelastic interactions of the beam particles inside the target.

The scintillator counters are read-out by fast photo-multiplier tubes (PMTs). They transform the scintillation light into electrical signal, which is then passed to the read-out electronics and trigger logic. Before each data-taking campaign, a set of counters that are used is properly selected based on the beam type and trigger requirements. It is crucial to minimize the amount of the material on the beam trajectory in order to minimize the number of interactions of the beam particles with the detector material. The typical parameters of the beam detectors are presented in Table 2.1.

The S1 and S2 are the scintillating counters. The S1 is equipped with four PMTs on each side perpendicularly to the beam trajectory. The signals from all four PMTs allow for very precise timing measurement, independently of the beam position in the scintillator plane. The amplitude of the S1 and S2 signals are proportional to the squared charge $Z^2$ of the incoming particle. Thus, they can be used to select beam particles with different charge states $Z$ in the off-line analysis. The S1 and S2 signals are always used in the coincidence in the trigger logic.

The next group of scintillators consists out of the veto counters V0, V0$^{\mathrm{p}}$, V1, V1$^{\mathrm{p}}$. They have a hole of a small diameter in the center. Those counters are used in anti-coincidence (veto) mode in the trigger logic. It allows for triggering only on the core of the beam, removing the beam halo.

The interaction counters S3, S4 and S5 are placed downstream of the target. When the interaction of a beam particle occurs, there is no signal of the beam particle registered in the interaction counters. Thus, the S3, S4 or S5 signals are used in the anti-coincidence mode in the trigger logic. Typically, a single counter is included in the trigger logic during the data-taking. It is selected based on the beam type and detector configuration.

During the data-taking campaigns with the secondary hadron beams, the beamline is additionally equipped with a Cherenkov Differential Counters with Achromatic Ring Focus (CEDAR) [71]. The detector is filled with gas as a radiator and equipped with a dedicated optic system. By adjusting the pressure of the gas and tuning the optics, the CEDAR is able to accept only a desired hadron species. It allows for the beam particle identification on the trigger level. The CEDAR signal is used in the coincidence mode in the trigger logic.

The trajectory of each incoming beam particle is measured by the telescope of three BPDs (BPD-1, BPD-2, and BPD-3). The BPDs are the proportional chambers operating with the Ar/$CO_2$ gas mixture in the proportions of 85/15. The schematic picture of a single detector is presented in Fig. 2.5. It consists out of two planes of orthogonal readout strips, which allow to measure the position of the beam particles in $x$–$y$ plane.

In the Ar+Sc data-taking campaign the telescope of three BPD detectors was used. The configuration of other beam detectors used in the Ar+Sc data-taking is discussed in Section 4.1.

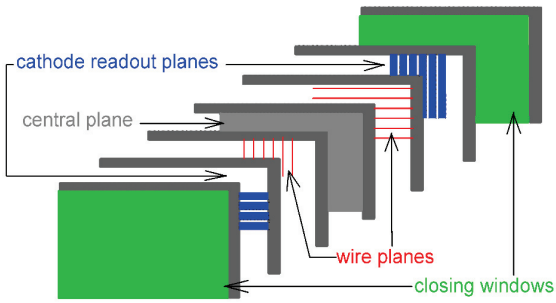


**Figure 2.5:** Schematic layout of BPD detector. Figure from Ref. [72].

| Name | Definition | Description |
|---|---|---|
| T1 | $S1 \cdot S2 \cdot \overline{V0} \cdot \overline{V1} \cdot CEDAR$ | identified beam |
| T2 | $S1 \cdot S2 \cdot \overline{V0} \cdot \overline{V1} \cdot CEDAR \cdot \overline{S4}$ | identified interaction |
| T3 | $S1 \cdot S2 \cdot \overline{V0} \cdot \overline{V1}$ | unidentified beam |
| T4 | $S1 \cdot S2 \cdot \overline{V0} \cdot \overline{V1} \cdot \overline{S4}$ | unidentified interaction |

**Table 2.2:** Example list of trigger definitions used during data-taking with secondary hadron beams.

### 2.3.4 Trigger system

The trigger system allows for selection of the events that are interesting from the point of view of the physics goal of the experiment. The selection is done online what greatly reduces the amount of data that are recorded.

The NA61/SHINE trigger system is based on the analog signals from the beam detectors described in the previous section. The trigger decision is made through the coincidence of input signals. Any analog signal that arrives in the proper time window can be included in the trigger. Very often the signal from PSD is included, providing an online centrality selection. The analog signals are discriminated by the Constant Fraction Discriminators (CFDs). They convert the analog signal into digital one, if the amplitude of the input signal is sufficiently high. Then, the signals are passed to the core of the trigger logic – unit based on Field Programmable Gate Array (FPGA). It generates the Main Trigger (MT) signal which starts the data acquisition on the read-out electronics. Additionally, each sub-detector provides a busy signal when reading out the data. If any of the sub-systems is busy, the MT signal is not generated.

Up to four independent trigger configurations can be run in parallel (T1, T2, T3, and T4). They differ by the signals which are taken into account in the coincidence. The example definition of the trigger configuration for the data taking with secondary hadron beam is presented in Table 2.2. The generated T1–T4 signals are send to prescaller module. It reduces the fraction of given trigger type, that contribute to the MT generation. Thus, not each trigger of a given type is recorded. The prescaller passes only one of $N$ input pulses, where $N \in [1, 4096]$ is a configurable parameter. As a result, the fraction of $1/N$ triggers of a given type are stored. The prescalling solution is used to obtain the desired fraction of events triggered by each of the trigger configurations in the collected data.

The trigger configuration used during the Ar+Sc data-taking campaign is described in details in Sec. 4.1.

## 2.4 Time Projection Chambers

### 2.4.1 Principle of work

The schematic picture of the Time Projection Chamber is presented in Fig. 2.6. It is built out of a gas volume marked in grey surrounded by a field cage and a read-out plane on the top. The

field cage consists of shaping electrodes coupled with a resistive voltage divider terminated with a cathode plate on the bottom. It provides a uniform electric field along the vertical axix ($y$-axis in the NA61/SHINE coordinate system) within the active volume of the TPC. When the charged particle crosses the active volume of the TPC, it ionises the gas mixture along its trajectory. The free electrons created in the ionization process form the primary ionization clusters, marked as blue circles in Fig. 2.6. The primary ionization electrons drift in the electric field towards the read-out part with a velocity $v_D$. As the number of primary ionization electrons is too small to be detected by the read-out electronics, the amplification mechanism is needed.

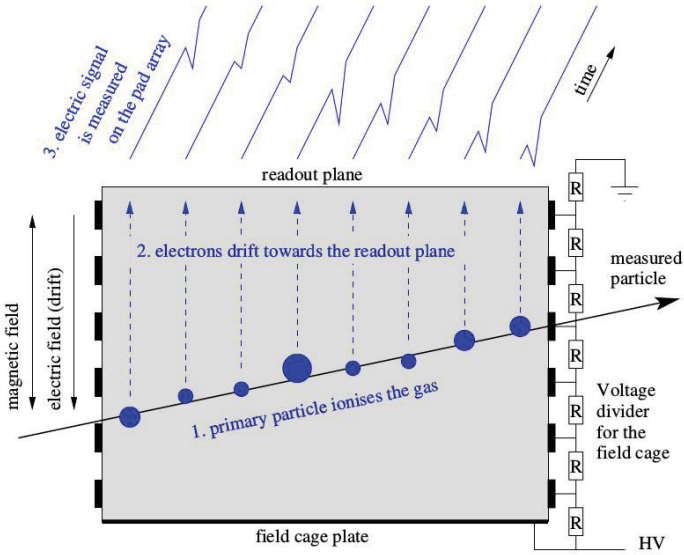


**Figure 2.6:** Schematic picture presenting principle of operation of Time Projection Chamber. Figure from Ref. [73].

For the amplification, NA61/SHINE uses the solution based on the Multiwire Proportional Chambers (MWPCs) [74, 75]. Another solution is based on Gas Electron Multiplier (GEM) foils and is used for example in the ALICE experiment [76]. The schematic picture of MWPC based solution is presented in Fig. 2.7. The idea is that the primary ionization electrons are accelerated by the field created by high voltage applied between the two layers of wires. Accelerated electrons start further ionize the gas, creating the electron avalanche and positive ions drifting in the opposite direction. The local current mainly created by moving ions induces the charge on the pads which can be read-out by the charge sensitive amplifiers of the Front-End Electronics (FEE). Knowing the position of the pads, one can reconstruct the two-dimensional trajectory of the particle. The third coordinate can be calculated from the time and drift velocity $v_D$ of the electrons in the specific gas mixture.

In Fig. 2.7 the first layer of the wires from the bottom is called Gating Grid. It separates the

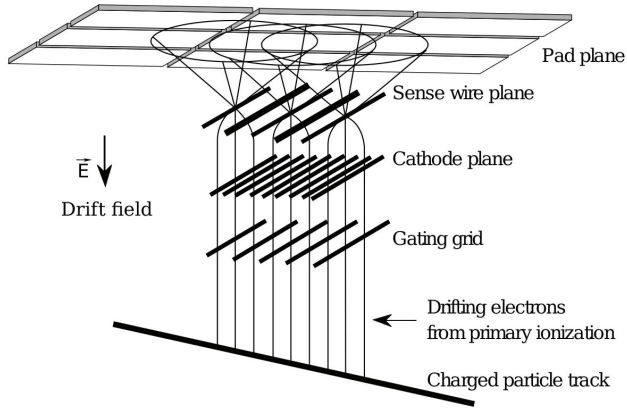


**Figure 2.7:** Schematic picture of TPC read-out. Figure from Ref. [60].

drift volume of the TPC with the MWPC read-out part. In the open state, all wires are held at the same potential, which makes them transparent to the drifting electrons and ions. In the closed state, for each pair of the wires additional positive potential for one wire and negative potential for second wire is applied. It prevents electrons and ions from passing between amplification and drift volumes. When the valid trigger signal is received, the Gating Grid opens and FEE starts sampling the signals from all the pads into 256 time-slices with 5 MHz sampling frequency in case of the NA61/SHINE experiment. This gives the charge collection window lasting for $t_s = 51.2$ µs. This time derives from the length of the drift volume and the drift velocity of the electrons. After the charge collection is done, the Gating Grid closes and opens again for the next valid read-out trigger signal. This mechanism prevents the space charge accumulation inside the chamber as well as reduces the aging effect of the amplification part of MWPC.

After the Gating Grid, there are two cathode planes surrounding the sense wires. The cathode plane closer to the Gating Grid is made out of wires, while the second one is a solid plane subdivided into the read-out pads. The sense wires plane consists of anode wires interspersed by the field wires (kept at zero potential). The presence of the field wires helps to shape the electric field and allows to use lower anode voltages improving the stability of the chamber. The high voltage on the anode wires is adjusted in a way that the MWPC operates in the proportional mode – the signal is proportional to the primary ionization charge and thus to the energy deposit of ionizing particle traveling through the chamber. The information about the energy deposit can be used to identify the particles.

For a single ionizing particle going through the TPC, the energy deposit of the reconstructed clusters follows the Landau distribution, presented in the left panel of Fig. 2.8. It has a long tail towards high values of energy deposit, thus high fluctuations of the measured values are expected. To minimize the impact of high-value fluctuations, the truncation method is used (presented in

the right panel of Fig. 2.8). It is about removing a fraction of the clusters with the highest energy deposit values from the calculations. This method significantly improves the resolution of the reconstructed energy loss, improving the particle identification procedure.

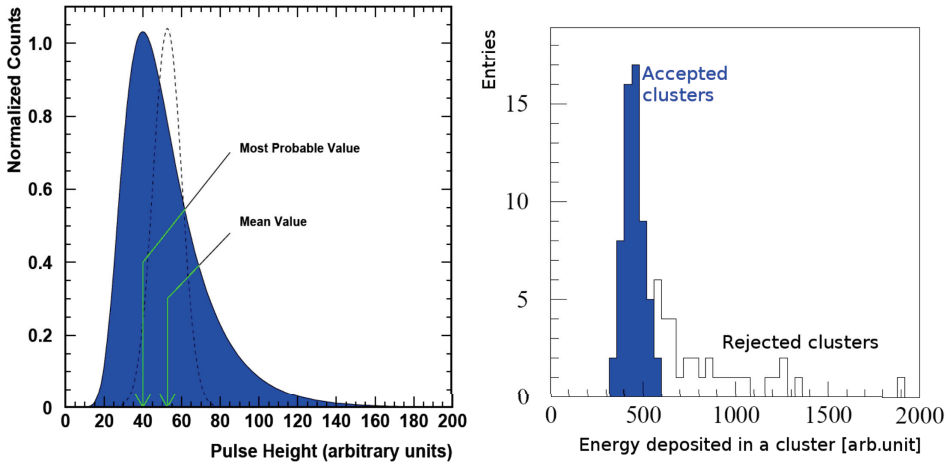


**Figure 2.8:** *Left*: Landau shape describing charge distribution in primary ionization clusters (marked with shaded blue area). Gaussian peak of comparable width is shown with dashed line for reference. *Right*: Sample distribution of measured cluster energy deposits, showing principle of truncation procedure. Small deposit clusters (blue area) are accepted for energy-loss measurement. Figures from Ref. [73].

For moderately relativistic particles ($0.1 \leq \beta\gamma \leq 500$), the mean rate of energy loss is described by the Bethe-Bloch formula [3]:

$$\left\langle -\frac{\mathrm{d}E}{\mathrm{d}x} \right\rangle = Kz^2 \frac{Z}{A} \frac{1}{\beta^2} \left[ \frac{1}{2} \ln \frac{2m_e c^2 \beta^2 \gamma^2 W_{\max}}{I^2} - \beta^2 - \frac{\delta(\beta\gamma)}{2} \right], \tag{2.1}$$

where $K = 0.307$ MeV mol$^{-1}$ cm$^2$ (constant), $z$ – the charge of the incident particle in the electron charge units, $Z$ – atomic number of the absorber, $A$ – mass number of the absorber, $\beta = v/c$, $v$ – velocity of the particle, $\gamma = (1-\beta^2)^{-1/2}$, $m_e$ – electron mass, $I$ – mean excitation energy of the absorber, $W_{\max}$ – maximum energy that can be transferred to an electron in a single ionization act, and $\delta(\beta\gamma)$ – density effect correction to ionization energy-loss. The particles with different masses ($m_0$) but the same momenta ($p$) will have different $\beta$:

$$\beta = \frac{p}{\gamma m_0 c} \tag{2.2}$$

and thus different energy losses. Therefore, by measuring the energy loss and momentum of the particle, one can identify the particle type. The example measurement of the energy loss as a function of particle momenta is presented in Fig. 2.9. The black lines show the Bethe-Bloch parametrization of the energy loss for different particle types.

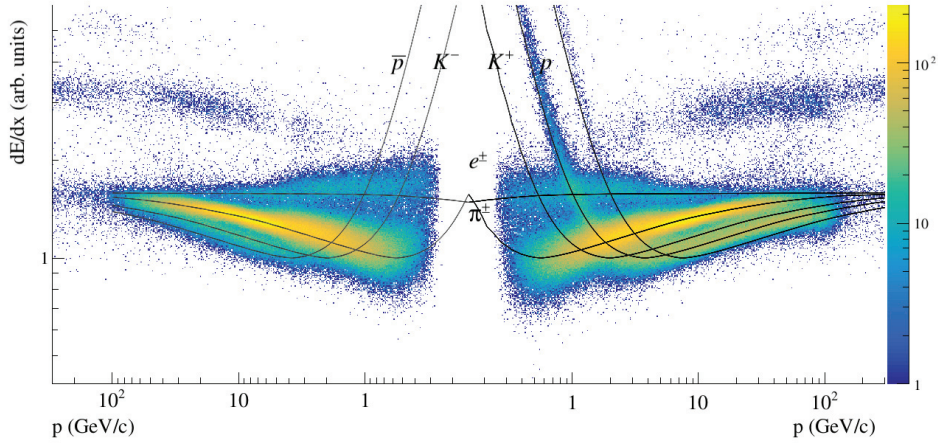


**Figure 2.9:** Distribution of energy loss versus momentum measured by NA61/SHINE TPCs in Ar+Sc collisions at 75$A$ GeV/$c$. Solid lines show nominal Bethe-Bloch functions (Eq. (2.1)) for different particle species. Clouds visible for $p > 10$ GeV/$c$ above main part of distribution correspond to heavier fragments produced in Ar+Sc interactions. Right part of plot shows positively charged particles while left part negatively charged ones.

In the high-energy physics experiments, the most common TPC active medium is the proper gas mixture, usually based on noble gas (e.g. Ar or Ne) with the addition of so-called quenching gas (e.g. $CH_4$ or $CO_2$). The role of the quenching gas is to stabilize the operation of the gas mixture and to suppress uncontrolled growth of electron avalanches. The stability of the gas mixture is crucial for the data-taking, as any small variation can change the detection properties of the TPCs.

### 2.4.2 NA61/SHINE TPCs

The Time Projection Chambers are the main detectors in NA61/SHINE used to register the trajectories of the particles and identify them. The VTPC-1 and VTPC-2 are placed in the magnetic field. It allows for the measurement of the momenta of charged particles by measuring the curvatures of their trajectories in the magnetic field. The most important parameters of NA61/SHINE TPCs are collected in Table 2.3. The VTPCs and MTPCs are divided into sectors read-out by separate MWPCs. All the TPCs operate with Ar/$CO_2$ mixture with the proportions listed in Table 2.3. The orientation of read-out pads in the VTPC and MTPC sectors close to the beam is optimized for the high-track density environment. The pads are tilted in a way to minimise the angle between a particle track and the longer edge of a pad.

During the Ar+Sc data-taking campaign VTPCs and MTPCs were used.

| | VTPC-1/2 | MTPC-L/R | GAP-TPC | FTPC-1/2/3 |
|---|---|---|---|---|
| Size (L×W×H) (cm) | 250 × 200 × 98 | 390 × 390 × 180 | 30 × 81.5 × 70 | 60 × 71/81 × 160 |
| Drift length (cm) | 66.60 | 111.74 | 58.97 | 101.40 |
| Drift voltage (kV) | 13 | 19 | 10.2 | 17.3 |
| Gas mixture Ar/$CO_2$ | 90/10 | 95/5 | 90/10 | 94/6 |
| Number of sectors | 2 × 3 | 5 × 5 | 1 | 1 |
| Number of padrows | 72 | 90 | 7 | 12 |
| No. of pads/TPC | 26 886/27 648 | 63 360 | 672 | 1536 |

**Table 2.3:** Parameters of NA61/SHINE Time Projection Chambers [59, 77]. Dimensions are given along $x$ (width), $y$ (height) and $z$ (length) axes in NA61/SHINE coordinate system. Number of pads in VTPC-2 is slightly higher than in VTPC-1. Also, FTPC-1 is 10 cm narrower than FTPC-2/3.

## 2.5 Time-of-Flight detectors

The tracking system of the NA61/SHINE detector is supplemented by the measurement of the time of flight of the particles. This can give an additional independent information about the particle identification. The Time-of-Flight (ToF) detector consists of left and right walls (ToF-L and ToF-R) placed behind the MTPCs symmetrically with respect to the beamline as well as the forward ToF detector (ToF-F) which fills the gap between ToF-L and ToF-R.

The ToF detector measures the time that the particle needs to reach the detector after the production. The momentum and the distance traveled by particle can be reconstructed from the measured trajectory. Knowing the length of the trajectory and the time, one can calculate the velocity. Then, from the measured momentum and the velocity, it is possible to reconstruct the mass of the particle, and thus to identify the type of the particle. The whole ToF detector was used in the Ar+Sc data-taking campaign, however the ToF information is not used in the analysis presented in this thesis.

### 2.5.1 ToF-L and ToF-R

The ToF-L and ToF-R are the two ToF walls placed behind the MTPCs. They are built of a matrix of plastic cuboidal-shaped scintillators. The schematic picture of ToF-R is shown in Fig. 2.10. The ToF-L is a mirror reflection of ToF-R with respect to the beamline. Each wall consists of 891 scintillators with a total area of 4.4 $m^2$ for both walls. The scintillators are grouped into three sections depending on their size (marked with different colours in Fig. 2.10). They have a thickness of 23 mm, a height of 34 mm and widths of 60, 70 or 80 mm. The section of shortest scintillators is placed closest to the beam. It gives the highest granularity in the region of highest local track density. The photo-multipliers (PMTs) are glued to the smallest side of each scintillator. The time measurement resolution is equal to 100 ps for ToF-L and 80 ps for ToF-R. The difference results from the fact that the two walls were constructed separately, using different components (PMTs, read-out electronics). The resolution is enough to distinguish between pions and kaons up to a momentum of around 2 GeV/$c$. For higher momenta, the ToF measurement can be combined with the TPC $\mathrm{d}E/\mathrm{d}x$ measurement, providing excellent particle identification capabilities.

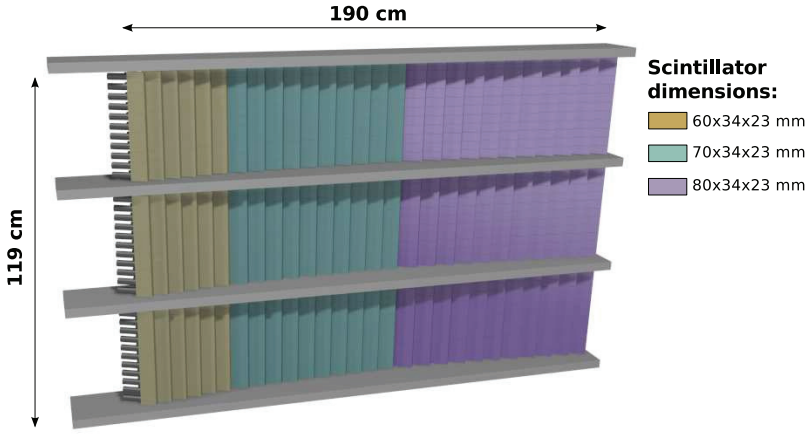


**Figure 2.10:** Schematic layout of scintillators in ToF-R detector. ToF-L detector layout is mirror reflection of ToF-R with respect to beamline. Figure from Ref. [59].

### 2.5.2 ToF-F

The NA61/SHINE measurements for the neutrino experiments required particle identification in the forward phase-space region which was not covered by ToF-L/R. In order to meet these requirements, the additional forward ToF (ToF-F) was constructed. It is built out of 120 cm long, 10 cm wide and 2.5 cm thick scintillator bars oriented vertically. The scintillators overlap by 1 cm to ensure the full coverage. Each scintillator is equipped with two photo-multipliers installed on both ends of the bars (top and bottom). The vertical coordinate of the hit can be reconstructed from the time difference in signal registration between two PMTs.

## 2.6 Projectile Spectator Detector

The last detector on the NA61/SHINE beamline is a zero-degree hadron calorimeter called Projectile Spactator Detector (PSD). It measures the energy flow around the beam direction, which in nucleus-nucleus reactions is primarily a measure of the number of projectile spectators (non-interacting nucleons). The higher energy is registered, the less nucleons took part in the interaction during the collision, which means less central collision. Thus, the measured energy can be used in the trigger system to register the most central collisions. Later, in the off-line event-by-event analysis, the number of interacting nucleons from the projectile can be estimated with the precision of one nucleon.

The schematic front layout of PSD is shown in the left panel of Fig. 2.11. The detector consists of 44 modules. The central part is built of 16 modules with a transverse size of 10 x 10 $cm^2$ and the outer part consists of 28 modules with a transverse size of 20 x 20 $cm^2$. The layout of a single module is shown in the right panel of Fig. 2.11. A PSD module is built of 60 pairs of 16 mm thin

lead plates and 4 mm thin scintillator plates. The longitudinal length of each module is equal to 120 cm.

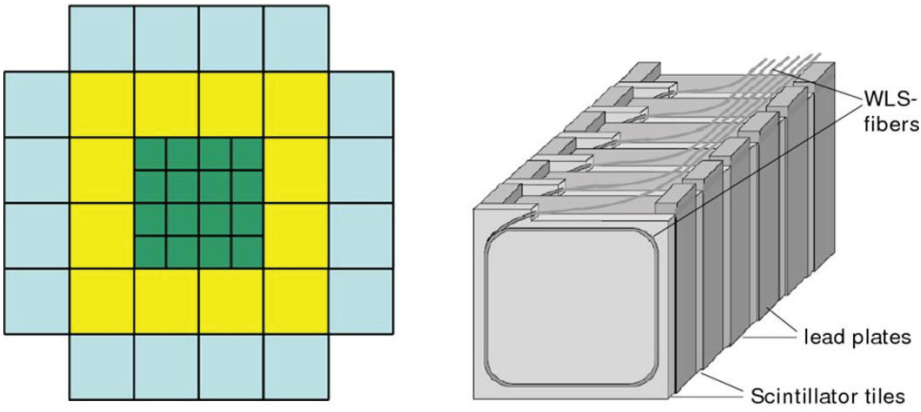


**Figure 2.11:** *Left*: Schematic transverse layout of PSD modules. *Right*: Schematic view of single PSD module. Figures from Ref. [59].

The particle which hits a given PSD module, produces a particle cascade. It includes electromagnetic and hadronic components produced in different processes like inelastic interactions, ionisations, excitations. When the cascade propagates through a module, it deposits the energy in the detector material. The energy deposit is then probed in the active material – scintillator plates. The scintillation light is transmitted by wave-length-shifter (WLS) fibres to the micro-pixel avalanche photodiodes (MAPDs). Then, the signals are read-out by the custom FPGA based front-end electronics.

In the Ar+Sc data-taking campaign the PSD detector was included in the trigger (see Section 4.1). Moreover, the information from the PSD was used in the analysis presented in this thesis to select the 10% most central Ar+Sc collisions (off-line selection – see Section 5.2.2).

## 2.7 Vertex Detector

The new physics programme of NA61/SHINE includes the measurement of the open charm mesons (built of $c/\overline{c}$ and $u/\overline{u}$ or $d/\overline{d}$ valence quarks). In order to meet the challenges of the required spatial resolution of primary and secondary vertex reconstruction, the NA61/SHINE detector setup was upgraded by a Vertex Detector. Vertex Detector is a silicon pixel detector built of 4 layers of silicon sensors separated by 5 cm. The first station is installed 5 cm behind the target. The first version of Vertex Detector – so-called Small Acceptance Vertex Detector (SAVD) – was installed in 2016. It allowed for the first direct measurement of $D^0$ and $\overline{D^0}$ mesons in heavy-ions collisions at the SPS energies [78, 79, 80] which confirmed the measurement concept. It integrated 16 MIMOSA-26AHR [81, 82] sensors, located in two movable arms. The schematic

picture of SAVD is shown in Fig. 2.12. The full-acceptance version of Vertex Detector was commissioned in 2022. It is built out of ALPIDE [83] sensors located in 4 layers. In comparison to the previous version, it has a faster read-out, much smaller noise level and bigger acceptance.

The Vertex Detector was not yet used in the Ar+Sc data-taking campaign.

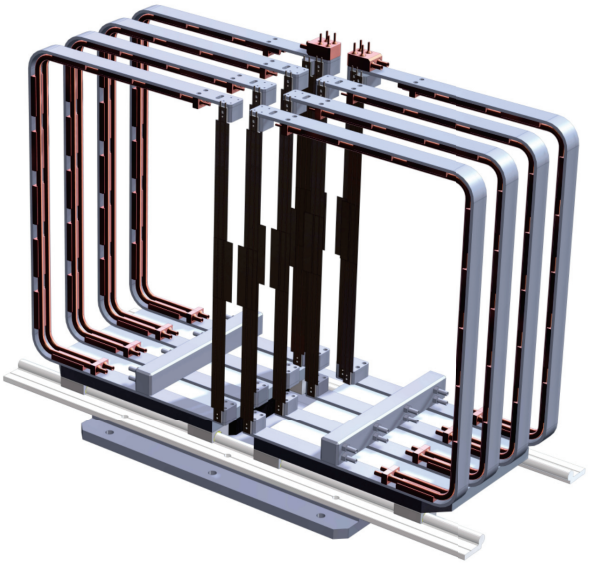

**Figure 2.12:** Schematic layout of SAVD. ”C” shaped frames located on two movable arms serve as mechanical mounting structures for sensors, limiting amount of material in region directly behind target. Figure from Ref. [84].

Chapter 3

# Data processing and Monte Carlo simulations

Data collected by the NA61/SHINE experiment have to be calibrated and reconstructed before the analysis can be performed. The data are organized in the structure of events. One event corresponds to a single collision. The digitized data from the detectors are called *raw events*. The reconstruction translates the raw detector data into particle trajectories and their properties. During the analysis, the results are corrected for the detector effects, like acceptance or detector and reconstruction efficiencies. The corrections are based on simulated *Monte Carlo* (MC) data. This chapter provides a description of the reconstruction algorithms as well as the procedure of MC simulations.

## 3.1 Reconstruction chain

The reconstruction chain is sub-divided into few stages corresponding to the different sub-detectors. At first, the information from the BPDs is reconstructed. Based on the registered hits in $x$–$y$ plane and position of the detectors, three points of the beam particle trajectories can be obtained. Then, the points are fitted with a straight line to reconstruct the trajectory of the beam particle.

The second step is the TPC reconstruction which is described in details in the section below. The reconstructed TPC tracks can be used to reconstruct the primary vertex of the interaction. For this purpose, the BPD beam track is extrapolated to the target region and the $x$ and $y$ position of the primary vertex is extracted. Then, the $z$ coordinate of the primary vertex is obtained from the extrapolated TPC tracks. All the TPC tracks originating from the primary vertex are refitted including the primary vertex point. It improves the momentum resolution of the TPC tracks.

The next step is the reconstruction of the secondary vertices which come from the decays of uncharged particles. For this purpose the algorithm called V0 finder is used. It is described in details in Sec. 3.1.2. All the reconstructed secondary vertices are stored in the events.

In order to improve the particle identification, the TPC tracks are extrapolated to the ToF walls and for the tracks within ToF acceprance, the corresponding ToF hits are assigned.

In the last step of the reconstruction procedure, the signals registered in the PSD modules

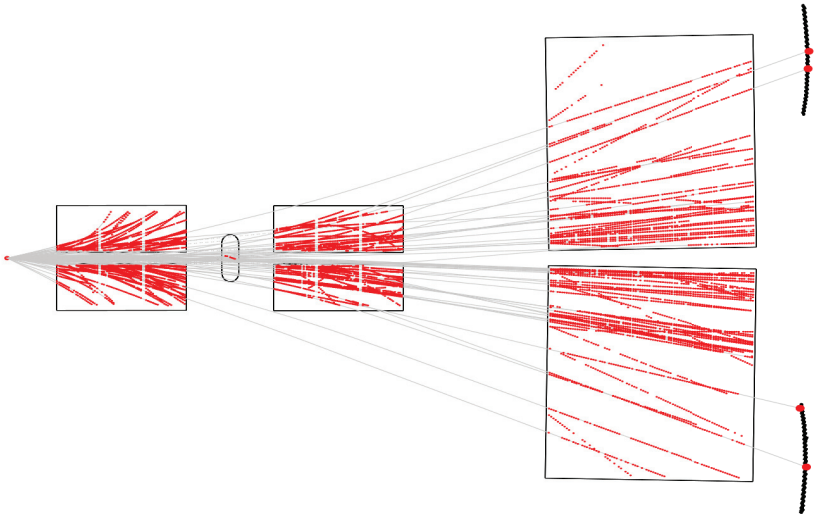

**Figure 3.1:** Example of reconstructed $^{40}$Ar+$^{45}$Sc collision at 75$A$ GeV/$c$. TPC clusters are marked as red points and reconstructed tracks are marked as gray lines.

are translated into the energy deposit in the whole calorimeter. This information is then used to determine the centrality of the collision.

As a results of the complex reconstruction procedure, one ends up with the events containing all the information necessary for the analysis. When selecting the events, it is possible for example to check if a given event has a primary vertex and check its quality or select the centrality of the event. All the reconstructed tracks contain the information about the length of the trajectory, momentum, electric charge sign, mean energy loss and the number of clusters. The example visualisation of the reconstructed event is presented in Fig. 3.1.

### 3.1.1 TPC reconstruction

The raw data from the TPCs contain the digitized signal as a function of time – so-called waveforms – from all the read-out pads. The signal in the TPCs from a single ionizing cluster can be induced in the few neighbouring pads (see Sec. 2.4.1). Thus, the first step of the reconstruction is clusterization which is about connecting the signals from neighbouring pads and timestamps, creating the cluster. Cluster is a single reconstructed three-dimensional point of the particle trajectory (red points in Fig. 3.1). The shape of the cluster signal is fitted to obtain the cluster properties, like position and total charge. Then, clusters created by one particle are connected together using the local track finding algorithm. It reconstructs the tracks from a single TPC chamber. Finally, the local tracks are connected together creating the TPC global tracks.

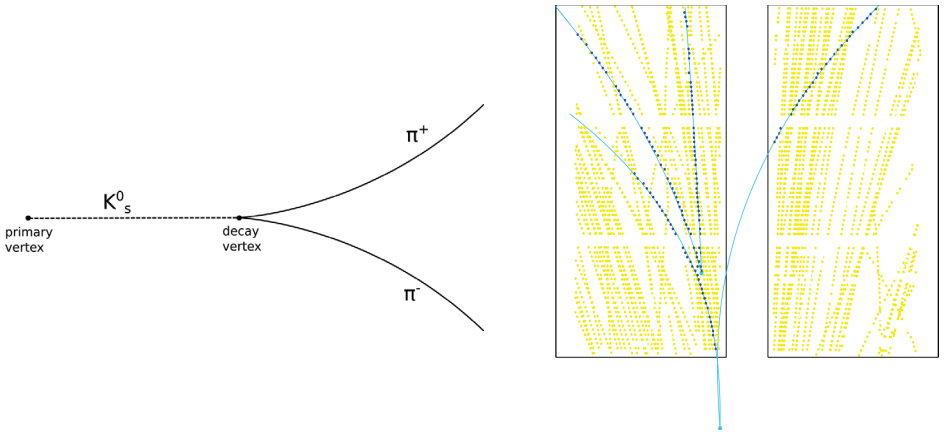


**Figure 3.2:** *Left*: Example of V0 topology as for $K^0_S$ decaying into two pions. *Right*: Two reconstructed V0 decays in NA61/SHINE spectrometer. Yellow points are TPC clusters and blue lines represent two reconstructed V0 decays. TPC clusters belonging to V0 daughter tracks are marked as blue points.

### 3.1.2 V0 finder and fitter

The neutral particles traveling through the detector material do not ionize, and thus can not be detected in the NA61/SHINE spectrometer. The only way to measure them is via the decay products (daughter particles). The two-body decays create a characteristic V shape – two particle tracks originating from one decay point. It is presented in the left panel of Fig. 3.2. The right panel of Fig. 3.2 shows the V0 topology as reconstructed in the NA61/SHINE spectrometer.

The first step of the reconstruction of V0 candidates is the V0 finder. It loops over the pairs of tracks which do not originate from the primary vertex. For each pair of tracks a Distance of Closest Approach (DCA) is estimated. The DCA is the smallest distance between the two tracks. In order to estimate the DCA, the space is divided into 1 cm slices along the beam axis ($z$ direction). For each slice the distance between tracks is calculated. This step is summarised in the left panel of Fig. 3.3. The $z$ position of the slice with a smallest distance is weighted with the values from the two closest slices calculating $z_c$. It is presented in the right panel of Fig. 3.3. The obtained $z_c$ value is considered as the initial value of the decay vertex position. The distance between the tracks for $z_c$ is the DCA estimation. If the two tracks are close enough to each other (DCA is small enough), they are reconstructed as V0 candidate. Then, the decay vertex is found and the tracks are refitted using the V0 fitter.

## 3.2 Monte Carlo simulations

In the NA61/SHINE experiment, the results of the analyses are corrected for many detector effects, like detection efficiency, detector acceptance, and performance of the reconstruction algorithms. In order to calculate the proper corrections the simulated Monte Carlo data are employed. The

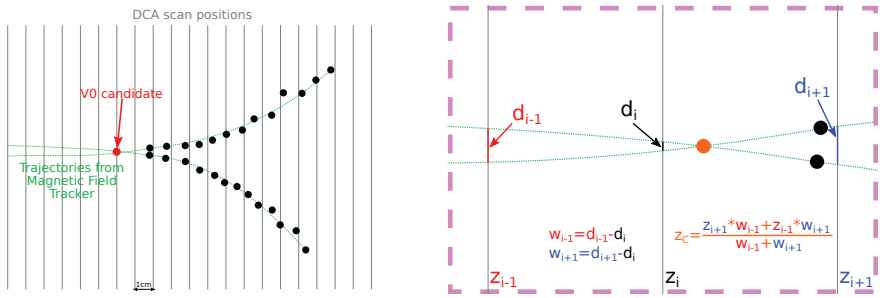


**Figure 3.3:** *Left*: First step of estimation of Distance of Closest Approach between two tracks. Black dots are TPC clusters and green lines represent reconstructed TPC tracks. Distance between tracks is calculated with 1cm granularity. $z$ position with smallest distance is first estimation of decay vertex position. *Right*: Estimation of $z$ position of decay vertex. $z$ value corresponding to smallest distance between tracks found with 1 cm granularity is weighted using two closest points and $z_c$ is calculated. $z_c$ is initial value of decay vertex position along $z$ axis which is then used in V0 fitter.

selection of the Monte Carlo model was based on the performance analysis of different models in the p+p collisions [85]. The selected model EPOS 1.99 [38, 86] guarantees a good agreement with the data as well as the continuous support from the developers. Moreover, the EPOS model simulates the fragmentation of the colliding nuclei which is very useful when analysing the heavy-ion collisions. The simulated particles are propagated through the NA61/SHINE detector using GEometry ANd Tracking (GEANT) framework [87]. The GEANT implementation of the NA61/SHINE detector response is included in the simulation software. The produced detector response is stored in the same format as the collected raw data, so exactly the same reconstruction algorithms can be used. This allows for the comparison between reconstructed experimental and simulated data and calculation of the efficiency corrections. The simulation procedure consists of the following steps:

- simulation of the inelastic ion-ion (e.g. $^{40}$Ar+$^{45}$Sc) collisions using the EPOS model,
- propagation of the simulated particles through the NA61/SHINE detector using the GEANT package,
- reconstruction of the simulated data using the same algorithms as for experimental data.

The output of the MC simulation procedure is stored in two different types of event objects:

- Monte Carlo generated event (MC$_{gen}$) – it contains the information about the simulated particles taken directly from the model, like momentum, species, origin (whether the particle comes from the primary interaction or the decay of other particle),
- Monte Carlo reconstructed event (MC$_{rec}$) – it contains the information from the reconstruction in the same format as for reconstructed experimental data; information starting from the interaction in the target is reconstructed.

Chapter 4

# Ar+Sc datasets

The data on $^{40}$Ar+$^{45}$Sc collisions were registered by the NA61/SHINE experiment in 2015. The data-taking was performed at six different beam momenta: $p_{beam}$ = 13$A$, 19$A$, 30$A$, 40$A$, 75$A$, 150$A$ GeV/$c$. For the whole Ar+Sc data collection, a common configuration of the beam and detector was used. This chapter summarises the used trigger configuration as well as the characteristics of the beam and target.

## 4.1 Trigger

The sub-detectors included in the trigger system for Ar+Sc data-taking campaign are schematically presented in Fig. 4.1. The beam detectors included in the coincidence mode are marked in green and the sub-detectors working in the veto (anti-coincidence) mode are marked in red.

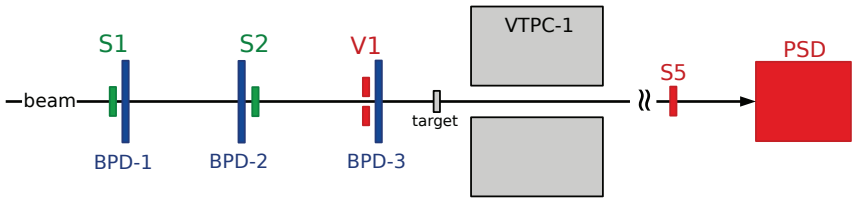


**Figure 4.1:** Layout of sub-detectors included in trigger during Ar+Sc data-taking campaign. Sub-detectors included in coincidence mode are marked in green, while sub-detectors used in anti-coincidence mode are marked in red. Figure from Ref. [72].

Four different trigger configurations were defined: *beam* trigger (T1), *central interaction* trigger (T2), *beam halo* trigger (T3), and *minimum bias interaction* trigger (T4). The definitions of the listed configurations are summarised in Table 4.1. The last column of the table represents the fraction of defined trigger pattern corresponding to the unbiased sample. The sum of the values is higher than 100% as some events might belong to many patterns (for example: some prescaled T1 triggers also belong to the group of prescaled T2 triggers). The fractions were obtained by setting the prescaling factors properly (see Sec. 2.3.4). Most of the registered events correspond to the central interactions in the Ar+Sc collisions.

| Name | Definition | Description | Fraction of data |
|---|---|---|---|
| T1 | $S1 \cdot S2 \cdot \overline{V1}$ | beam | 1.16% |
| T2 | $S1 \cdot S2 \cdot \overline{V1} \cdot \overline{S5} \cdot \overline{PSD}$ | central interaction | 92.61% |
| T3 | $S1 \cdot S2$ | beam halo | 0.18% |
| T4 | $S1 \cdot S2 \cdot \overline{V1} \cdot \overline{S5}$ | min. bias interaction | 7.13% |

**Table 4.1:** Trigger definitions used in Ar+Sc data-taking campaign.

## 4.2 Beam

The $^{40}$Ar beam used during the Ar+Sc data-taking campaign, was the primary beam accelerated by the CERN accelerator complex. After the last step of acceleration in the SPS, the beam was transported to the NA61/SHINE experiment via the H2 beam line. From the SPS, the beam was extracted in slow extraction mode, resulting in 10 s spill duration. After the spill there was around 30 s break. Thus, the beam duty cycle was about 25%.

### 4.2.1 Beam profile

The trajectory of the beam is measured by three Beam Position Detectors (BPDs). The measured points are fitted with a straight line in order to reconstruct the beam particle trajectory. Figure 4.2 shows the beam position on the target $z$ position reconstructed in the Ar+Sc collisions at 75$A$ GeV/$c$. The visible structures come from the read-out granularity of the BPDs. The circular shape around the beam center is caused by the hole in the V1 detector included in the trigger system.

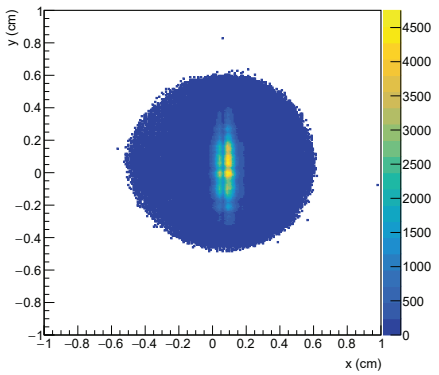


**Figure 4.2:** Beam profile at target $z$ position in collected Ar+Sc collisions at 75$A$ GeV/$c$.

### 4.2.2 Beam time structure

The time structure of the beam particles is presented in Fig. 4.3. It was created from the data registered by the Multi-hit Time to Digital Converter (MHTDC) module which is able to register the timing of different signals around the triggering particle. The figure shows the time distribution

of the particles hitting the S1 detector close in time to the triggering particle. The sharp peak at zero corresponds to triggering particle. The region with lower number of entries before the triggering particle comes from ToF *fast-clear* mechanism. Since the ToF detectors require faster trigger, the read-out is triggered on S1 signal before the final trigger decision. If the S1 signal is not followed by the accepted trigger, the ToF read-out has to be cleared which takes about 3 µs. During the fast-clear procedure, the ToF read-out is busy and thus, no trigger can be accepted. The entries present in that region of the distribution come from the beam particles hitting S1 during the process of ToF fast-clear. The read-out window of the S1 counter is around 100 ns. This causes the short region with no entries after the triggering particles peak. Except of the two mentioned regions, the time distribution of the beam extracted from SPS is flat. The flat time structure of the beam is desired as it minimises the probability of registering multiple particle interactions in one event – so-called pileup.

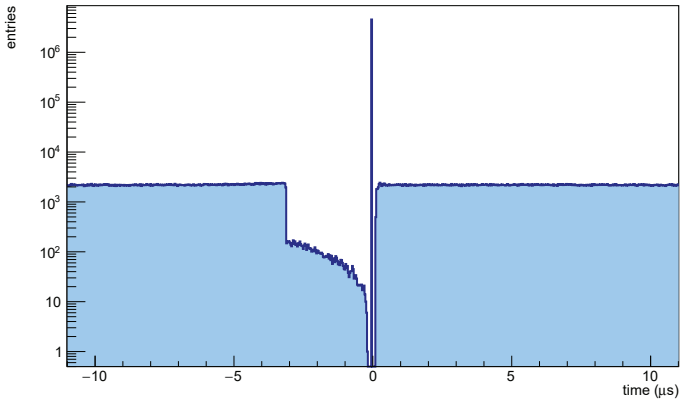


**Figure 4.3:** Time structure of beam particles hitting S1 counter in proximity of triggering particle in Ar+Sc collisions at 75$A$ GeV/$c$. Peak at zero corresponds to triggering particle.

## 4.3 Target

The $^{45}$Sc target used in the Ar+Sc data-taking at 40$A$ GeV/$c$ and 75$A$ GeV/$c$ consisted of 6 square layers with a size of 2 cm x 2 cm and the thickness of 1 mm. It was installed at $z = -580$ cm in the NA61/SHINE coordinate system in a dedicated helium box. The purpose of the helium presence in the target proximity is to reduce the number of interactions of the beam particles with the air (so-called off-target interactions). The helium box was integrated with a pneumatic movable system. It allows to collect the data in two modes: with (Target-IN) and without (Target-OUT) the target inserted. The Target-OUT data are used to estimate the impact of the off-target interactions on the analysis results.

In the fixed-target experiments the usage of highly pure targets is desired. The contamination of the NA61/SHINE targets is measured using Wavelength Dispersive X-Ray Fluorescence (WDXRF) method. The purity of $^{45}$Sc target was measured at the Jan Kochanowski University in Kielce, Poland. The content of $^{45}$Sc in the used target was at the level of 99.3%. The contamination of the target was identified as: Ti (0.16%), Al (0.14%) Fe (0.13%), Cu (0.07%), and Ta (0.07%). The impact of the target impurities on the negatively charged particle multiplicities was estimated to be less than 0.2% [88]. The impact on the positively charged particles was assumed to be on the same level. As the systematic uncertainty corresponding to this effect is over one order of magnitude smaller in comparison to other sources, it was neglected in the total systematic uncertainty calculation.

Chapter 5

# Analysis

The main results of the presented analyses are the rapidity [(a)] – transverse momentum spectra of $K^0_S$ mesons produced in the 10% most central $^{40}$Ar+$^{45}$Sc collisions at 40$A$ GeV/$c$ and 75$A$ GeV/$c$ ($\sqrt{s_{NN}} = 8.77$ GeV and $\sqrt{s_{NN}} = 11.94$ GeV). The $K^0_S$ mesons can be studied by measuring the properties of their decay products. In order to estimate the multiplicity of the $K^0_S$ in a given kinematic bin, the invariant mass distribution is created for all the V0 decay candidates from a given kinematic bin. The invariant masses of the candidates coming from $K^0_S$ decays contribute to the peak close to the mass of $K^0_S$. The other candidates (pairs) contribute to the background. Then, the distribution is fitted with the proper signal and background functions. The integral of the signal function divided by the bin width is equal to the *raw* (uncorrected) number of the reconstructed $K^0_S$ in a given kinematic bin. This chapter summarises the steps of the analysis process. At first, the binning procedure is discussed (Sec. 5.1). As the highest possible quality of the data is desired, the event selection (Sec. 5.2) and track selection (Sec. 5.3) is performed. The process of invariant mass spectra analysis is discussed in Sec. 5.4. The procedure of optimization of rapidity dependent cuts is presented in Sec. 5.5. Then, Sec. 5.6 describes the procedure of calculating the corrections based on MC data. Last Sec. 5.7 summarizes the procedure of calculating the statistical and systematic uncertainties. The technical plots presented in this chapter were prepared for Ar+Sc collisions at 75$A$ GeV/$c$. The same cut values were used for both studied beam momenta of the Ar+Sc collisions (40$A$ GeV/$c$ and 75$A$ GeV/$c$), unless specified differently.

## 5.1 Binning

The results of the analyses are corrected for detector and reconstruction inefficiencies. In order to make the MC corrections model independent, the analysis is performed in rapidity and transverse momenta bins. The smaller the bins are, the more reliable results can be obtained. The size of the bins is however determined by the available statistics. Thus, the selected binning size is the compromise which ensures that the bins are as small as possible and the data statistics for each bin is sufficient.

The phase space was divided into bins in the following way:

- for 40$A$ GeV/$c$:
  - 6 bins in rapidity from -1 to 2,

[(a)] In this thesis $K^0_S$ rapidity is always given in collision CMS.

    - 8 bins in transverse momentum from 0 to 2.4 GeV/$c$.
- for 75$A$ GeV/$c$:
    - 7 bins in rapidity from -1.5 to 2,
    - 9 bins in transverse momentum from 0 to 2.7 GeV/$c$.

The final bins accepted in the analyses can be found in Figs. 6.5 and 6.6 (Chapter 6), which present the already corrected $y$–$p_T$ spectra for Ar+Sc collisions at 40$A$ GeV/$c$ and 75$A$ GeV/$c$.

## 5.2 Event selection

In order to ensure the best possible quality of the data and proper centrality selection, a set of event selection cuts was applied. The analysis was performed on the sub-sample of the events that were collected with the T2 trigger configuration (the $\approx 35\%$ most central events for 40$A$ GeV/$c$ and the $\approx 20\%$ most central events for 40$A$ GeV/$c$). The event selection cuts can be sub-divided into two groups: non-biasing cuts and biasing cuts. The first group concerns the variables that do not depend on the interaction properties, namely the beam quality and beam time structure. The second group refers to the off-target interactions, reconstruction capabilities and centrality selection.

### 5.2.1 Non-biasing event cuts

The group of non-biasing event cuts consists of two following cuts:

1) beam off-time cut,
2) beam quality cut.

These cuts ensure the quality of the measured beam trajectory as well as registration of a single collision in one event. They were applied sequentially and are described in details below.

**Beam off-time cut**

The beam off-time cut removes the events in which there was an additional beam particle close in time to the triggering particle, that could interact with the target or the detector material. It ensures that there is no pile-up in the analysed events. The beam off-time cut is defined by the time range and the signal type. The event is removed from the analysis if a given signal arrives within a defined time interval around the triggering particle. For this analysis, the cut is defined for two types of signals: presence of additional beam particle (S1) and a minimum bias interaction (T4). For the first signal, the time interval is set to $\pm 4$ µs and for the second one to $\pm 25$ µs. If there is an additional beam particle present within the time of $\pm 4$ µs around the triggering particle or additional minimum bias interaction happens within the time of $\pm 25$ µs around the triggering particle, the event is removed from the analysis. The off-time particle registration has a dead time of 100 ns. The possible contamination by the off-time events not registered because of a dead time was estimated to be at the level of 0.01%. As it is few orders of magnitude lower than the other contributions taken into account when calculating the systematic uncertainties, this effect

was neglected.

**Beam quality cut**

The beam quality cut ensures that the trajectory of the beam particle is precisely reconstructed. It requires the measurement of the beam position in BPD-3 and at least one of the two remaining BPDs (BPD-1 or BPD-2). Then, it is possible to fit the beam particle trajectory and extrapolate it to the target region. It also ensures, that the beam particle interaction did not happened upstream of the BPD-3 which is close to the target.

### 5.2.2 Biasing event cuts

The group of biasing event cuts includes the following cuts:

1) cut on the properties of the primary vertex,
2) centrality selection cut.

This group of cuts is used to reduce the background from off-target events and select the centrality of the collisions. They can potentially bias the results of the analysis. Thus, their influence is studied carefully using Monte Carlo data.

**Primary vertex properties**

Events included in the analysis must have a well defined interaction point. Two selection criteria were applied concerning the properties of primary vertex.

The first cut ensures the quality of the fit. The $x$ and $y$ positions of the primary vertex are extracted from the BPD tracks, while the $z$ position comes from the fit of extrapolated TPC tracks. The events are accepted for the analysis, if the fitting procedures converge and the primary vertex is reconstructed.

The second cut removes most of the off-target interactions. This cut is imposed on the $z$ position of the primary vertex. The distribution of the primary vertex $z$ position is shown in Fig. 5.1. The plot presents the distributions for the data collected with the target inserted (Target-IN) and target removed (Target-OUT). Events with primary vertex $z$ position located within $\pm 2$ cm with respect to the target position, were accepted for the analysis. The cut values are marked with dashed lines in Fig. 5.1. The selection of cut values was based on the distribution for the 10% most central collisions (plotted as shaded area on darker blue). The maxima visible in the distributions, correspond to different detector elements. The sharp peak coming from the interactions in the target is only present in Target-IN data. Other detector structures are present in both Target-IN and Target-OUT data. Target-OUT data were scaled so the integral over the range $z < -620$ cm is the same as for Target-IN data.

**Centrality selection**

The analyses presented in this thesis were performed for the 10% most central Ar+Sc collisions at $40A$ GeV/$c$ and $75A$ GeV/$c$. The selection of the event centrality was done based on the information

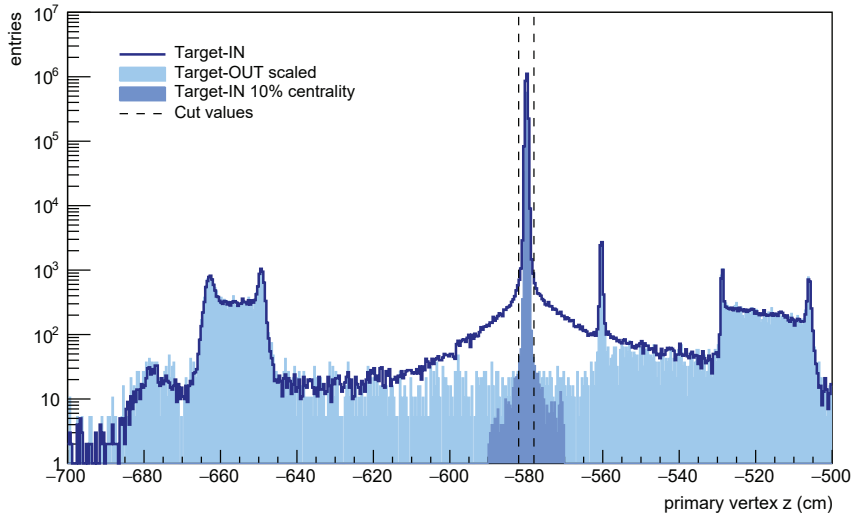


**Figure 5.1:** Distribution of $z$ position of primary vertex for Ar+Sc collisions at 75$A$ GeV/$c$. Solid line represents Target-IN data; light blue histogram represents scaled Target-OUT data. Dashed lines correspond to range of values accepted for analysis. Cut selection was based on Target-IN data for 10% most central collisions presented as shaded area on darker blue. Distributions are plotted after beam off-time cut and beam quality cut.

from the PSD detector. It measures the energy deposit of the projectile spectators as well as the hadrons produced within the PSD acceptance. This section presents the brief description of centrality selection procedure. The detailed description can be found in Refs. [34, 89, 90].

The information from the PSD was included in the T2 trigger definition in order to select mostly the central collisions for the permanent storage. The integrated signal from 16 central modules was used with a properly selected threshold value. The off-line procedure of precise centrality selection was developed using PSD data and special sub-samples of minimum bias events.

The first step of the centrality determination is the selection of the PSD modules that are used. For this purpose, the mean energy deposit as a function of track multiplicity is plotted for each module. The example distributions are presented in the left and middle panels of Fig. 5.2. The positive correlation means that the module mostly registers the energy of produced particles (as in the middle panel of Fig. 5.2). The negative correlation is desired and it means that most of the energy deposited in a given module comes from the spectators (as in the left panel of Fig. 5.2). The modules taken into account in the centrality selection for Ar+Sc collisions at 40$A$ GeV/$c$ and 75$A$ GeV/$c$ are presented in the right panel of Fig. 5.2. Using the selected modules a total energy $E_{PSD}$ is calculated.

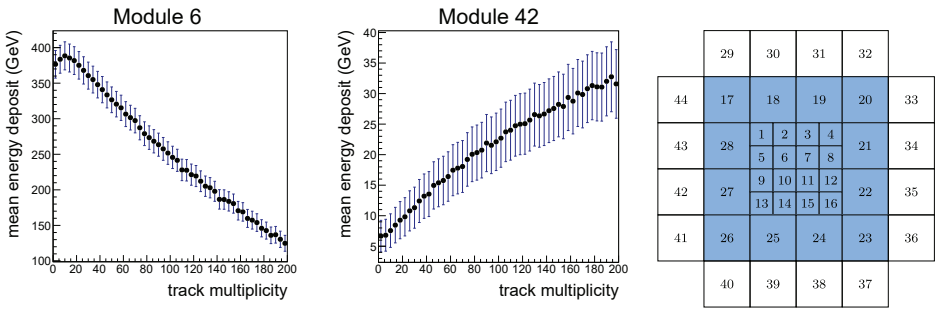


**Figure 5.2:** *Left*: Mean energy deposit measured by Module 6 of PSD as function of TPC track multiplicity for minimum bias Ar+Sc collisions at 75$A$ GeV/$c$. *Middle*: Mean energy deposit measured by Module 42 of PSD as function of TPC track multiplicity for minimum bias Ar+Sc collisions at 75$A$ GeV/$c$. *Right*: PSD modules used in off-line event centrality selection for Ar+Sc collisions at 40$A$ GeV/$c$ and 75$A$ GeV/$c$.

The threshold values of $E_{PSD}$ defining a given centrality class, are calculated based on the minimum bias samples of data. The measured distribution of PSD energy for minimum bias data is plotted in Fig. 5.3. The energy distribution for T2 events is also shown. It was scaled so the integral for small values of PSD energy is the same as for the minimum bias distribution. The threshold for the 10% most central Ar+Sc collisions was set to: $E_{PSD}^{10\%} = 1290.6$ GeV for 75$A$ GeV/$c$ and $E_{PSD}^{10\%} = 665.6$ GeV for 40$A$ GeV/$c$. The events selected for the analysis are required to have a smaller $E_{PSD}$ than the selected threshold for the 10% most central collisions $E_{PSD}^{10\%}$.

The impact of the centrality selection procedure on the results was studied [72] on MC data in order to estimate the possible bias. The detailed description of the procedure is given in Ref. [72]. At first, the minimum bias sample of events was generated with the EPOS 1.99 model. Then, the centrality selection was made based on two different methods. The first method uses the PSD acceptance map [91] to calculate forward energy $E_F$ of particles within the PSD acceptance. The acceptance map defines the 3D acceptance of PSD detector in total momentum $p$, transverse momentum $p_T$ and azimuthal angle $\varphi$ [(b)]. The 10% most central events are defined as 10% of events with the smallest $E_F$. This procedure was also used to select the 10% most central collisions in the SMASH model used for the comparison of the results in Sec. 6.5. The second method of centrality selection uses the simulated PSD response to calculate simulated $E_{PSD}$. Then, for both selection methods the multiplicity of $\pi^-$ mesons was calculated [72]. The observed difference was on the level of 0.5%. According to the Wounded Nucleon Model (WNM) [92], the mean multiplicity of particles is proportional to the mean number of wounded nucleons for a given centrality selection. The difference in mean number of wounded nucleons between the

[(b)] Azimuthal angle is the angle in plane perpendicular to the beam axis between the transverse momentum and the positive $x$ axis.

two centrality selections is small, thus the scaling is assumed to be valid. Consequently, the same scaling is assumed for other particles. As a result, the 0.5% difference can be considered as a possible bias of the centrality selection on the results. This value is smaller by an order of magnitude from the other estimated contributions to the systematic uncertainty and thus was neglected in the calculation of final systematic uncertainty.

In this thesis, the centrality selection in the analysis of data generated by EPOS was based on the number of participants provided in the output of the model. The threshold on the number of participants was selected to accept the 10% most central Ar+Sc collisions for the analysis.

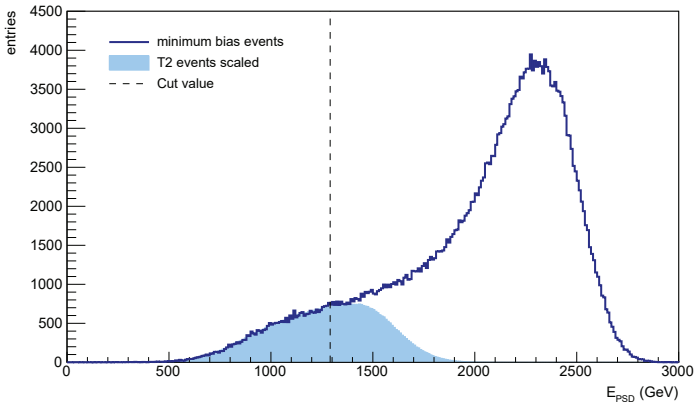


**Figure 5.3:** Measured distribution of PSD energy deposit for minimum bias events (blue line) and scaled T2 events (shaded blue area) without any event selection for Ar+Sc collisions at 75$A$ GeV/$c$. Dashed line corresponds to threshold for 10% most central collisions.

### 5.2.3 Event statistics

The event cuts described above were applied on the experimental data as well as the reconstructed MC data sequentially. The statistics of the events accepted after each cut is summarized in Table 5.1. The cuts were also applied on the Target-OUT data. The majority of those events were rejected by the selection cuts. Thus, the possible bias from off-target interactions was neglected in the analysis.

## 5.3 Track selection

For the events accepted in the analysis, the V0 candidates are reconstructed. The candidates further taken into account must fulfill the track selection criteria. The track cuts can be divided into two groups: single track cuts and pair track cuts. Single track cuts correspond to the properties of the reconstructed daughter particles and are applied separately for each daughter track. Pair track cuts correspond to the properties reconstructed from the two tracks assigned to V0 candidate

| $p_{beam}$ | cut | Target-IN | Target-OUT | MC$_{gen}$ | MC$_{rec}$ |
|---|---|---|---|---|---|
| 40$A$ GeV/$c$ | - | $6.4 \cdot 10^6$ (100%) | $2.1 \cdot 10^5$ (100%) | $18 \cdot 10^6$ (100%) | $18 \cdot 10^6$ (100%) |
| | beam off-time | $5.4 \cdot 10^6$ (84%) | $8.7 \cdot 10^4$ (41%) | - | - |
| | beam quality | $5.3 \cdot 10^6$ (83%) | $7.2 \cdot 10^4$ (34%) | - | - |
| | primary vertex properties | $4.6 \cdot 10^6$ (72%) | 151 (0.07%) | - | $17 \cdot 10^6$ (94%) |
| | centrality selection | $1.3 \cdot 10^6$ (20%) | 2 (0.001%) | $1.8 \cdot 10^6$ (10%) | $1.8 \cdot 10^6$ (10%) |
| 75$A$ GeV/$c$ | - | $2.9 \cdot 10^6$ (100%) | $1.8 \cdot 10^5$ (100%) | $19 \cdot 10^6$ (100%) | $19 \cdot 10^6$ (100%) |
| | beam off-time | $2.4 \cdot 10^6$ (83%) | $4.6 \cdot 10^4$ (26%) | - | - |
| | beam quality | $2.3 \cdot 10^6$ (79%) | $3.8 \cdot 10^4$ (21%) | - | - |
| | primary vertex properties | $2.2 \cdot 10^6$ (76%) | 37 (0.02%) | - | $18 \cdot 10^6$ (95%) |
| | centrality selection | $1.1 \cdot 10^6$ (38%) | 2 (0.001%) | $1.9 \cdot 10^6$ (10%) | $1.9 \cdot 10^6$ (10%) |

**Table 5.1:** Summary of number of events after event selection cuts. Percentage of statistics accepted after each cut is given in brackets. For both beam momenta, final number of MC$_{rec}$ events is 0.1% smaller than number of MC$_{gen}$ events (precision of values given in table is not high enough to see this difference). It means that cut on primary vertex properties rejects very small fraction of 10% most central events.

(candidate for neutral particle decaying into two daughter particles). The track selection cuts are described in details in the sections below.

### 5.3.1 Single track cuts

The single track cuts group includes the following cuts:

1) number of reconstructed VTPC clusters cut,
2) cut on minimum momentum.

**Number of reconstructed VTPC clusters**

The cut on the number of reconstructed VTPC clusters ensures the good quality of the reconstructed momenta of the particles. The tracks are accepted in the analysis if the sum of number of clusters reconstructed in both VTPCs is higher than 10.

**Minimum momentum**

The cut on minimum total momentum of the particle (in NA61/SHINE laboratory frame) is applied in order to reduce the background coming mainly from the low-momenta electrons. The track is accepted in the analysis if the total momentum is higher than 0.4 GeV/$c$. The impact of this cut is presented in Fig. 5.4 in the Armenteros-Podolanski plot. The details of Armenteros-Podolanski plot are described in Sec. 1.5. The left panel shows the plot before applying the minimum momentum cut and the right panel after applying the cut. The cut reduces significantly the background present for low values of $p_T^{Arm}$ and peripheral values of $\alpha^{Arm}$ (bottom corners of the plot).

### 5.3.2 Pair track cuts

The pair track cuts are applied in order to increase the $K_S^0$ signal to background ratio in the invariant mass spectra. The values of those cuts are optimised for each $K_S^0$ rapidity bin separately.

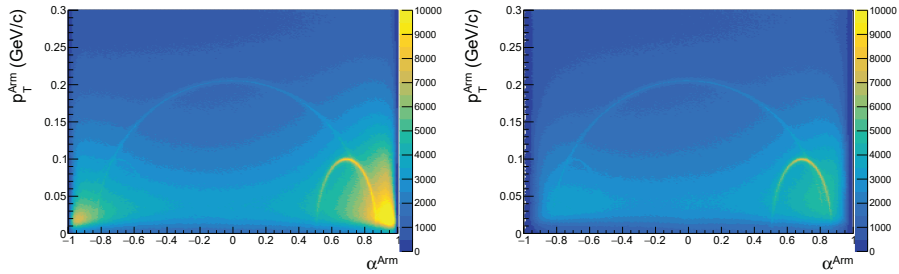


**Figure 5.4:** *Left*: Armenteros-Podolanski plot without minimum momentum cut applied. *Right*: Armenteros-Podolanski plot with minimum momentum cut applied. Both plots were prepared for Ar+Sc collisions at 75$A$ GeV/$c$ for all accepted events and all other track cuts included.

The optimization procedure is described below. The group of pair track cuts consists of the following cuts:

1) directional angle cut,
2) cut on distance between primary and decay vertex.

**Directional angle**

The directional angle is the angle between the V0 mother momentum and the line joining the primary vertex and the decay vertex. The cut is applied on the cosine value of the directional angle. For the two body decays the cosine of directional angle should be equal to one. The cosine of directional angle is calculated from the following formula (variables used in the formula are explained in the left panel of Fig. 5.5):

$$\cos(\alpha) = \frac{\overrightarrow{vtx} \cdot \overrightarrow{p_{K0s}}}{|\overrightarrow{vtx}||\overrightarrow{p_{K0s}}|}. \tag{5.1}$$

This cut ensures the proper decay topology for the V0 candidates taken into account in the analysis. The distribution of the cosine of the directional angle for the V0 candidates reconstructed in the Ar+Sc collisions at 75$A$ GeV/$c$ is shown in the right panel of Fig. 5.5. The values of the cut are optimized in each $K^0_S$ rapidity bin to minimise the statistical uncertainty of the final result. The optimization procedure is discussed in Sec. 5.5. Table 5.2 summarises the values of the cut in the rapidity bins taken into account in the analysis.

| rapidity bin | | $(-1.5,-1)$ | $(-1,-0.5)$ | $(-0.5,0)$ | $(0,0.5)$ | $(0.5,1)$ | $(1,1.5)$ | $(1.5,2)$ |
|---|---|---|---|---|---|---|---|---|
| cut value | 40$A$ GeV/$c$ | - | >0.9995 | >0.9995 | >0.9995 | >0.9999 | >0.9999 | >0.9999 |
| | 75$A$ GeV/$c$ | >0.999 | >0.9995 | >0.9995 | >0.9995 | >0.9995 | >0.9999 | >0.9999 |

**Table 5.2:** Values of directional angle cut in rapidity bins used for analysis of Ar+Sc collisions at 40$A$ GeV/$c$ and 75$A$ GeV/$c$.

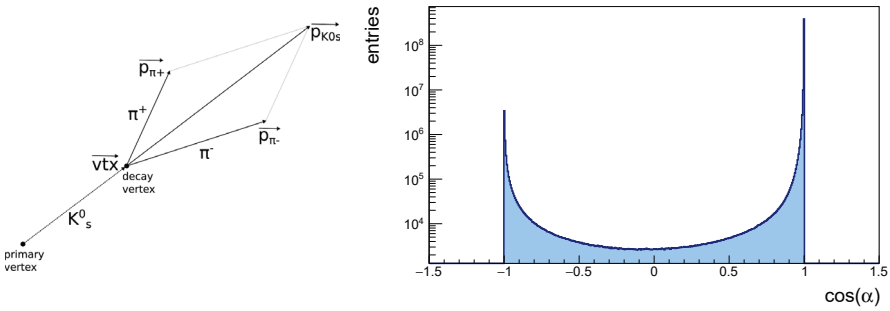


**Figure 5.5:** *Left*: V0 topology defining variables used to calculate directional angle. *Right*: Distribution of cosine of directional angle for V0 candidates reconstructed in Ar+Sc collisions at 75$A$ GeV/$c$ for all accepted events and both single track cuts applied.

**Distance between primary and decay vertex**

This cut defines the minimum distance between the primary vertex and decay vertex. The distance between the vertices can be calculated from the following formula (variables used in the formula are explained in the left panel of Fig. 5.6):

$$\Delta L = \left|\overrightarrow{vtx}\right| = \sqrt{\sum_{i=x,y,z} (\text{decay\_vertex}_i - \text{primary\_vertex}_i)^2} \tag{5.2}$$

The cut reduces the contribution of primary tracks reconstructed as V0 candidates. The distribution of the $\Delta L$ for the V0 candidates reconstructed in the Ar+Sc collisions at 75$A$ GeV/$c$ is presented in the right panel of Fig. 5.6. The values of the cut are optimized for each $K^0_S$ rapidity bin. Table 5.3 summarises the values of the cut in the rapidity bins taken into account in the analysis.

| rapidity bin | | $(-1.5,-1)$ | $(-1,-0.5)$ | $(-0.5,0)$ | $(0,0.5)$ | $(0.5,1)$ | $(1,1.5)$ | $(1.5,2)$ |
|---|---|---|---|---|---|---|---|---|
| cut value | 40$A$ GeV/$c$ | - | >5cm | >5cm | >10cm | >12.5cm | >15cm | >10cm |
| | 75$A$ GeV/$c$ | >5cm | >5cm | >7.5cm | >12.5cm | >12.5cm | >15cm | >12.5cm |

**Table 5.3:** Values of cut on distance between primary and decay vertex in rapidity bins used for analysis of Ar+Sc collisions at 40$A$ GeV/$c$ and 75$A$ GeV/$c$.

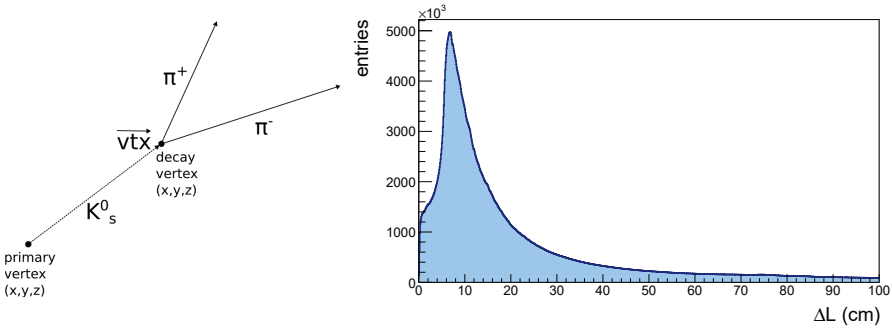


**Figure 5.6:** *Left*: V0 topology defining variables used to calculate distance between primary and decay vertex. *Right*: Distribution of distance between primary and secondary vertex for V0 candidates reconstructed in Ar+Sc collisions at 75$A$ GeV/$c$ for all accepted events and both single track cuts applied.

Figure 5.7 presents the Armenteros-Podolanski plot created for all V0 candidates accepted for the analysis (including additionally the cut on the range of invariant mass – see Sec. 5.4) in Ar+Sc collisions at 75$A$ GeV/$c$.

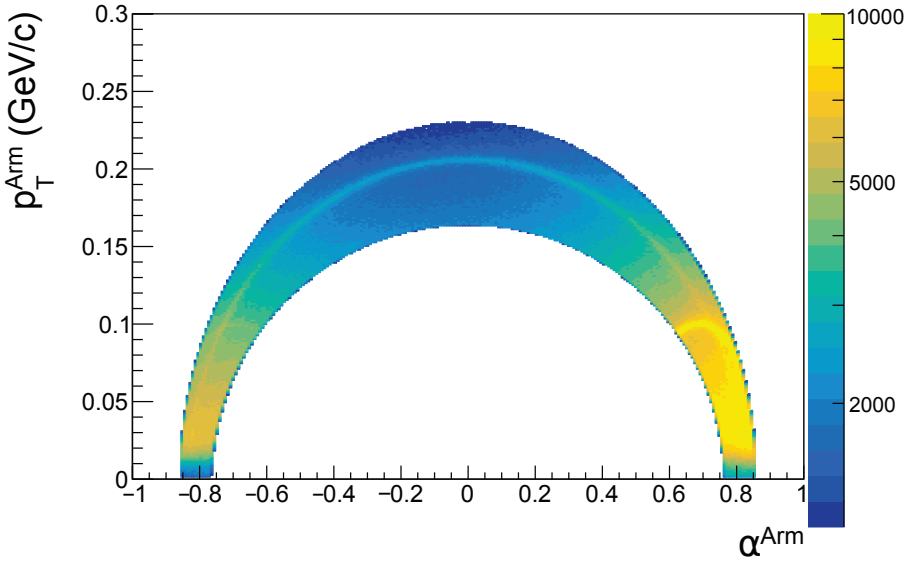


**Figure 5.7:** Armenteros-Podolanski plot for all V0 candidates accepted for analysis after event and track cuts (including additionally cut on invariant mass – see Sec. 5.4) for Ar+Sc collisions at 75$A$ GeV/$c$.

## 5.4 Raw $K^0_S$ yields

In order to estimate the raw (uncorrected) number of $K^0_S$ mesons in a given kinematic bin, the invariant mass distribution is created for all the V0 candidates which passed the selection criteria. For a given V0 candidate the invariant mass is calculated using the following formula ($c \equiv 1$ is assumed):

$$m(\pi^+\pi^-) = \sqrt{\left(E_{\pi^+} + E_{\pi^-}\right)^2 - \left(\overrightarrow{p_{\pi^+}} + \overrightarrow{p_{\pi^-}}\right)^2}, \tag{5.3}$$

where $E_{\pi^+}$ and $E_{\pi^-}$ are the energies of decay products, and $\overrightarrow{p_{\pi^+}}$ and $\overrightarrow{p_{\pi^-}}$ are their momenta. The V0 candidates corresponding to $K^0_S$ decays contribute to the peak close to the mass of $K^0_S$ meson and other V0 candidates taken into account contribute to the background. The example invariant mass distribution is presented in Fig. 5.8.

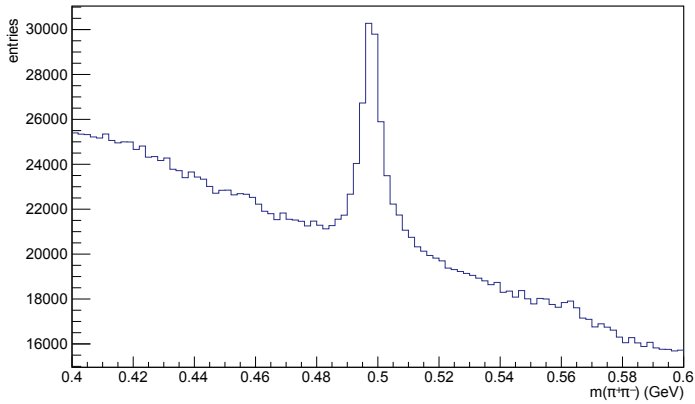


**Figure 5.8:** Example invariant mass distribution of V0 candidates accepted for analysis in Ar+Sc collisions at 75$A$ GeV/$c$ for $y \in (0.0, 0.5)$, $p_T \in (0.6, 0.9)$ GeV/$c$.

The obtained invariant mass spectra are fitted with a sum of signal and background functions:

$$f(x) = \mathrm{BW}(x) + \mathrm{Ch}_3(x), \tag{5.4}$$

where $x \equiv m(\pi^+\pi^-)$ (for simplifying the notation), $\mathrm{BW}(x)$ and $\mathrm{Ch}_3(x)$ are signal and background functions, respectively. For the fitting, the RooFit [93] package was used. The signal is described using the RooFit implementation of the non-relativistic Breit-Wigner function:

$$\mathrm{BW}(x) = A_S \cdot \frac{1}{(x-\mu)^2 + 0.25\sigma^2}, \tag{5.5}$$

where $A_S$ is the normalisation factor, $\mu$ is the mean, and $\sigma$ is the half-width at half-maximum.

The background is described by the third order Chebychev polynomial curve, defined as:

$$\mathrm{Ch}_3(x) = A_B \cdot \sum_{n=0}^{n=3} pn \cdot u_n, \tag{5.6}$$

where $A_B$ is the normalisation factor, $pn$ are the polynomial coefficients and $p0 = 1$, and $u_n$ can be defined recursively:

$$\begin{aligned} u_0 &= 1, \\ u_1 &= x, \\ u_{n+1} &= 2x \cdot u_n - u_{n-1}. \end{aligned} \tag{5.7}$$

The fitting range was selected by the following constrains: $m(\pi^+\pi^-) > 0.43$ GeV and $m(\pi^+\pi^-) < 0.54$ GeV. The example fitted distributions of the invariant mass of V0 candidates are shown in Fig. 5.9. The integral of the fitted signal function (red curve in Fig. 5.9) divided by the bin width is considered as a raw number of $\mathrm{K}^0_\mathrm{S}$ mesons in a given kinematic bin ($n_{\mathrm{K}^0_\mathrm{S}}$). It is denoted as yield_signal in Fig. 5.9 and $S$ in Sec. 5.5. The integral of the fitted background function divided by the bin width is denoted as yield_bkg in Fig. 5.9 and $B$ in Sec. 5.5. In RooFit framework yields (integrals of the functions divided by bin width) are treated as fit parameters. Thus, they are provided by the framework together with their statistical uncertainties. The raw (uncorrected) $y$–$p_T$ spectrum for Ar+Sc collisions at 75$A$ GeV/$c$ is shown in Fig. 5.10.

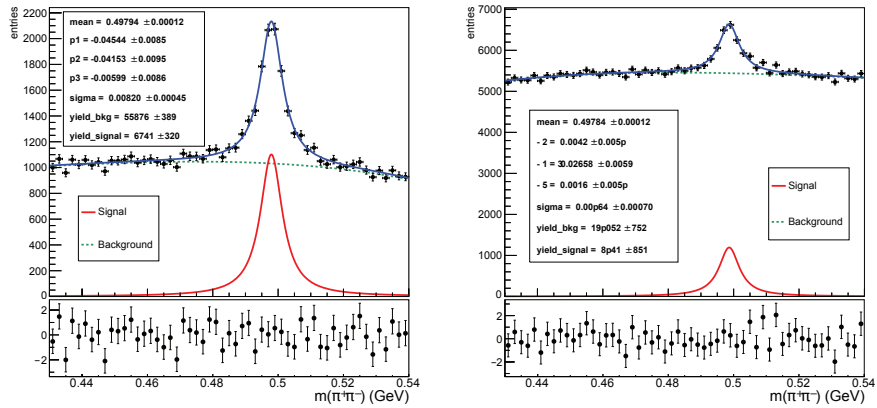


**Figure 5.9:** Example fitted invariant mass distributions for Ar+Sc collisions at 75$A$ GeV/$c$ for $y \in (-1.0, -0.5)$, $p_T \in (1.2, 1.5)$ GeV/$c$ (*Left*) and for $y \in (0.5, 1.0)$, $p_T \in (1.2, 1.5)$ GeV/$c$ (*Right*).

## 5.5 Cuts optimization procedure

The optimization of the rapidity dependent cuts is done on reconstructed MC data. It is performed in each rapidity bin independently. For a given rapidity bin, different values of the cut are checked. For a given cut value, the invariant mass spectra are obtained and then, the signal significance is

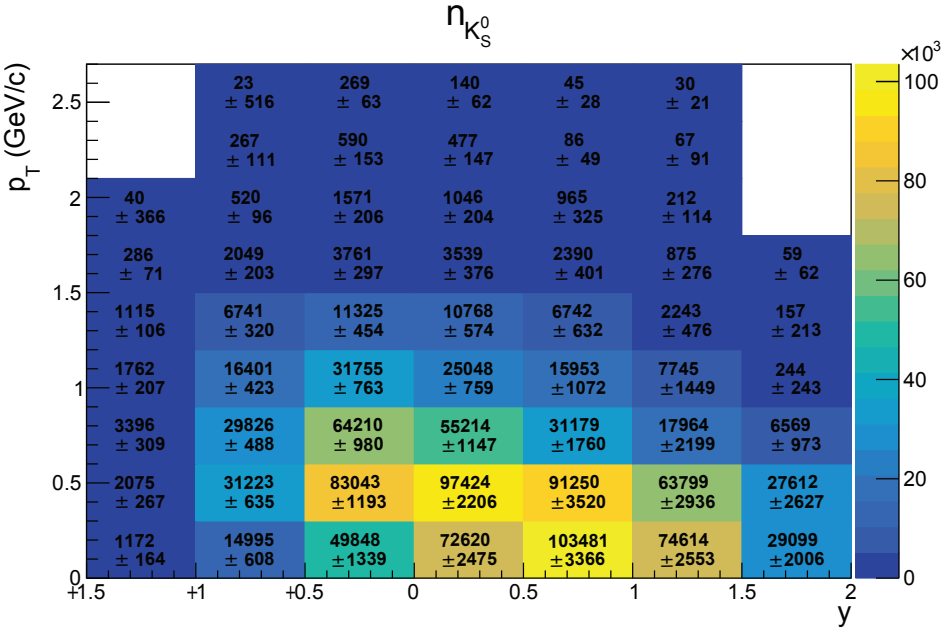


**Figure 5.10:** Raw (uncorrected) $y$–$p_T$ yields of $K^0_S$ mesons in Ar+Sc collisions at 75$A$ GeV/$c$ with statistical uncertainties (see Sec. 5.7.1).

calculated from the following formula:

$$\text{Significance} = \frac{S}{\sqrt{S+B}}, \tag{5.8}$$

where $S$ is the integral of signal function divided by bin width and $B$ is the integral of background function divided by bin width. The cut value which maximizes the signal significance, keeping the signal as high as possible, is selected for the analysis. The following values were checked for directional angle cut: 0.99, 0.995, 0.999, 0.9995, 0.9999, 0.99995, 0.99999, 0.999995, 0.999999 (numbered from 1 to 9 in Fig. 5.11). The optimization of the cut on distance between primary and decay vertex was performed on the following versions of the cut: 5, 7.5, 10, 12.5, 15, 17.5, 20, 22.5, 25, 27.5 cm. The example dependencies of the signal significance and signal yield as a function of directional angle cut version are presented in Fig. 5.11.

## 5.6 Corrections

In order to correct the results for losses due to detection and data processing inefficiencies, detailed Monte Carlo simulations were performed. The description of Monte Carlo simulation procedure can be found in Sec. 3.2. The simulated data are reconstructed and analysed using the same software as for experimental data. The branching ratio of $K^0_S$ meson decays is taken into account

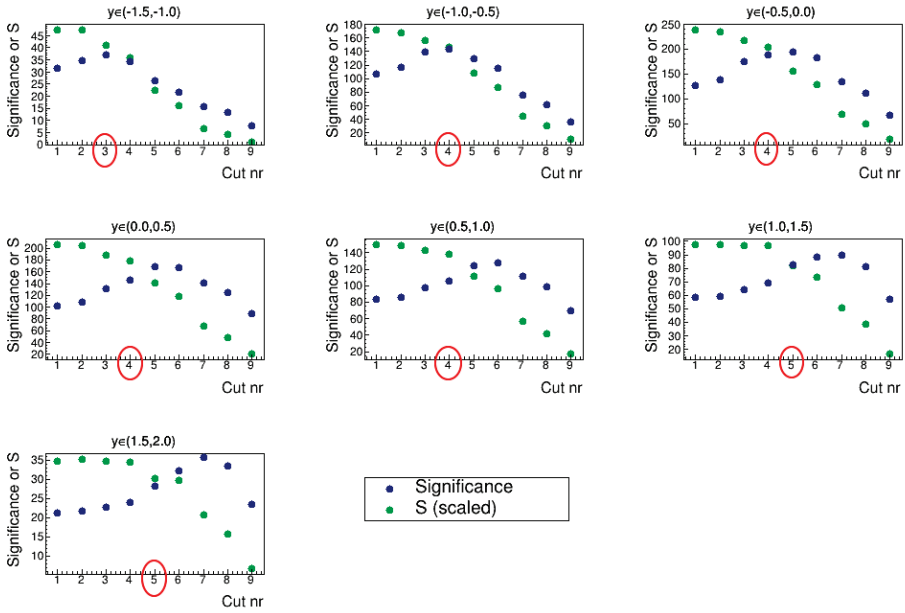


**Figure 5.11:** Example dependencies of signal significance and signal yield as function of directional angle cut version for Ar+Sc collisions at 75$A$ GeV/$c$ after event selection cuts and single track cuts applied. Distribution of signal yield was scaled so integral is the same as for signal significance distribution. Selected cut version for analysis is marked by red circle.

in the GEANT framework. For each rapidity and transverse momentum bin, the correction factor was calculated from the following formula:

$$c_{MC}(y,p_T) = \frac{n^{gen}_{MC}(y,p_T)}{N^{gen}_{MC}} \Big/ \frac{n^{acc}_{MC}(y,p_T)}{N^{acc}_{MC}}, \tag{5.9}$$

where:
$n^{gen}_{MC}(y,p_T)$ – number of generated $K^0_S$ in a given kinematic bin,
$n^{acc}_{MC}(y,p_T)$ – raw number of reconstructed $K^0_S$ in a given kinematic bin (this number is obtained by performing the same analysis as for experimental data; the procedure is described in Sec. 5.4),
$N^{gen}_{MC}$ – number of the 10% most central generated MC events,
$N^{acc}_{MC}$ – number of accepted MC events after the event cuts.

The double-differential yield of $K^0_S$ mesons (per event) in $y$–$p_T$ bin was calculated from the following formula:

$$\frac{d^2n}{dydp_T}(y,p_T) = \frac{c_{MC}(y,p_T)}{\Delta y \Delta p_T} \cdot \frac{n_{K^0_S}(y,p_T)}{N_{evt}}, \tag{5.10}$$

where:

$c_{MC}(y, p_T)$ – MC correction factor,
$\Delta y$, $\Delta p_T$ – widths of rapidity and transverse momentum bins,
$n_{\mathrm{K}^0_{\mathrm{S}}}(y, p_T)$ – raw (uncorrected) number of $\mathrm{K}^0_{\mathrm{S}}$ in a given $y$–$p_T$ bin obtained as described in Sec. 5.4,
$N_{evt}$ – number of events accepted in the analysis.

The $y$–$p_T$ distribution of corrections for Ar+Sc collisions at 75$A$ GeV/$c$ is presented in Fig. 5.12.

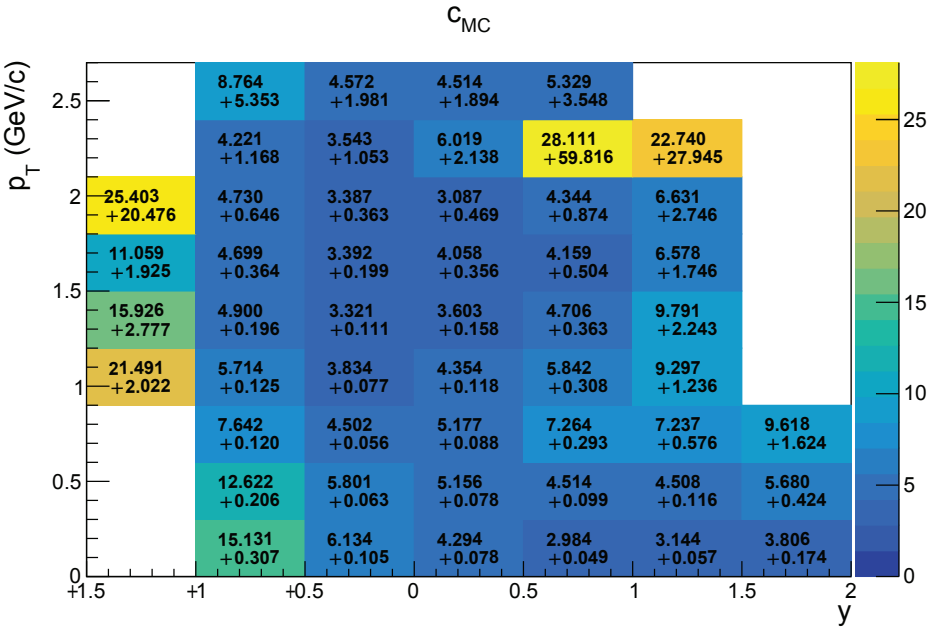


**Figure 5.12:** Distribution of corrections in rapidity and transverse momentum space for Ar+Sc collisions at 75$A$ GeV/$c$ with statistical uncertainties (see Sec. 5.7.1).

## 5.7 Uncertainties

### 5.7.1 Statistical uncertainties

The analysis was performed on finite statistics of the experimental and simulated data. This section summarizes the statistical uncertainties of the results.

The statistical uncertainty of double-differential yield in $y$–$p_T$ has two main contributions. The first one comes from the statistical uncertainty of raw number of $\mathrm{K}^0_{\mathrm{S}}$ mesons ($\Delta n_{\mathrm{K}^0_{\mathrm{S}}}(y, p_T)$ – taken from the fitting procedure) and the second one comes from the statistical uncertainty of correction factor $c_{MC}(y, p_T)$. The statistical uncertainty of correction factor has a contribution

connected to event selection procedure ($\alpha$) and track selection procedure ($\beta$):

$$c_{MC}(y,p_T) = \frac{n^{gen}_{MC}(y,p_T)}{N^{gen}_{MC}} \Big/ \frac{n^{acc}_{MC}(y,p_T)}{N^{acc}_{MC}} = \frac{N^{acc}_{MC}}{N^{gen}_{MC}} \Big/ \frac{n^{acc}_{MC}(y,p_T)}{n^{gen}_{MC}(y,p_T)} = \frac{\alpha}{\beta(y,p_T)}. \tag{5.11}$$

The statistical uncertainty of $\alpha$ is calculated assuming a binomial distribution:

$$\Delta\alpha = \sqrt{\frac{\alpha(1-\alpha)}{N^{gen}_{MC}}}. \tag{5.12}$$

The statistical uncertainty of $\beta$ can be calculated from the following formula:

$$\Delta\beta(y,p_T) = \sqrt{\left(\frac{\Delta n^{acc}_{MC}(y,p_T)}{n^{gen}_{MC}(y,p_T)}\right)^2 + \left(\frac{n^{acc}_{MC}(y,p_T)\cdot\Delta n^{gen}_{MC}(y,p_T)}{(n^{gen}_{MC}(y,p_T))^2}\right)^2}, \tag{5.13}$$

where:
$\Delta n^{acc}_{MC}(y,p_T)$ – the uncertainty of the number of accepted $\mathrm{K^0_S}$ in a given kinematic bin taken from the fit,
$\Delta n^{gen}_{MC}(y,p_T)$ – the uncertainty of the number of generated $\mathrm{K^0_S}$ in a given kinematic bin taken as $\sqrt{n^{gen}_{MC}(y,p_T)}$.
The uncertainty of correction factor can be written as:

$$\Delta c_{MC}(y,p_T) = \sqrt{\left(\frac{\Delta\alpha}{\beta(y,p_T)}\right)^2 + \left(\frac{\alpha\cdot\Delta\beta(y,p_T)}{(\beta(y,p_T))^2}\right)^2}. \tag{5.14}$$

The final statistical uncertainty of double-differential yield in $y$–$p_T$ can be calculated from the following formula:

$$\Delta\frac{d^2n}{dydp_T}(y,p_T) = \sqrt{\left(\frac{c_{MC}(y,p_T)}{N_{evt}\cdot\Delta y\Delta p_T}\right)^2\cdot(\Delta n_{\mathrm{K^0_S}}(y,p_T))^2 + \left(\frac{n_{\mathrm{K^0_S}}(y,p_T)}{N_{evt}\cdot\Delta y\Delta p_T}\right)^2\cdot(\Delta c_{MC}(y,p_T))^2}. \tag{5.15}$$

### 5.7.2 Systematic uncertainties

The systematic uncertainties were estimated only for Ar+Sc collisions at 75$A$ GeV/$c$. The possible systematic bias of the results was estimated by varying each biasing selection criterion independently. The whole analysis was repeated for a modified selection criterion and the results were compared with the nominal results. For each criterion two variations are defined: loose (less restrictive than nominal) and tight (more restrictive than nominal). From these two, the bigger deviation from the nominal result is taken as a contribution to the systematic uncertainty. The final systematic uncertainty is calculated as a square root of the sum of squared contributions (four contributions from Table 5.4, one contribution from Table 5.5, one contribution from Table 5.6, and one contribution from different initial parameters of the invariant mass spectra fit –

see text below). The uncertainties are estimated for each $y$–$p_T$ bin separately.

The ranges of loose and tight cuts compared to nominal values are summarized in Table 5.4. For the event selection, only the cut on the $z$ position of the primary vertex was varied. For the track selection, four cuts were considered as potentially biasing the results: cut on the minimum number of VTPC clusters, cut on minimum momenta of daughter particles, directional angle cut and cut on distance between primary and decay vertex. The last two cuts were varied in each rapidity bin independently. The summary of values for these two cuts can be found in Table 5.5 for directional angle cut and Table 5.6 for the cut on the distance between primary and decay vertex. For the signal extraction procedure, the fitting range of the invariant mass spectra and the initial fitting parameters were varied. The fitting procedure, described in Sec. 5.4, requires the initial values of function parameters ($p1$, $p2$, $p3$, $\mu$, $\sigma$). The result of the fit can slightly vary depending on the initial values of the parameters. Thus, the sets of different bigger and smaller values (with the maximum difference up to 20% in comparison to nominal value) were tested in many different configurations. The maximum deviation from the nominal result was taken into account as a contribution to the systematic uncertainty.

| selection criterion | nominal | loose | tight |
|---|---|---|---|
| primary vertex $z$ cut (Vertex z in Fig. 5.14) | $(-580 \pm 2)$ cm | $(-580 \pm 5)$ cm | $(-580 \pm 1.5)$ cm |
| number of VTPC points (VTPCp in Fig. 5.14) | >10 | >5 | >15 |
| minimum momentum (p in Fig. 5.14) | >0.4 GeV/$c$ | >0.3 GeV/$c$ | >0.5 GeV/$c$ |
| invariant mass fitting range (fitRange in Fig. 5.14) | 0.43–0.54 GeV | 0.4–0.57 GeV | 0.45–0.52 GeV |

**Table 5.4:** Ranges of loose and tight cuts (compared to nominal cut values) used to estimate systematic uncertainties in analysis of Ar+Sc collisions at 75$A$ GeV/$c$. Cuts are not dependent on rapidity.

| rapidity bin | | $(-1.5,-1)$ | $(-1,-0.5)$ | $(-0.5,0)$ | $(0,0.5)$ | $(0.5,1)$ | $(1,1.5)$ | $(1.5,2)$ |
|---|---|---|---|---|---|---|---|---|
| cut value for 75$A$ GeV/$c$ | nominal | >0.999 | >0.9995 | >0.9995 | >0.9995 | >0.9995 | >0.9999 | >0.9999 |
| | loose | >0.995 | >0.999 | >0.999 | >0.999 | >0.999 | >0.9995 | >0.9995 |
| | tight | >0.9995 | >0.9999 | >0.9999 | >0.9999 | >0.9999 | >0.99995 | >0.99995 |

**Table 5.5:** Summary of values used as variations of directional angle cut (dirA in Fig. 5.14) in rapidity bins in order to estimate systematic uncertainty in analysis of Ar+Sc collisions at 75$A$ GeV/$c$.

| rapidity bin | | $(-1.5,-1)$ | $(-1,-0.5)$ | $(-0.5,0)$ | $(0,0.5)$ | $(0.5,1)$ | $(1,1.5)$ | $(1.5,2)$ |
|---|---|---|---|---|---|---|---|---|
| cut value for 75$A$ GeV/$c$ | nominal | >5cm | >5cm | >7.5cm | >12.5cm | >12.5cm | >15cm | >12.5cm |
| | loose | >7.5cm | >7.5cm | >10cm | >15cm | >15cm | >17.5cm | >15cm |
| | tight | >2.5cm | >2.5cm | >5cm | >10cm | >10cm | >12.5cm | >10cm |

**Table 5.6:** Summary of values used as variations of cut on distance between primary and decay vertex (deltaL in Fig. 5.14) in rapidity bins in order to estimate systematic uncertainty in analysis of Ar+Sc collisions at 75$A$ GeV/$c$.

Additionally, one more contribution to the systematic uncertainty of the final multiplicity of $K^0_S$ mesons was taken into account, namely the multiplicity was calculated in a different way. For

the nominal result, the multiplicity was calculated as the integral of fitted rapidity distribution (see Sec. 6.4). In the modified version the multiplicity was calculated as a sum of all measured points from the rapidity distribution multiplied by the rapidity bin width, summed up with the integrals of the linear fits to the most external points of the distribution (two most external points from the left side of the rapidity distribution and two most external points from the right side of the distribution). The fitted lines are presented in Fig. 5.13. The integrals of linear functions were calculated outside of the range covered by experimental points. The difference between the multiplicity of $K^0_S$ mesons calculated in nominal and modified way was taken into account as a contribution to the systematic uncertainty. The different contributions to the final systematic uncertainty of the mean multiplicity of $K^0_S$ are shown in Fig. 5.14.

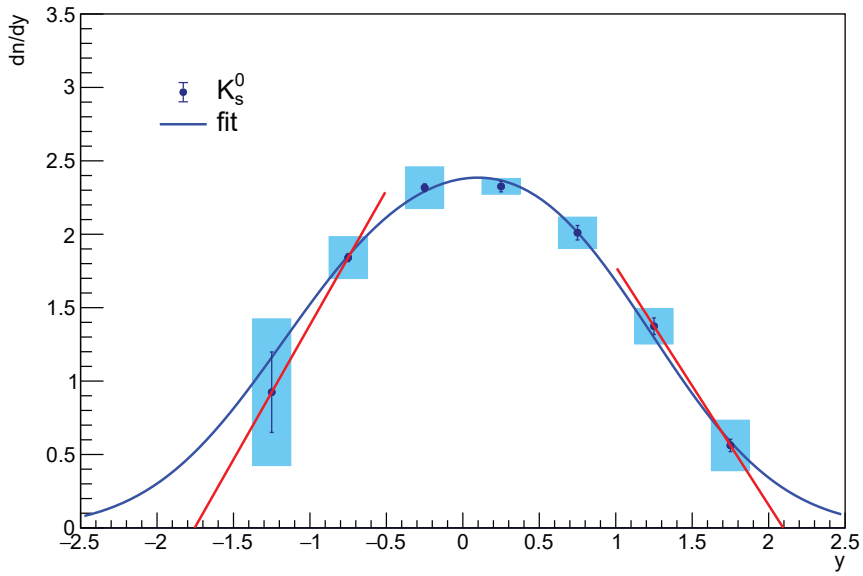


**Figure 5.13:** Rapidity spectrum of $K^0_S$ in 10% most central Ar+Sc collisions at 75$A$ GeV/$c$ (see Sec. 6.4). Red lines fitted to most external points of distribution were used to estimate contribution to systematic uncertainty coming from extrapolation of measured rapidity distribution to full phase space.

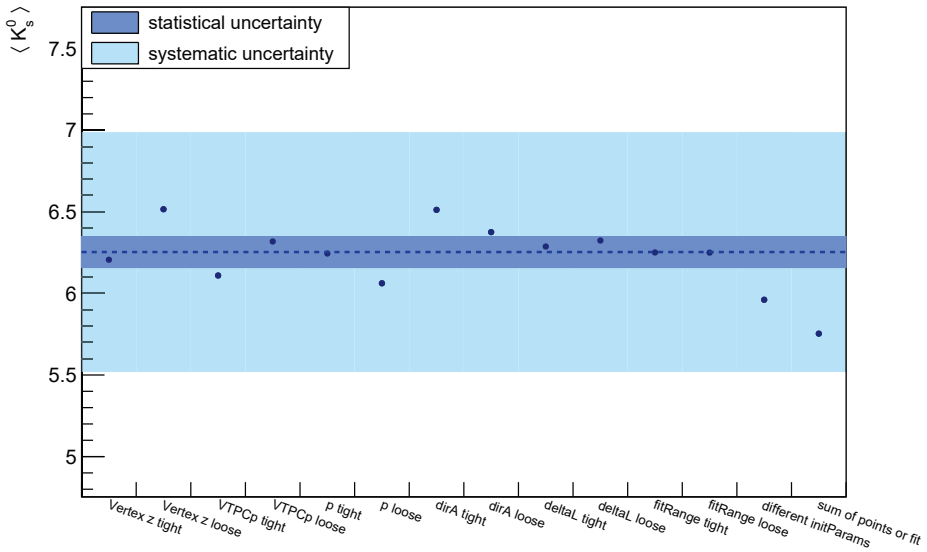


**Figure 5.14:** Contributions of different biasing selection criteria to final systematic uncertainty of mean multiplicity of $K^0_S$ mesons produced in Ar+Sc collisions at $75A$ GeV/$c$. Dashed line denotes $\langle K^0_S \rangle = 6.25$ (see Sec. 6.4).

Chapter 6

# Results

This chapter presents the main experimental results from the analysis of $K^0_S$ meson production in Ar+Sc collisions at 40$A$ GeV/$c$ and 75$A$ GeV/$c$ ($\sqrt{s_{NN}} = 8.77$ GeV and $\sqrt{s_{NN}} = 11.94$ GeV). At first, the mean lifetime measurements of $K^0_S$ mesons are discussed in Sec. 6.1. Then, Sec. 6.2 presents the double-differential spectra in rapidity – transverse momentum space. The one-dimensional transverse momentum and rapidity spectra are shown in Secs. 6.3 and 6.4, concluded with the calculations of the mean multiplicities of produced $K^0_S$ mesons. Finally, the results are compared with other experiments as well as model predictions in Secs. 6.5 and 6.6.

## 6.1 Mean lifetime measurements

One of the quality checks of the $K^0_S$ measurement is the analysis of the lifetime distribution of reconstructed $K^0_S$. It proves the reliability of the reconstruction procedure and application of corrections.

The analysis procedure of lifetime is analogous to the analysis in rapidity and transverse momentum space described in details in Chapter 5. In case of this analysis, the phase space is divided into bins in rapidity and lifetime. The selection of rapidity bins was the same as described in Sec. 5.1. The speed of light times lifetime ($c\tau$) space, normalised to its PDG value ($c\tau_{PDG}$), was divided into 8 bins in the range: $1 < c\tau/c\tau_{PDG} < 5$. All $K^0_S$ candidates accepted after all event and track cuts were taken into account in the lifetime analysis. For a given $K^0_S$ candidate, the lifetime ($c\tau$) was calculated using the distance ($\Delta L$) between the decay vertex and the primary vertex ($c\tau = \Delta L/(\gamma\beta)$, where $\gamma$, $\beta$ are the Lorentz variables) and then divided by the tabulated PDG [3] value $c\tau_{PDG} = 2.6844$ cm. For a given lifetime ($c\tau/c\tau_{PDG}$) and rapidity bin, the invariant mass spectrum was created for all accepted V0 candidates. Then, it was fitted as discussed in Sec. 5.4 in order to extract the raw number of $K^0_S$ in a given bin. A given bin was accepted in the analysis if the statistics of reconstructed $K^0_S$ candidates was high enough to perform the fit. Finally, the raw spectra were corrected in the analogous way (using MC data) as described in Sec. 5.6.

The corrected lifetime ($c\tau/c\tau_{PDG}$) distributions obtained in all rapidity bins for Ar+Sc collisions at 40$A$ GeV/$c$ and 75$A$ GeV/$c$ are presented in Figs. 6.1 and 6.2, respectively. The distributions are fitted with exponential functions in order to calculate the mean lifetime in each rapidity bin. The ratio of calculated mean lifetime value and PDG value as a function of rapidity

is presented in Fig. 6.3 for 40$A$ GeV/$c$ and Fig. 6.4 for 75$A$ GeV/$c$. The obtained results show a very good agreement with the PDG values within the uncertainties.

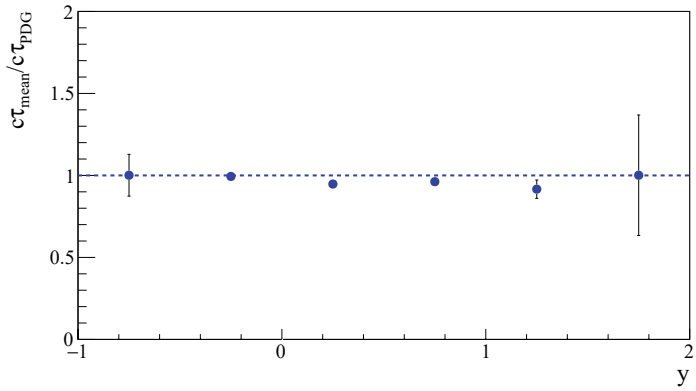


**Figure 6.3:** Mean lifetime with statistical (vertical bars) uncertainties of $K^0_S$ mesons compared with PDG value as function of rapidity for Ar+Sc collisions at 40$A$ GeV/$c$.

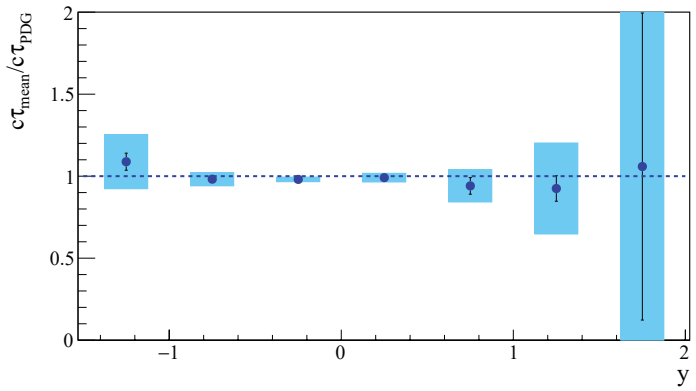


**Figure 6.4:** Mean lifetime with statistical (vertical bars) and systematic (shaded boxes) uncertainties of $K^0_S$ mesons compared with PDG value as function of rapidity for Ar+Sc collisions at 75$A$ GeV/$c$.

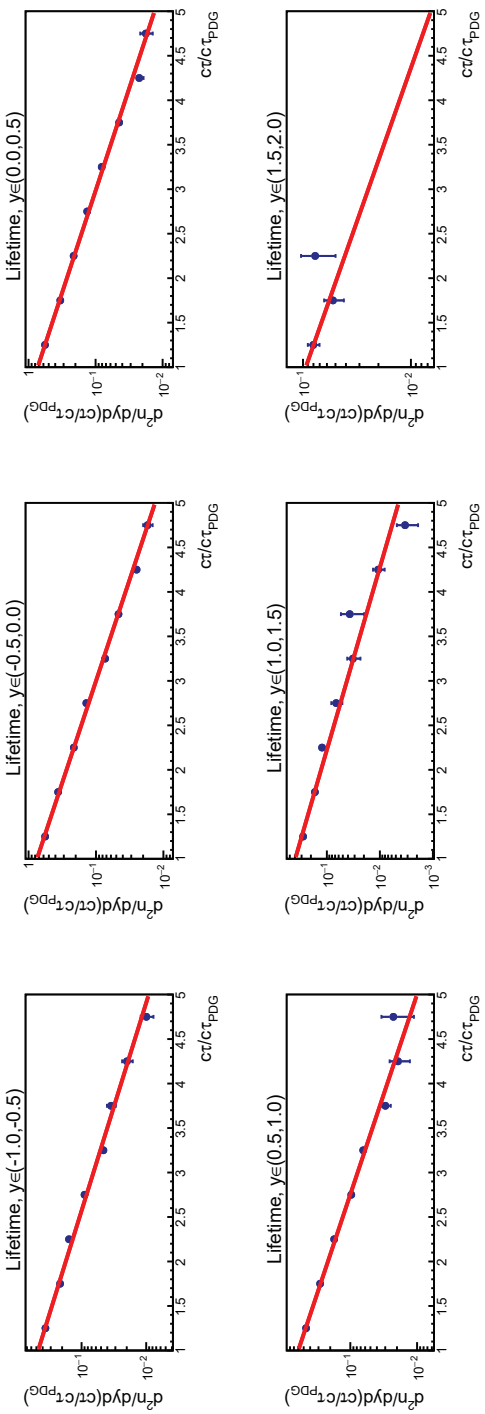


**Figure 6.1:** Corrected lifetime distributions of $K^0_S$ mesons produced in Ar+Sc collisions at 40$A$ GeV/$c$ with statistical uncertainties. Exponential fits of distributions performed in order to estimate mean lifetimes are plotted as red lines.

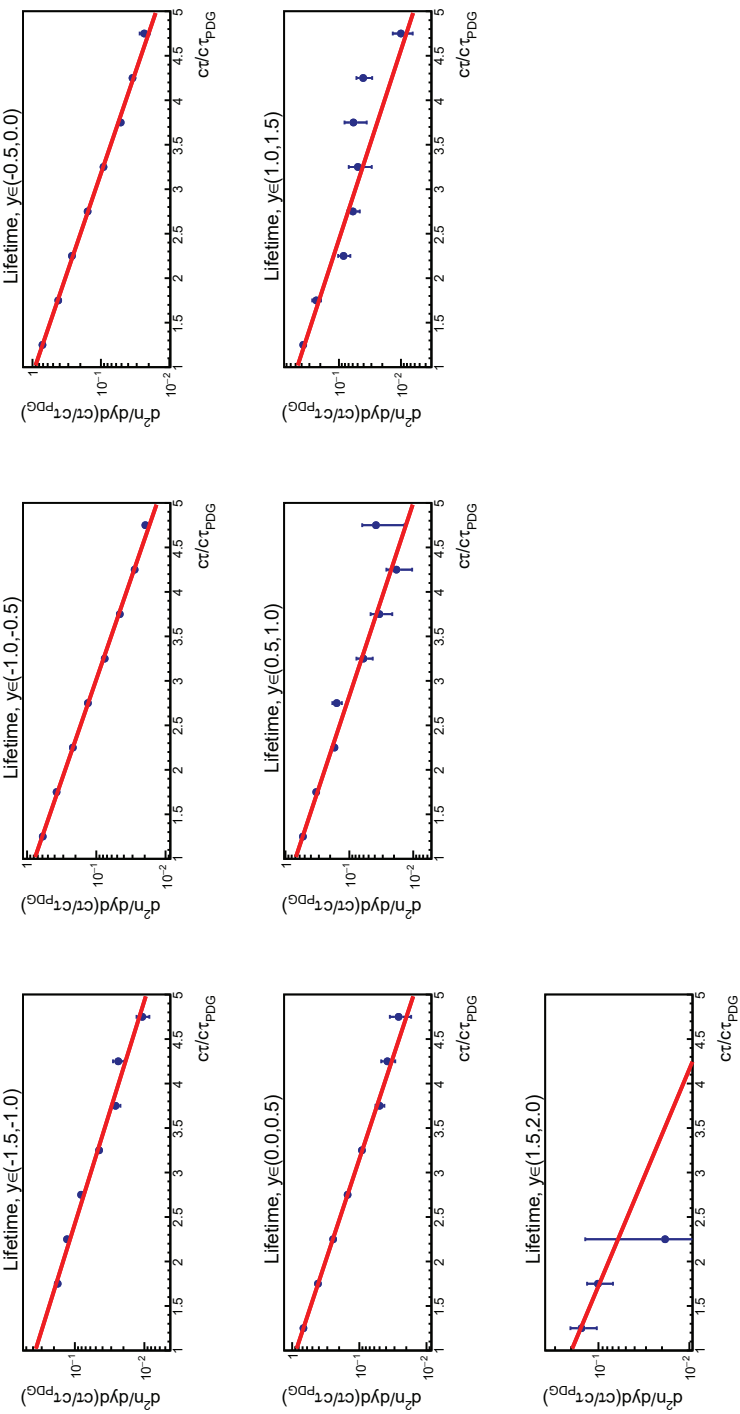


**Figure 6.2:** Corrected lifetime distributions of $K^0_S$ mesons produced in Ar+Sc collisions at 75$A$ GeV/$c$ with statistical uncertainties. Exponential fits of distributions performed in order to estimate mean lifetimes are plotted as red lines.

## 6.2 Double-differential spectra

The double-differential spectra in rapidity and transverse momentum space were calculated as described in Sec. 5.4 and then corrected for detection and reconstruction inefficiencies as described in Sec. 5.6. The final corrected spectra in rapidity – transverse momentum space (given by Eq. (5.10)) with statistical uncertainties (given by Eq. (5.15)) are presented in Fig. 6.5 for Ar+Sc collisions at 40$A$ GeV/$c$ and in Fig. 6.6 for Ar+Sc collisions at 75$A$ GeV/$c$. Additionally, for 75$A$ GeV/$c$ the $y$–$p_T$ spectrum is plotted with systematic uncertainties (calculated as described in Sec. 5.7.2) in Fig. 6.7.

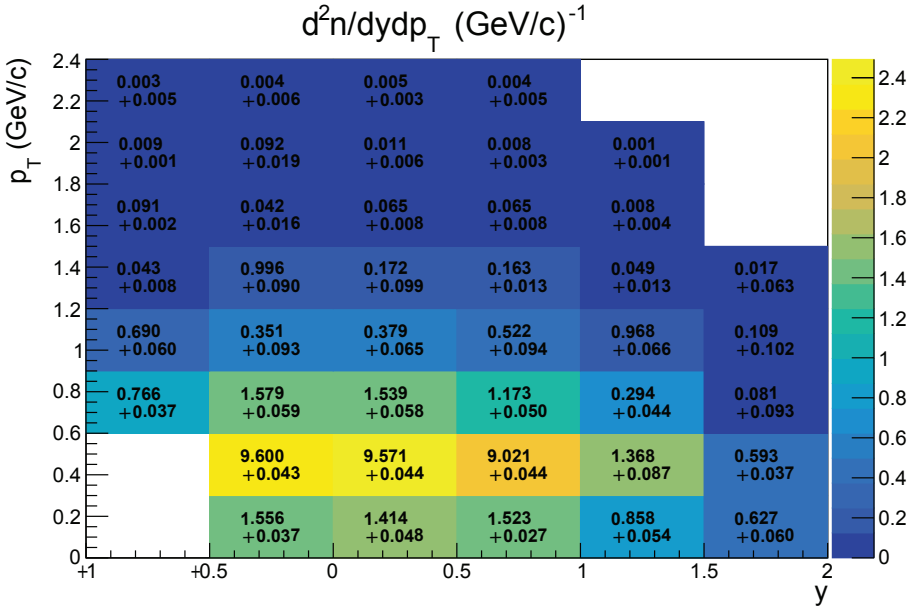


**Figure 6.5:** Double-differential $y$–$p_T$ spectrum of $K^0_S$ mesons produced in Ar+Sc collisions at 40$A$ GeV/$c$ with statistical uncertainties.

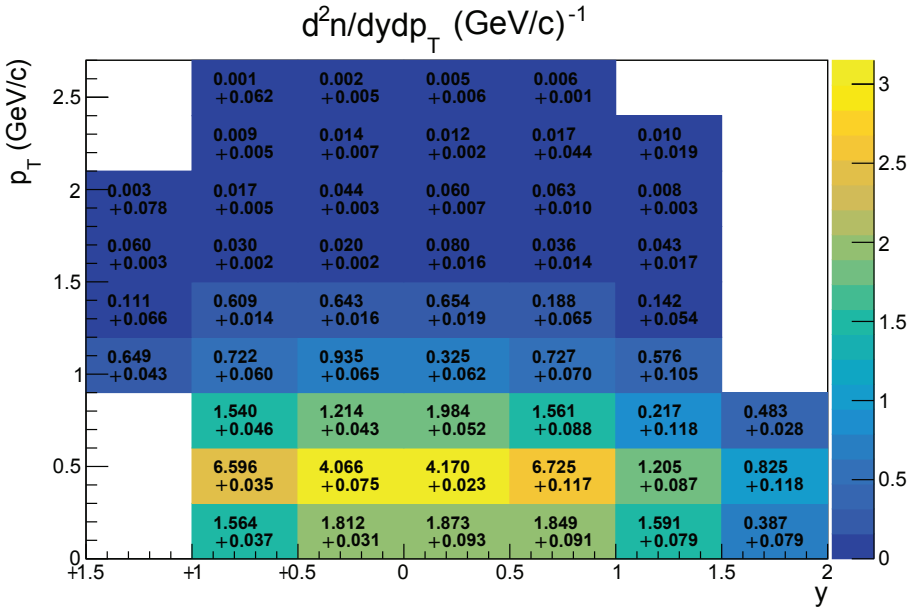


**Figure 6.6:** Double-differential $y$–$p_T$ spectrum of $K^0_S$ mesons produced in Ar+Sc collisions at 75$A$ GeV/$c$ with statistical uncertainties.

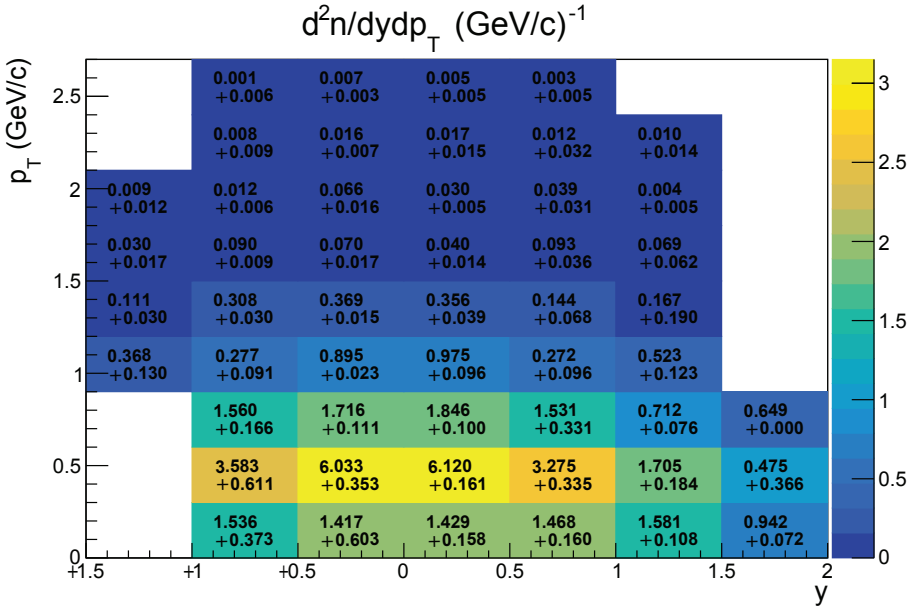


**Figure 6.7:** Double-differential $y$–$p_T$ spectrum of $K^0_S$ mesons produced in Ar+Sc collisions at 75$A$ GeV/$c$ with systematic uncertainties.

## 6.3 Transverse momentum spectra

The $K^0_S$ transverse momentum spectra in rapidity bins are presented in Fig. 6.8 for Ar+Sc collisions at 40$A$ GeV/$c$ and in Fig. 6.9 for Ar+Sc collisions at 75$A$ GeV/$c$. The spectra were fitted with the following function:

$$f(p_T) = A \cdot p_T \cdot \exp\left(\frac{-\sqrt{p_T^2 + m_0^2}}{T}\right), \tag{6.1}$$

where $A$ is the normalisation factor, $T$ is the inverse slope parameter, and $m_0$ is the $K^0_S$ mass taken from Ref. [3]. The fitted functions are plotted as red lines in Figs. 6.8 and 6.9. The inverse slope parameters obtained from the fits are cited in the figure legends.

## 6.4 Rapidity distribution and mean multiplicity

The rapidity spectra of $K^0_S$ mesons produced in Ar+Sc collisions at 40$A$ GeV/$c$ and 75$A$ GeV/$c$ are presented in Fig. 6.10 and Fig. 6.11, respectively. The distributions were obtained from the extrapolated and integrated transverse momentum spectra plotted in Sec. 6.3. The integrals were calculated in range $p_T \in (0, 10)$ GeV/$c$. The statistical uncertainties were taken as the uncertainties of the integrals of fitted functions provided by the ROOT framework [93]. The systematic uncertainties were calculated for Ar+Sc collisions at 75$A$ GeV/$c$ as described in Sec. 5.7.2. Both rapidity distributions were fitted with a sum of two Gaussian functions centered symmetrically around $y = 0$:

$$f(y) = A_1 \cdot \exp\left(-\frac{1}{2}\frac{(y-\mu)^2}{\sigma^2}\right) + A_2 \cdot \exp\left(-\frac{1}{2}\frac{(y+\mu)^2}{\sigma^2}\right), \tag{6.2}$$

where $A_1$ and $A_2$ are the normalisation factors, $\mu$ is the center of a single Gaussian peak (displacement of each peak from $y = 0$), and $\sigma$ is a standard deviation of a single Gaussian peak. The fitting procedure took into account only the statistical uncertainties of the points. The fitted functions are plotted as blue lines in Figs. 6.10 and 6.11.

The mean multiplicity of produced $K^0_S$ mesons was calculated as the integral of the fitted rapidity function (Eq. (6.2)) in the range $y \in (-10, 10)$. The statistical uncertainty was taken as the uncertainty of the integral of fitted function provided by the ROOT framework [93]. The systematic uncertainty of mean multiplicity of $K^0_S$ mesons produced in Ar+Sc collisions at 75$A$ GeV/$c$ was calculated as described in Sec. 5.7.2. The mean multiplicity of $K^0_S$ in the 10% most central Ar+Sc collisions at 40$A$ GeV/$c$ equals: $\langle K^0_S \rangle = 4.495 \pm 0.079(\text{stat})$, and for the 10% most central Ar+Sc collisions at 75$A$ GeV/$c$ equals: $\langle K^0_S \rangle = 6.25 \pm 0.09(\text{stat}) \pm 0.73(\text{sys})$.

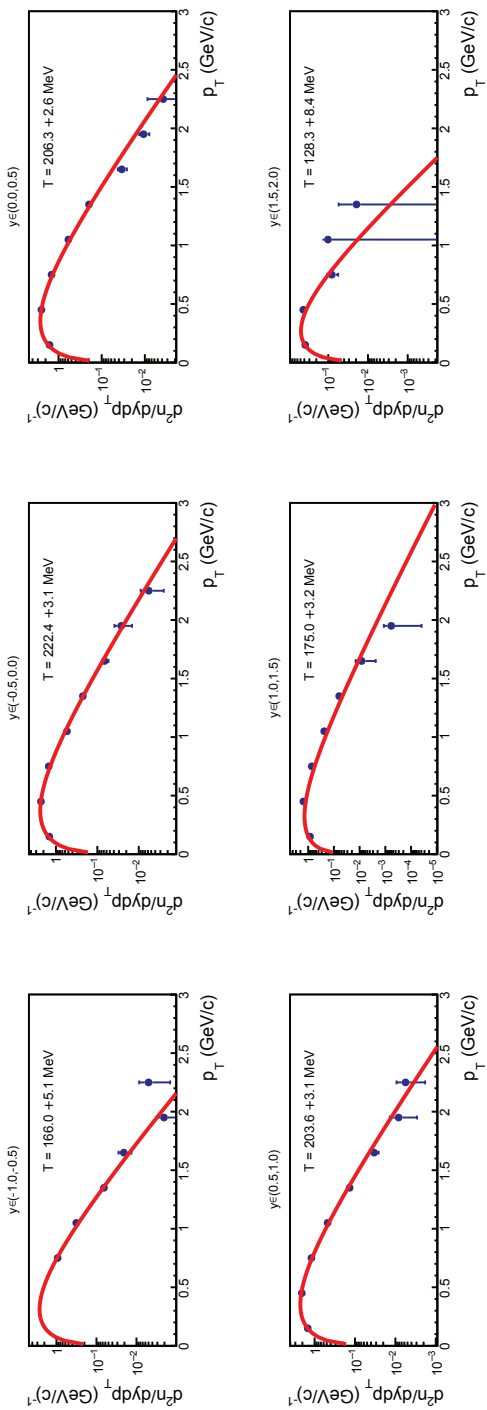


**Figure 6.8:** $K^0_S$ transverse momentum spectra in rapidity bins for Ar+Sc collisions at 40$A$ GeV/$c$ with statistical uncertainties. Red lines are fits given by Eq. (6.1).

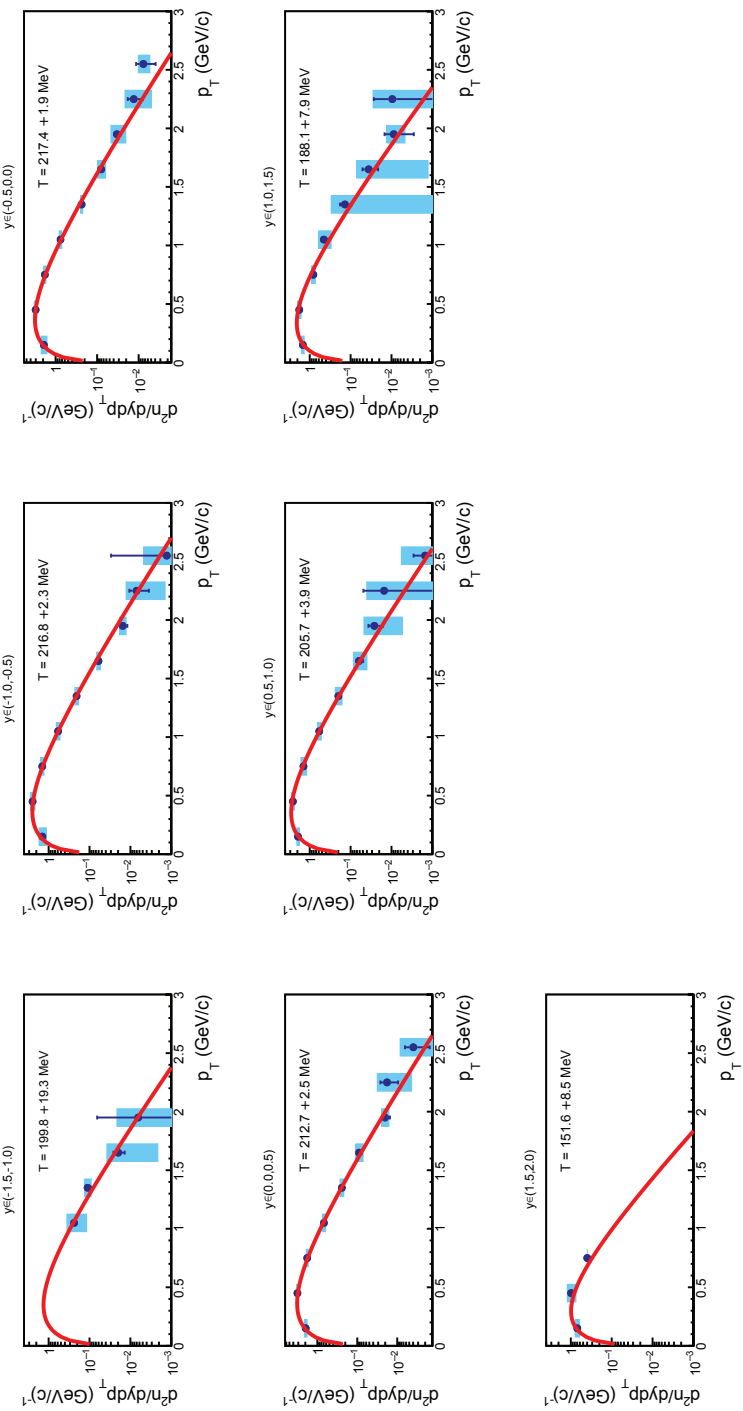


**Figure 6.9:** $K^0_S$ transverse momentum spectra in rapidity bins for Ar+Sc collisions at 75$A$ GeV/$c$ with statistical (vertical bars) and systematic (shaded boxes) uncertainties. Red lines are fits given by Eq. (6.1).

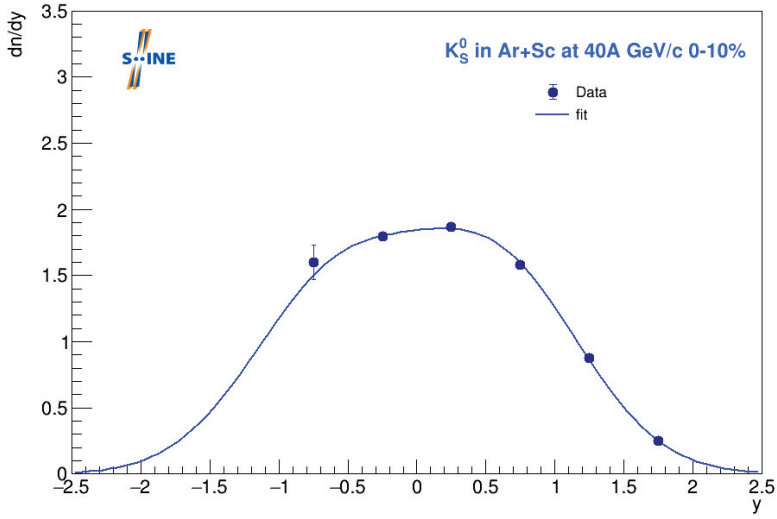


**Figure 6.10:** Rapidity spectrum of $K^0_S$ mesons in 10% most central Ar+Sc collisions at 40$A$ GeV/$c$ with statistical uncertainties plotted as vertical bars. Blue line is fit given by Eq. (6.2).

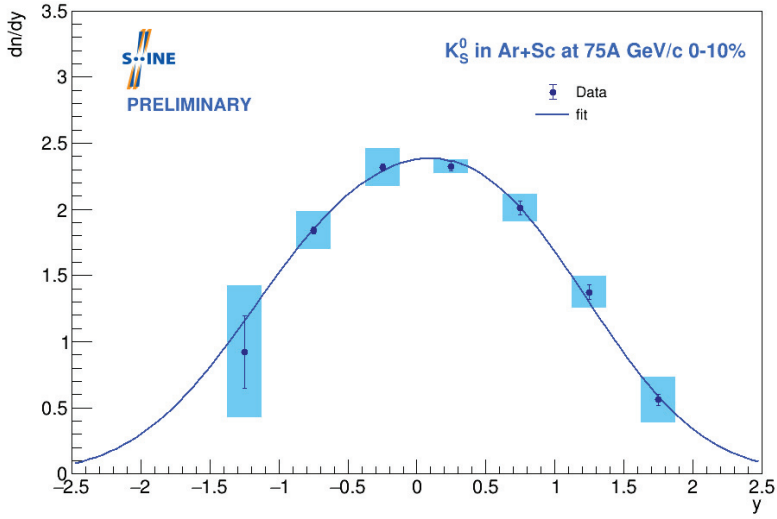


**Figure 6.11:** Rapidity spectrum of $K^0_S$ mesons in 10% most central Ar+Sc collisions at 75$A$ GeV/$c$ with statistical uncertainties plotted as vertical bars and systematic uncertainties as shaded boxes. Blue line is fit given by Eq. (6.2).

## 6.5 Comparison with model predictions

This section presents the comparison of the obtained results with selected models. The results are compared to EPOS 1.99 [38, 86, 94], and SMASH 2.0 [95, 96]. The EPOS stands for Energy conserving quantum mechanical multiple scattering approach, based on Partons (parton ladders), Off-shell remnants and Splitting of parton ladders. It is a microscopic string model in which the colour exchange between partons (quarks and gluons) results in the creation of Pomerons (parton ladders) followed by hadronisation. The SMASH stands for Simulating Many Accelerated Strongly-interacting Hadrons. It uses a relativistic hadronic transport approach including all well-established hadrons.

The comparison of rapidity spectrum of $K^0_S$ in Ar+Sc collisions at 40$A$ GeV/$c$ is presented in Fig. 6.12. The SMASH model underestimates the $K^0_S$ production in the whole rapidity range. The EPOS model overestimates the results in the mid-rapidity region. The forward rapidity region shows good agreement between data and EPOS predictions. Figure 6.13 presents the comparison of the results for Ar+Sc collisions at 75$A$ GeV/$c$. Similarly to 40$A$ GeV/$c$, the SMASH model significantly underestimates $K^0_S$ production. The results for 75$A$ GeV/$c$ are well described by the EPOS predictions.

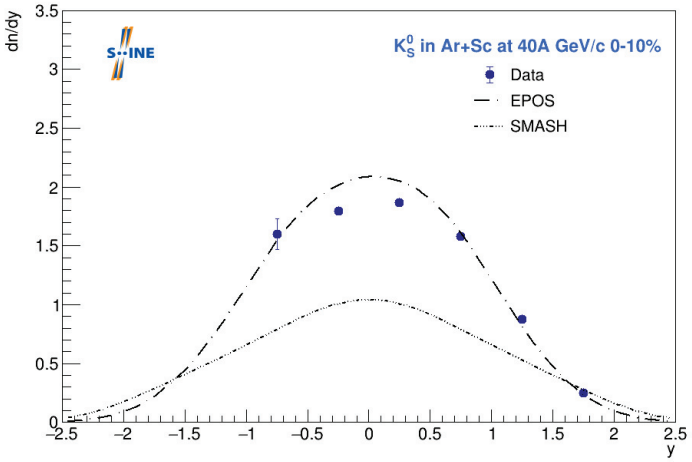


**Figure 6.12:** Comparison of rapidity spectrum of $K^0_S$ mesons in 10% most central Ar+Sc collisions at 40$A$ GeV/$c$ with model predictions. Statistical uncertainties are plotted as vertical bars.

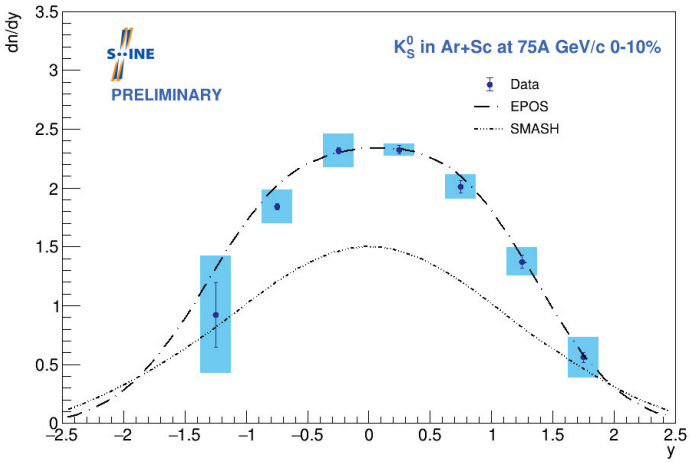


**Figure 6.13:** Comparison of rapidity spectrum of $K^0_S$ mesons in 10% most central Ar+Sc collisions at 75$A$ GeV/$c$ with model predictions. Statistical uncertainties are plotted as vertical bars and systematic uncertainties as shaded boxes.

## 6.6 Comparison with charged kaons

The production of $K^0_S$ mesons should be equal to the mean production of charged kaons (see Sec. 1.4). The results obtained in this thesis were compared with the results on $K^+$ and $K^-$ production in the 10% most central Ar+Sc collisions at 40$A$ GeV/$c$ and 75$A$ GeV/$c$, measured by the NA61/SHINE experiment [97]. For the charged kaons, the following notation is used:

$$K^{+/-} = \frac{K^+ + K^-}{2}, \tag{6.3}$$

where K are the multiplicities of corresponding kaons in selected rapidity and transverse momentum region or in full phase space (mean multiplicity), depending on the figure.

The comparison of rapidity distribution of $K^0_S$ and the average distribution of charged kaons in Ar+Sc collisions at 75$A$ GeV/$c$ is presented in Fig. 6.14. The comparison reveals around 20-25% discrepancy in the mid-rapidity and forward rapidity regions.

The comparison was also studied in transverse momentum space. The top panel of Fig. 6.15 shows the transverse momentum spectra integrated over rapidity in the following range: $y \in (0, 2)$. The spectra are plotted for $K^0_S$ mesons and $K^{+/-}$ in Ar+Sc collisions at 75$A$ GeV/$c$. The spectra were fitted using the function described in Sec. 6.3. For the quantitative comparison the following ratio was defined:

$$R_k = \frac{K^{+/-} - K^0_S}{K^0_S}\ (\%). \tag{6.4}$$

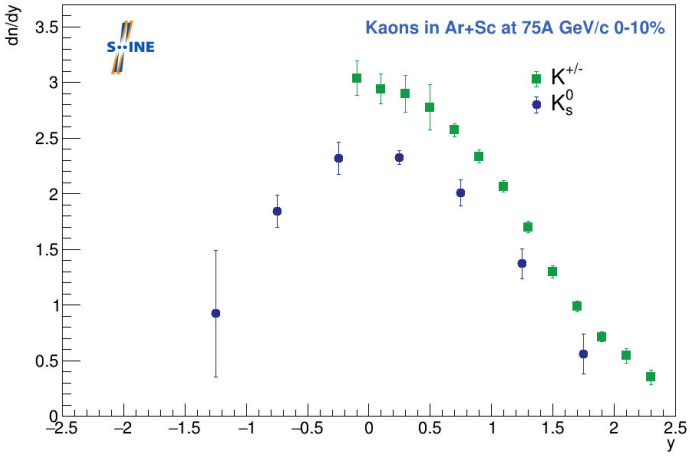


**Figure 6.14:** Comparison of rapidity spectrum of $K^0_S$ (this analysis) and average spectrum of charged kaons [97] in Ar+Sc collisions at 75$A$ GeV/$c$. Total uncertainties are plotted, calculated as square root of sum of squared statistical and systematic uncertainties ($\sqrt{\text{stat}^2 + \text{sys}^2}$). For charged kaons total uncertainties were calculated separately for positively charged and negatively charged kaons, and then propagated.

The bottom panel of Fig. 6.15 presents the $R_k$ ratio calculated for the fitted functions. The difference of around 15-30% can be observed in the wide range of transverse momentum.

The $R_k$ ratio was also calculated for the $dn/dy$ at mid-rapidity. For 40$A$ GeV/$c$ Ar+Sc collisions the result is the following: $R_k = (30.7 \pm 2.7)\%$ (statistical uncertainty only – for charged kaons also only statistical uncertainties were taken into account). For 75$A$ GeV/$c$ Ar+Sc interactions the calculated ratio is equal to: $R_k = (21.6 \pm 6.0)\%$ (total uncertainty calculated in the following way: at first, for each type of kaon total uncertainty is calculated as square root of sum of squared statistical and systematic uncertainties ($\sqrt{\text{stat}^2 + \text{sys}^2}$), and then such uncertainties are propagated). The obtained NA61/SHINE $R_k$ ratios were compared with the world available data. The comparison (computing $R_k$ values) was prepared as a part of this thesis and is presented in Fig. 6.16. It used the $K^0_S$, $K^+$, and $K^-$ experimental data from AGS [56], CERES [55], STAR BES [49, 32], STAR [50, 51, 52, 98], ALICE [54, 99], NA49 [53], HADES [47, 100, 101, 48], and FOPI [102, 46].

The charged to neutral kaon ratios were compared with model predictions. The comparison with HRG [103] and UrQMD [103, 104, 105, 106] is presented in Fig. 6.17. All the experimental points except ALICE follow similar trend, beeing around 15-20% above model predictions. In the model predictions, the charged to neutral kaon ratio is not equal to unity. This is caused by the known effects that violate the isospin symmetry. For example, the small differences between the

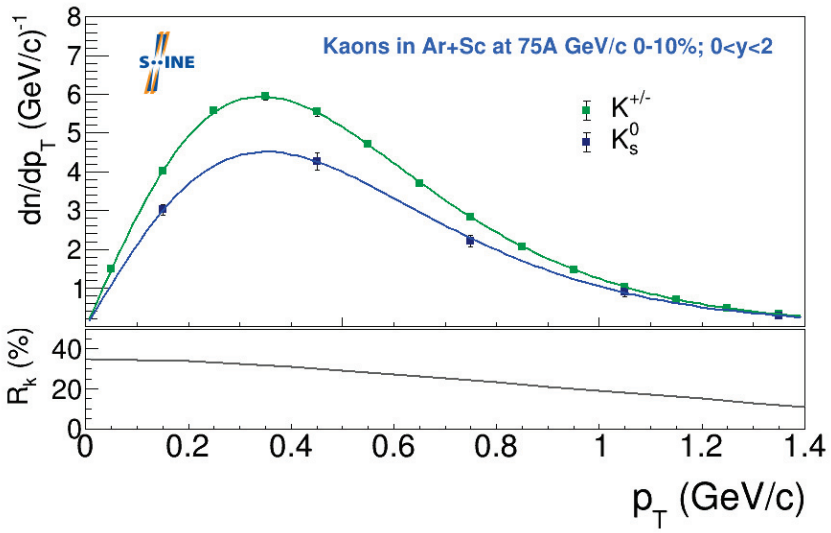


**Figure 6.15:** *Top*: Comparison of transverse momentum spectrum of $K^0_S$ (this analysis) and average spectrum of charged kaons [97] in Ar+Sc collisions at 75$A$ GeV/$c$. Total uncertainties are plotted, calculated as square root of sum of squared statistical and systematic uncertainties ($\sqrt{\text{stat}^2 + \text{sys}^2}$). For charged kaons total uncertainties were calculated separately for positively charged and negatively charged kaons and then propagated. *Bottom*: Transverse momentum dependence of $R_k$ ratio calculated from Eq. (6.4) for fitted functions.

masses of charged and neutral kaons can lead to not negligible modifications. A typical example is the decay of the $\phi(1020)$ meson into kaons, for which branching ratio of $\phi(1020) \rightarrow K^+ + K^-$ is slightly larger than $\phi(1020) \rightarrow K^0_S + K^0_L$. Moreover, for the low energies the model predictions are below unity due to initial isospin assymetry of the colliding system. This effect becomes negligible for central collisions at high energies due to the large size of the created system. The predictions of HRG take into account all the known effects that violate isospin symmetry, however the predicted violation is significantly smaller than the one reflected in experimental data. In order to estimate the scale and accuracy of unknown effects that violate isospin symmetry, in Ref. [103] the experimental points were divided by the predictions of HRG (black dots in Fig. 6.17) (HRG predictions were taken as a baseline). Then, the global fit was performed. The result of this fit is shown in Fig. 6.18. From the fit, the ratio of charged to neutral kaons is equal to $1.140 \pm 0.026$, which means over $5\sigma$ effect of large isospin violation above the known effects.

The presented results reveal large anomalous isospin symmetry breaking effect. This effect remains challenging for existing theoretical models, and its origin calls for further scrutiny. Currently, two theoretical publications on this effect as well as NA61/SHINE experimental publication are under preparation.

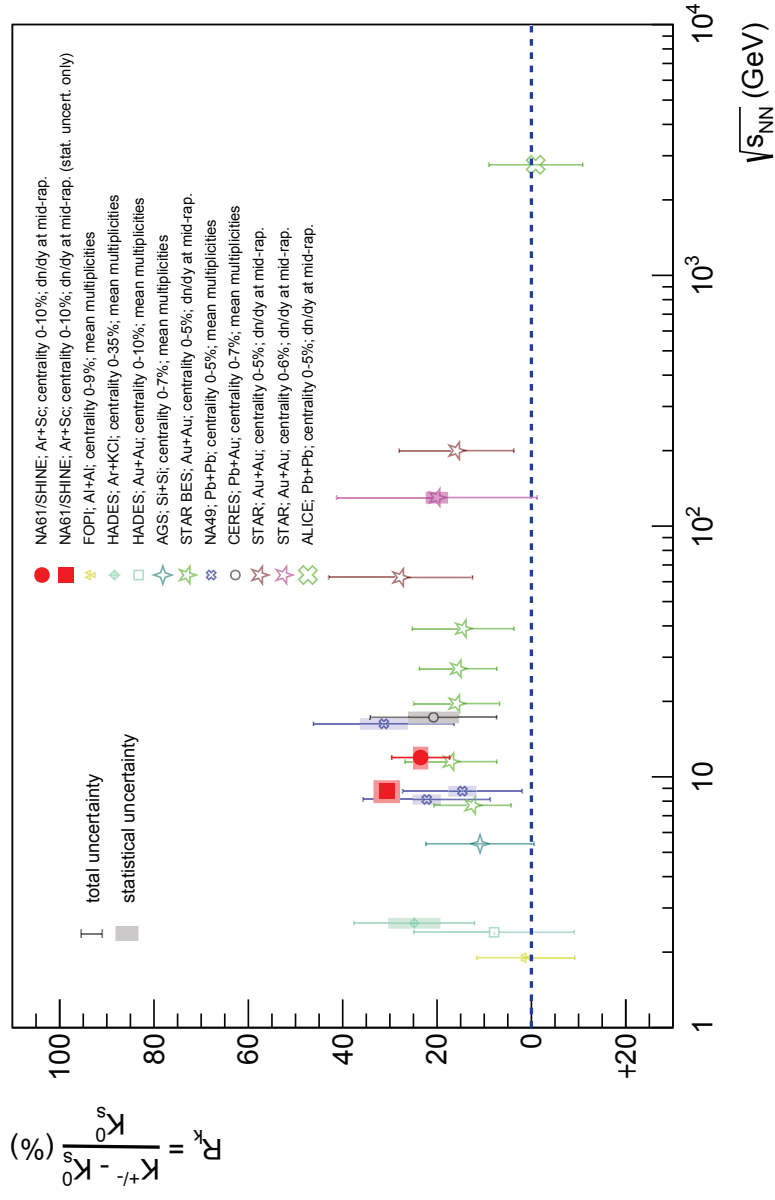


**Figure 6.16:** Compilation of world available data on $R_k$ ratio as function of collision energy.

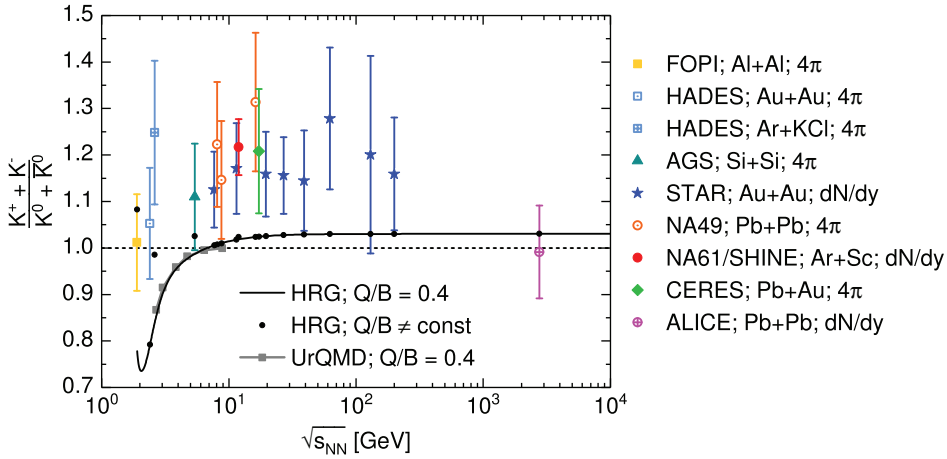


**Figure 6.17:** Charged to neutral kaon ratio ($K^0 + \overline{K^0}$ taken as $2K^0_S$) as function of collision energy. Experimental data are shown by symbols with uncertainties. HRG baseline for electric-to-baryon charge $Q/B = 0.4$ is shown by black line. HRG baseline for $Q/B$ values specified accordingly to given types of colliding nuclei is represented by black dots. UrQMD model results are shown by gray squares. Figure from Ref. [103].

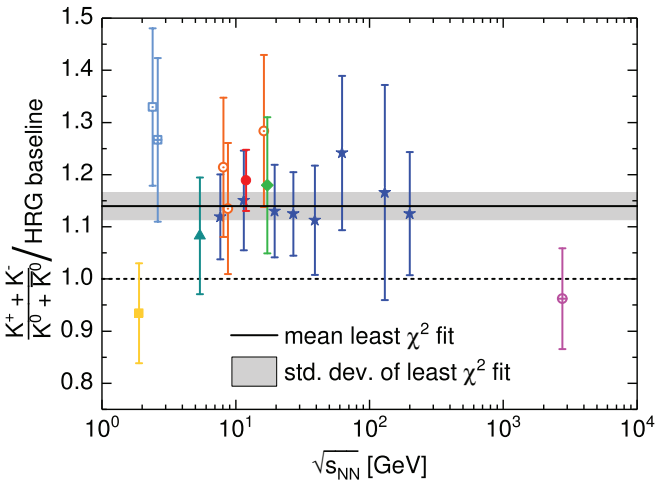


**Figure 6.18:** Experimental data for charged to neutral kaon ratio divided by HRG baseline as function of collision energy. HRG baseline ($Q/B \neq$ const.) is shown by black dots in Fig. 6.17. Figure from Ref. [103].

Chapter 7

# NA61/SHINE upgrade

The NA61/SHINE experiment has undergone a major upgrade during the CERN Long Shutdown 2 (2018–2022) [107]. It was motivated by the measurement of the open charm production in heavy-ion collisions. The setup was commissioned in 2022 and the first physics data taking took place in summer 2022. This chapter presents the motivation of the upgrade and the summary of the work that was done. At the end, the new data acquisition system is discussed in details.

## 7.1 Motivation of the upgrade

The physics programme of the NA61/SHINE was extended by the measurement of the open charm production in heavy-ion collisions. The studies are motivated by three main questions:

1) What is the mechanism of open charm production?
2) How does the onset of deconfinement impact open charm production?
3) How does the formation of quark-gluon plasma impact $J/\psi$ production?

In order to answer these questions the mean number of charm and anti-charm quarks $\langle c\bar{c}\rangle$ produced in the full phase space in heavy-ion collisions is crucial to be known. Up to now, the corresponding measurement has not been performed. The acceptance of the NA61/SHINE spectrometer will allow to extrapolate the measurements to the full phase space with relatively small uncertainties.

The left panel of Fig. 7.1 presents the summary of statistical and dynamical model predictions on the mean multiplicity of the $c\bar{c}$ quarks produced in Pb+Pb collisions at 158$A$ GeV/$c$. The main conclusion from the plot is that the predictions differ by over two orders of magnitude. The future measurement will narrow the spectrum of the model predictions and thus will allow to better understand the mechanism of the open charm production.

The production of the open charm is predicted to be affected by the onset of deconfinement. The predictions of the SMES model are shown in the right panel of Fig. 7.1 for central Pb+Pb collisions. The energy dependence of the $\langle c\bar{c}\rangle$ production is plotted. The blue dashed line corresponds to the scenario without the phase transition. The red line corresponds to the QGP phase. At the beam momentum of 150$A$ GeV/$c$ ($\sqrt{s_{\mathrm{NN}}} \approx 16.8$ GeV) the enhancement of the open charm production by a factor of around 4 is expected in comparison to the scenario without the phase transition.

The last point of the $\langle c\bar{c}\rangle$ production measurement concerns the production of $J/\psi$ meson. The suppression of $J/\psi$ production was one of the key arguments for the discovery of the quark-

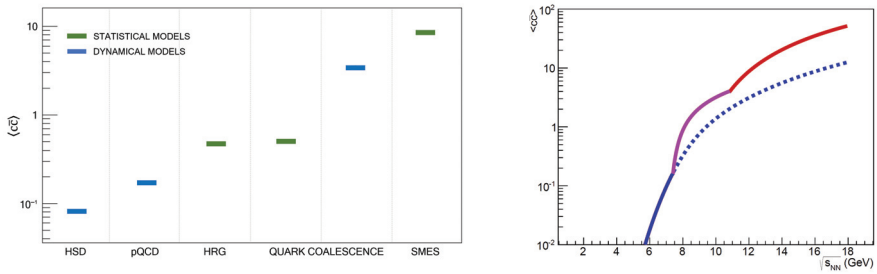


**Figure 7.1:** *Left*: Mean multiplicities of charm quark pairs produced in full phase space in central Pb+Pb collisions at 158*A* GeV/*c* calculated within statistical models (green bars): Hadron Resonance Gas model (HRG) [108], Statistical Quark Coalescence model [108] and Statistical Model of the Early Stage (SMES) [30] as well as dynamical models (blue bars): Hadron String Dynamics (HSD) model [109], pQCD-inspired model [110, 111] and Dynamical Quark Coalescence model [112]. *Right*: Energy dependence of mean multiplicity of charm quark pairs produced in central Pb+Pb collisions according to Statistical Model of the Early Stage [113]. Dotted line represents scenario without phase transition and solid one with phase transition (energy of onset of deconfinement is approximately $\sqrt{s_{NN}} \approx 7$ GeV). Figures from Ref. [107].

gluon plasma [7, 8]. The probability of $J/\psi$ formation is described by the following formula: $P(c\bar{c} \to J/\psi) \equiv \frac{\langle J/\psi \rangle}{\langle c\bar{c} \rangle}$. The mean multiplicity $\langle J/\psi \rangle$ was measured by other experiments, but $\langle c\bar{c} \rangle$ has not been measured yet. Thus, the interpretation of rich measurements on $J/\psi$ production was based on the assumption that the mean multiplicity of $c\bar{c}$ quarks is proportional to the mean multiplicity of Drell-Yan pairs [16, 114]: $\langle c\bar{c} \rangle \sim \langle DY \rangle$. Based on this assumption, the results of the NA50 experiment were interpreted as the evidence of the QGP formation in the central Pb+Pb collisions at 158$A$ GeV/$c$. This result is presented in Fig. 7.2. The future NA61/SHINE measurement of $\langle c\bar{c} \rangle$ will allow to verify the assumption and make a stronger conclusion on the presented result.

## 7.2 Upgrade

The schematic summary of the NA61/SHINE detector upgrade is presented in Fig. 7.3. The most important improvement from the point of view of the open charm measurements was the construction of the new Vertex Detector with the improved acceptance coverage. Moreover, the replacement of the TPC read-out electronics allowed for over tenfold increase of the data-taking rate up to 1 kHz. The radiation tolerance of the PSD was significantly improved by installation of the Forward PSD (PSD2). The old ToF-L and ToF-R detectors were dismounted. Up to now, only the new ToF-L detector was installed which is based on the Multigap Resistive Plate Chambers (MRPCs). The ToF-R wall will be installed in the future. Finally, the new trigger and data acquisition (DAQ) systems were developed.

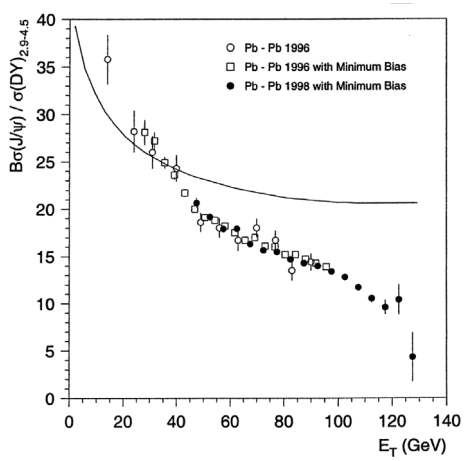


**Figure 7.2:** Branching ratio (B) multiplied $\sigma_{\mathrm{J}/\psi}$ (cross-section – measure of production/reaction probability) and divided by $\sigma_{\mathrm{DY}}$ (cross-section for well-known Drell-Yan process – lepton pair production in electromagnetic interaction of hadrons) as function of transverse energy (measure of collision centrality – most central events have highest values of $E_T$) in Pb+Pb collisions at 158$A$ GeV/$c$ measured by NA50. Curve represents $\mathrm{J}/\psi$ suppression due to ordinary ("cold") nuclear matter absorption. Figure from Ref. [114].

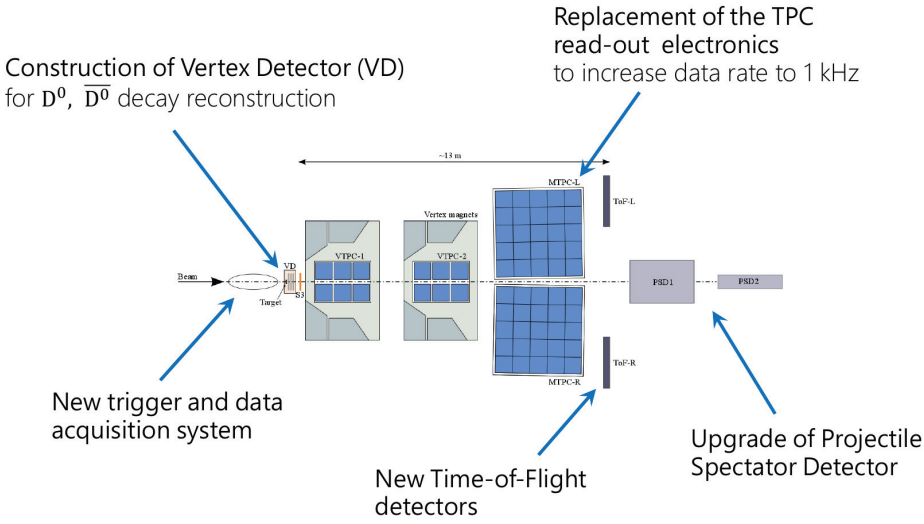


**Figure 7.3:** Schematic picture of most important upgrades in NA61/SHINE experiment. Figure from Ref. [107].

## 7.3 DAQ

The performed NA61/SHINE upgrade required the development of the new data acquisition system. The schematic overview of the new DAQ is presented in Fig. 7.4. The first step in the DAQ is the Detector Layer. It is based on the custom Front-End electronics which is specific to each sub-detector. The data from the detectors is then send to the Read-out Layer consisting of read-out nodes which are able to load the data into the computer memory. On the nodes, the data can be manipulated, for example on each out of 11 TPC nodes, the TPC sub-events are built out of up to eleven channels. Then, the data are sent to one out of 168 Event Builders, which glue together all the sub-events into full detector event. Each sub-event is marked with a unique event ID on the trigger level, thus it is known how to connect all the sub-events together. The full events are sent to the permanent storage with the possibility of semi-online processing, for example noise filtering. Everything is controlled by the Acquisition Supervisor. There is also a separate network for monitoring which includes online Event Monitor and DAQ Monitor. Those are crucial during the data-taking as it is important to detect any problems with the data as soon as possible. The DAQ system is also integrated with the Detector Control System (DCS). The DCS controls and monitors all the healthy parameters of all the sub-detectors. If something is wrong with any of the sub-detectors, DCS can send the request to DAQ to stop the data-taking.

## 7.4 PteroDAQtyl framework

PteroDAQtyl is a software framework that enables the uniform way of running and controlling the DAQ processes. The project is written in C++ programming language [115]. It is designed as a modular system which makes it easy scalable.

In order to easily control all the processes, each process has to obey the rules of the finite state machine presented in Fig. 7.5. Only strictly defined states are allowed for each process and the transition between the states can occur only under the defined conditions. The Acquisition Supervisor monitors the states of all the processes and detects the errors.

### 7.4.1 PteroDAQtyl modules

The single pteroDAQtyl process can load a configurable number and types of modules. A pteroDAQtyl module is a plugin that can be loaded at run-time by the bare pteroDAQtyl executable, which then acquires its functionalities. It is a class that implements the functions like configure()/unconfigure(), start()/stop() and runner(). The function runner() defines the code that is executed in the loop when the module is running. It can be for example reading out the sub-event from the electronics and sending it for further processing. When the pteroDAQtyl process is launched, it creates the instance of the Command Handler and Module Manager. The Command Handler opens the connection on which it can accept the commands from the Acquisition Supervisor. The example commands that can be accepted are configure/unconfigure, start/stop, shutdown.

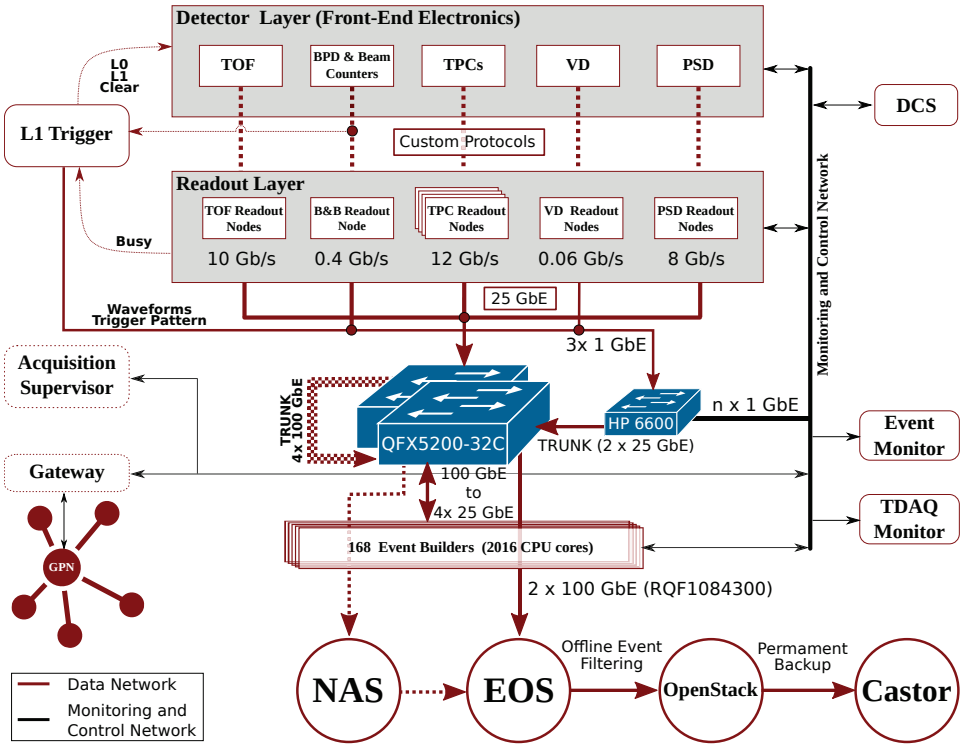


**Figure 7.4:** Schematic layout of new DAQ system of NA61/SHINE experiment. Figure from Ref. [70].

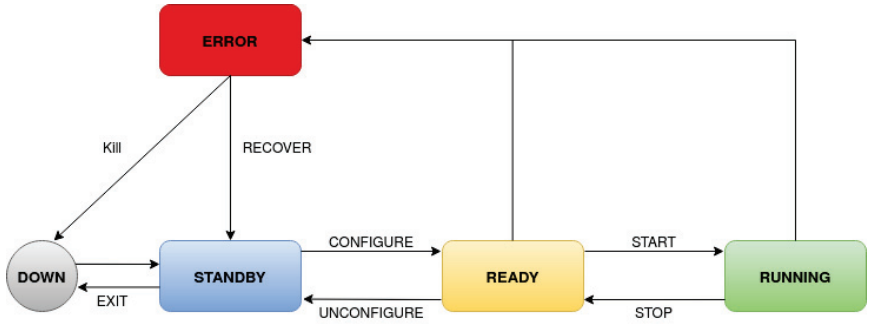


**Figure 7.5:** Schematic picture of finite state machine concept that all pteroDAQtyl processes have to obey.

The Module Manager loads the modules and serves as the interface between the Command Handler and modules. When the Command Handler receives the command, the Module Manager calls the proper function on all the modules. The schematic overview of a single pteroDAQtyl process is presented in Fig. 7.6.

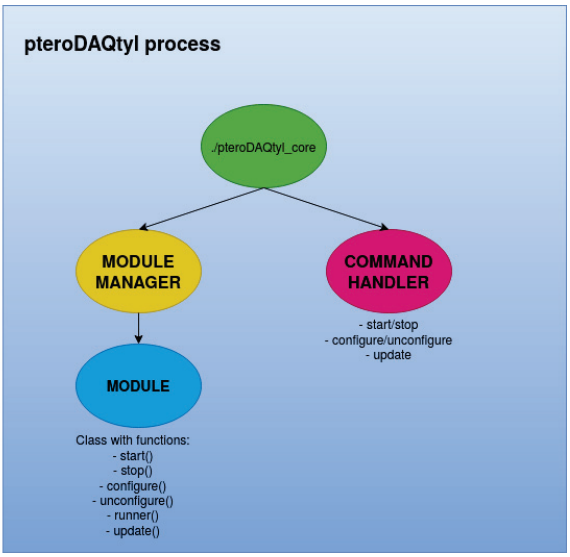


**Figure 7.6:** Schematic picture of single pteroDAQtyl process.

### 7.4.2 Data Manager

The pteroDAQtyl modules can communicate between themselves via the Data Manager. Data Manager is a collection of classes, that allows for sending the data between the modules. The data between the modules running in the same process can be sent by passing the pointer to the event object. For the modules running in different processes and very often on different machines, the ZMQ [116] based solution was prepared. The ZMQ is an open-source universal messaging library. The Data Manager implements two different schemas of sending the sub-events: aggregation mode and pipeline mode. The aggregation mode is presented in the left panel of Fig. 7.7. In this mode many sub-events from different sub-detectors are sent to one receiver. This scenario occurs when gluing together the sub-events into one event. The pipeline mode is presented in the right panel of Fig. 7.7. The events are sent from one module to another. It is needed when the events are processed by different modules, for example for online noise filtering.

The tools provided by the Data Manager are sufficient to implement the full data flow needed by the NA61/SHINE experiment, presented schematically in Fig. 7.8. On the read-out nodes, the detector sub-events are built from the different read-out electronics channels data. Then, the sub-events are sent via ZMQ to the Event Builders.

### 7.4.3 Metric Manager

Each module can register any number of metrics in the Metrics Manager. The value of each metric is published with a configurable time interval. Metric Manager can publish either a current value of a metric or perform some basic operations, for example calculate the rate of the mean value over time. Any monitoring client can connect to the metrics publisher and subscribe

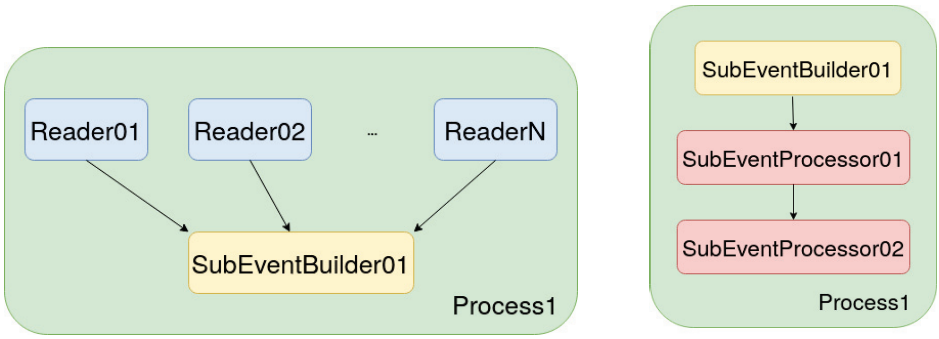


**Figure 7.7:** *Left*: Schematic picture showing aggregation mode of data transfer. *Right*: Schematic picture of pipeline mode.

the data. The default monitoring client included in the pteroDAQtyl, sends the metrics to the influxDB [117] – the time series database. The data can be visualized in Grafana [118]. The example Grafana dashboard is presented in Fig. 7.9. It shows the main dashboard that was displayed in the NA61/SHINE control room during the data-taking.

## 7.5 Impact of the upgrade on future $K^0_S$ studies

The upgraded detection setup of the NA61/SHINE is planned to be used in the future to collect the data on different intermediate-mass systems (He+He, B+B, O+O, Mg+Mg) [119]. The collected statistics on one system is planned to be around 10 times higher than the typical statistics recorded in the past by NA61/SHINE. This will allow for more precise study of isospin symmetry violation in ion collisions.

Motivated by the results presented in this thesis, the selected systems are planned to be fully isospin symmetric (the same number of protons and neutrons). The collected statistics will reduce the statistical uncertainties of both charged and neutral kaon measurements, allowing for more precise studies of isospin symmetry violation effect. The upgraded ToF detectors will improve the identification of charged kaons in the mid-rapidity region. The new TPC read-out electronics provides a lower noise level and a better resolution in $\mathrm{d}E/\mathrm{d}x$ measurement. Additionally, smaller colliding systems will result in smaller track density, improving $\mathrm{d}E/\mathrm{d}x$ measurement as well. All the mentioned points will reduce the systematic uncertainties of the results and will contribute to more precise measurements of observed isospin violation effect.

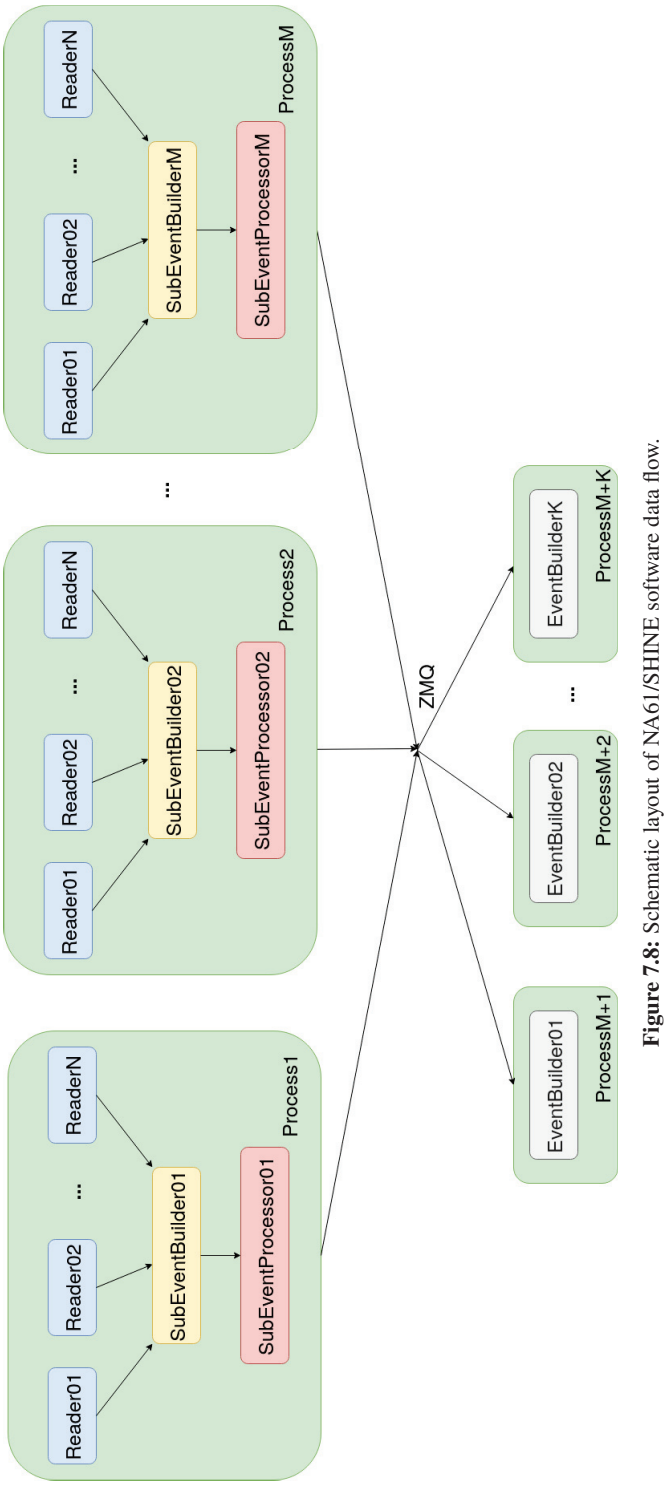


**Figure 7.8:** Schematic layout of NA61/SHINE software data flow.


**Figure 7.9:** Monitoring dashboard used during NA61/SHINE data-taking in 2022.

Chapter 8

# Summary

This thesis presents the analysis of the $K^0_S$ meson production in the 10% most central Ar+Sc collision at the beam momenta of 40$A$ GeV/$c$ and 75$A$ GeV/$c$ (the available energy in the center-of-mass system per nucleon pair: $\sqrt{s_{NN}} = 8.77$ GeV and $\sqrt{s_{NN}} = 11.94$ GeV, respectively). The data were collected by the NA61/SHINE experiment at the CERN SPS.

The main results of this thesis are the double-differential spectra of $K^0_S$ in rapidity – transverse momentum space. The $K^0_S$ mesons were reconstructed by studying their decay products. The decay channel into two charged pions was taken into account. The final results were corrected for losses due to detection and data processing inefficiencies using simulated data.

The results were compared with selected model predictions. The EPOS model describes the data well for Ar+Sc collisions at 75$A$ GeV/$c$ and slightly overestimates the $K^0_S$ production in mid-rapidity region for Ar+Sc collisions at 40$A$ GeV/$c$. The SMASH model significantly underestimates the $K^0_S$ production at both studied energies of the collisions.

The production of $K^0_S$ was compared with the production of charged kaons measured by the NA61/SHINE experiment. The $K^0_S$ production was expected to be equal to the mean production of charged kaons due to isospin symmetry. The presented comparison revealed a significant difference. The ratio of charged to neutral kaons was observed to be around 20% bigger than unity. This phenomenon was interpreted as unexpected, large isospin symmetry violation. The obtained results were compared with available world data. Although the world data points have large uncertainties, all the measurements follow the same trend of around 15-20% difference between charged and neutral kaons. The global fit proves the ratio of charged to neutral kaons to be significantly higher than unity on the level of above 5$\sigma$. The NA61/SHINE publication with the results discussed in this thesis is under preparation.

The NA61/SHINE experiment has undergone a significant upgrade recently. The upgraded setup will allow for a ten-fold increase of the data-taking rate. The data are expected to have a better quality, e.g. better $\mathrm{d}E/\mathrm{d}x$ resolution, precise vertexing, improved particle identification. It will allow for more precise measurements of neutral and charged kaons in ion collisions and further studies of the observed isospin symmetry violation effect.

# Bibliography


[1] S. Weinberg, "*The Making of the standard model*", *Eur. Phys. J.*, vol. C34, pp. 5–13, 2004. arXiv:hep-ph/0401010 [hep-ph].

[2] "Standard Model". `https://en.wikipedia.org/wiki/Standard_Model`, Accessed: 30.03.2023.

[3] R. L. Workman *et al.* [Particle Data Group], "*Review of Particle Physics*", *Prog. Theor. Exp. Phys.*, vol. 2022, p. 083C01, 2022.

[4] T. Gershon [LHCb], "*Exotic hadron naming convention*", arXiv:2206.15233 [hep-ex].

[5] "Lattice QCD, the numerical approach to the strong force". `https://webific.ific.uv.es/web/en/content/lattice-qcd-numerical-approach-strong-force`, Accessed: 23.09.2022.

[6] S. Bilenky, "*Neutrino oscillations: From a historical perspective to the present status*", *Nucl. Phys. B*, vol. 908, pp. 2–13, 2016. arXiv:1602.00170 [hep-ph].

[7] U. W. Heinz and M. Jacob, "*Evidence for a New State of Matter: An Assessment of the Results from the CERN Lead Beam Program*", arXiv:nucl-th/0002042.

[8] M. I. Gorenstein, "*Discovery of quark-gluon plasma in nucleus nucleus collisions at CERN SPS*", in *Crimean Summer School-Seminar on New Trends in High-Energy Physics (Crimean 2000)*, pp. 128–134, 2000.

[9] T. Ludlam, "*Experimental results from the early measurements at RHIC: Hunting for the quark-gluon plasma*", *Nucl. Phys. A*, vol. 750, pp. 9–29, 2005.

[10] H. R. Schmidt and J. Schukraft, "*The physics of ultra-relativistic heavy-ion collisions*", *J. Phys. G*, vol. 19, pp. 1705–1796, 1993.

[11] I.-K. Yoo, "*Bose-Einstein Correlations of Charged Kaons and Pions in Central Pb+Pb Collisions at 158 AGeV*". Ph.D. thesis, Philipps-Universitat Marburg, 2001, `https://edms.cern.ch/document/816026/1`.

[12] J. Rafelski and B. Muller, "*Strangeness Production in the Quark-Gluon Plasma*", *Phys. Rev. Lett.*, vol. 48, p. 1066, 1982.

[13] A. Bazavov *et al.* [HotQCD], "*Chiral crossover in QCD at zero and non-zero chemical potentials*", *Phys. Lett. B*, vol. 795, pp. 15–21, 2019. arXiv:1812.08235 [hep-lat].

[14] S. Borsanyi, Z. Fodor, J. N. Guenther, R. Kara, S. D. Katz, P. Parotto, A. Pasztor, C. Ratti, and K. K. Szabo, "*QCD Crossover at Finite Chemical Potential from Lattice Simulations*", *Phys. Rev. Lett.*, vol. 125, no. 5, p. 052001, 2020. arXiv:2002.02821 [hep-lat].

[15] J. D. Bjorken, "*Energy Loss of Energetic Partons in Quark-Gluon Plasma: Possible Extinction of High $p_T$ Jets in Hadron-Hadron Collisions*". tech. rep., FERMILAB, Batavia, 1982, FERMILAB-PUB-82-59-THY, `https://inspirehep.net/literature/181746`.

[16] T. Matsui and H. Satz, "*$J/\psi$ Suppression by Quark-Gluon Plasma Formation*", *Phys. Lett.*, vol. B178, pp. 416–422, 1986.

[17] U. W. Heinz, "*From SPS to RHIC: Maurice and the CERN heavy-ion programme*", *Phys. Scripta*, vol. 78, p. 028005, 2008. arXiv:0805.4572 [nucl-th].

[18] L. Adamczyk *et al.* [STAR], "*Centrality dependence of identified particle elliptic flow in relativistic heavy ion collisions at $\sqrt{s_{NN}}$=7.7–62.4 GeV*", *Phys. Rev.*, vol. C93, no. 1, p. 014907, 2016. arXiv:1509.08397 [nucl-ex].

[19] "NA49 library of images".

[20] D. H. Perkins, "*Introduction to high energy physics, 4th ed*", *Cambridge University Press*, 2000. https://doi.org/10.1017/CBO9780511809040.

[21] C. G. Wohl, "*Isospin relations by counting*", *Am. J. Phys.*, vol. 50, pp 748–753, 1982.

[22] M. Gazdzicki and O. Hansen, "*Hadron production in nucleon-nucleon collisions at 200 GeV/c – A compilation*", *Nucl. Phys. A*, vol. 528, pp. 754–770, 1991.

[23] A. Wroblewski, "*On the strange quark suppression factor in high-energy collisions*", *Acta Phys. Polon. B*, vol. 16, pp. 379–392, 1985.

[24] T. Anticic *et al.* [NA49], "*Inclusive production of charged kaons in p+p collisions at 158 GeV/c beam momentum and a new evaluation of the energy dependence of kaon production up to collider energies*", *Eur. Phys. J. C*, vol. 68, pp. 1–73, 2010. arXiv:1004.1889 [hep-ex].

[25] I. Smushkevich, *Dokl. Akad. Nauk SSSR*, vol. 103, no. 235, 1955.

[26] G. Pinski, A. J. Macfarlane, and E. C. G. Sudarshan, "*Shmushkevich's method for a charge-independent theory*", *Phys. Rev.*, vol. 140, pp. B1045–B1053, 1965.

[27] "Kaons – basic theory". `https://hep.uchicago.edu//cpv/theory.html`, Accessed: 20.05.2023.

[28] J. Podolanski and R. Armenteros, "*III. Analysis of V-events*", *The London, Edinburgh, and Dublin Philosophical Magazine and Journal of Science*, vol. 45, no. 360, pp. 13–30, 1954.

[29] T. Czopowicz, "*Study of $K^0_S$ meson production in NA61 experiment at the CERN SPS*". M.Sc. thesis, Warsaw University of Technology, 2010, `https://cds.cern.ch/record/2240120`.

[30] M. Gazdzicki and M. I. Gorenstein, "*On the early stage of nucleus-nucleus collisions*", *Acta Phys. Polon. B*, vol. 30, p. 2705, 1999. arXiv:hep-ph/9803462.

[31] C. Alt *et al.* [NA49], "*Pion and kaon production in central Pb + Pb collisions at 20A and 30A GeV: Evidence for the onset of deconfinement*", *Phys. Rev. C*, vol. 77, p. 024903, 2008.

[32] L. Adamczyk *et al.* [STAR], "*Bulk properties of the medium produced in relativistic heavy-ion collisions from the beam energy scan program*", *Phys. Rev. C*, vol. 96, no. 4, p. 044904, 2017. arXiv:1701.07065 [nucl-ex].

[33] J. Cleymans, R. V. Gavai, and E. Suhonen, "*Quarks and gluons at high temperatures and densities*", *Phys. Rept.*, vol. 130, p. 217, 1986.

[34] A. Acharya *et al.* [NA61/SHINE], "*Spectra and mean multiplicities of $\pi^-$ in central $^{40}Ar$+$^{45}Sc$ collisions at 13A, 19A, 30A, 40A, 75A and 150A GeV/c beam momenta measured by the NA61/SHINE spectrometer at the CERN SPS*", *Eur. Phys. J. C*, vol. 81, no. 5, p. 397, 2021. arXiv:2101.08494 [hep-ex].

[35] W. Brylinski [NA61/SHINE], "*Strangeness production in NA61/SHINE*", *WWND 2023 conference,* `https://indico.cern.ch/event/1196342/contributions/5228282/`.

[36] M. Kuich [NA61/SHINE], "*Recent results on the study of the onset of deconfinement and search for critical point from NA61/SHINE experiment*", *WHBM 2023 conference,* `https://conference-indico.kek.jp/event/205/contributions/4115/`.

[37] A. Aduszkiewicz *et al.* [NA61/SHINE], "*Report from the NA61/SHINE experiment at the CERN SPS*", tech. rep., CERN, Geneva, 2017, CERN-SPSC-2017-038, SPSC-SR-221, `https://cds.cern.ch/record/2287091`.

[38] T. Pierog and K. Werner, "*EPOS Model and Ultra High Energy Cosmic Rays*", *Nucl. Phys. B Proc. Suppl.*, vol. 196, pp. 102–105, 2009. arXiv:0905.1198 [hep-ph].

[39] A. Motornenko, V. V. Begun, V. Vovchenko, M. I. Gorenstein, and H. Stoecker, "*Hadron yields and fluctuations at energies available at the CERN Super Proton Synchrotron: System-size dependence from Pb+Pb to p+p collisions*", *Phys. Rev. C*, vol. 99, no. 3, p. 034909, 2019. arXiv:1811.10645 [nucl-th].

[40] J. Mohs, S. Ryu, and H. Elfner, "*Particle Production via Strings and Baryon Stopping within a Hadronic Transport Approach*", *J. Phys. G*, vol. 47, no. 6, p. 065101, 2020. arXiv:1909.05586 [nucl-th].

[41] V. Kireyeu, I. Grishmanovskii, V. Kolesnikov, V. Voronyuk, and E. Bratkovskaya, "*Hadron production in elementary nucleon–nucleon reactions from low to ultra-relativistic energies*", *Eur. Phys. J. A*, vol. 56, no. 9, p. 223, 2020. arXiv:2006.14739 [hep-ph].

[42] R. V. Poberezhnyuk, M. Gazdzicki, and M. I. Gorenstein, "*Statistical Model of the Early Stage of nucleus-nucleus collisions with exact strangeness conservation*", *Acta Phys. Polon.*, vol. B46, no. 10, p. 1991, 2015. arXiv:1502.05650 [nucl-th].

[43] M. Mackowiak-Pawlowska [NA61/SHINE], "*Study of the phase diagram of strongly interacting matter in the NA61/SHINE experiment*", *PoS*, vol. PANIC2021, p. 238, 2022. arXiv:2112.01877 [nucl-ex].

[44] E. Schnedermann, J. Sollfrank, and U. W. Heinz, "*Thermal phenomenology of hadrons from 200A GeV S+S collisions*", *Phys. Rev. C*, vol. 48, pp. 2462–2475, 1993. arXiv:nucl-th/9307020.

[45] F. Becattini, J. Manninen, and M. Gazdzicki, "*Energy and system size dependence of chemical freeze-out in relativistic nuclear collisions*", *Phys. Rev.*, vol. C73, p. 044905, 2006. arXiv:hep-ph/0511092 [hep-ph].

[46] X. Lopez *et al.* [FOPI], "*Measurement of $K^*(892)^0$ and $K^0$ mesons in Al+Al collisions at 1.9A GeV*", *Phys. Rev. C*, vol. 81, p. 061902, 2010. arXiv:1006.1905 [nucl-ex].

[47] J. Adamczewski-Musch *et al.* [HADES], "*Sub-threshold production of $K^0_s$ mesons and $\Lambda$ hyperons in Au+Au collisions at $\sqrt{s_{NN}} = 2.4$ GeV*", *Phys. Lett. B*, vol. 793, pp. 457–463, 2019. arXiv:1812.07304 [nucl-ex].

[48] G. Agakishiev *et al.*, "*In-Medium Effects on $K^0$ Mesons in Relativistic Heavy-Ion Collisions*", *Phys. Rev. C*, vol. 82, p. 044907, 2010. arXiv:1004.3881 [nucl-ex].

[49] J. Adam *et al.* [STAR], "*Strange hadron production in Au+Au collisions at $\sqrt{s_{\rm NN}} = 7.7, 11.5, 19.6, 27,$ and 39 GeV*", *Phys. Rev. C*, vol. 102, no. 3, p. 034909, 2020. arXiv:1906.03732 [nucl-ex].

[50] C. Adler *et al.* [STAR], "*Kaon production and kaon to pion ratio in Au+Au collisions at $\sqrt{s_{NN}} = 130$ GeV*", *Phys. Lett. B*, vol. 595, pp. 143–150, 2004. arXiv:nucl-ex/0206008.

[51] M. M. Aggarwal *et al.* [STAR], "*Strange and Multi-strange Particle Production in Au+Au Collisions at $\sqrt{s_{NN}} = 62.4$ GeV*", *Phys. Rev. C*, vol. 83, p. 024901, 2011. arXiv:1010.0142 [nucl-ex].

[52] G. Agakishiev *et al.* [STAR], "*Strangeness Enhancement in Cu+Cu and Au+Au Collisions at $\sqrt{s_{NN}} = 200$ GeV*", *Phys. Rev. Lett.*, vol. 108, p. 072301, 2012. arXiv:1107.2955 [nucl-ex].

[53] C. Strabel, "*Energieabhangigkeit der $K^0_S$-Produktion in zentralen Pb+Pb Reaktionen*". Ph.D. thesis, Johann Wolfgang Goethe-Universitat, 2006, `https://edms.cern.ch/document/2693436/1`.

[54] B. B. Abelev *et al.* [ALICE], "*$K^0_S$ and $\Lambda$ production in Pb-Pb collisions at $\sqrt{s_{NN}} = 2.76$ TeV*", *Phys. Rev. Lett.*, vol. 111, p. 222301, 2013. arXiv:1307.5530 [nucl-ex].

[55] M. Kalisky, "*Reconstruction of charged kaons in the three pion decay channel in Pb+Au 158 AGeV collisions by the CERES experiment*". Ph.D. thesis, Technical University of Darmstadt, 2008, `https://cds.cern.ch/record/1497739`.

[56] M. Gazdzicki and D. Rohrich, "*Strangeness in nuclear collisions*", *Z. Phys. C*, vol. 71, pp. 55–64, 1996. arXiv:hep-ex/9607004.

[57] T. Alber *et al.* [NA35], "*Strange particle production in nuclear collisions at 200 GeV per nucleon*", *Z. Phys. C*, vol. 64, pp. 195–207, 1994.

[58] H. Adhikary *et al.* [NA61/SHINE], "*Report from the NA61/SHINE experiment at the CERN SPS*", tech. rep., CERN, Geneva, 2022, CERN-SPSC-2022-034, SPSC-SR-319, https://cds.cern.ch/record/2839856.

[59] N. Abgrall *et al.* [NA61/SHINE], "*NA61/SHINE facility at the CERN SPS: beams and detector system*", *J. Inst.*, vol. 9, p. P06005, 2014. arXiv:1401.4699 [physics.ins-det].

[60] S. Afanasiev *et al.* [NA49], "*The NA49 large acceptance hadron detector*", *Nucl. Instrum. Meth. A*, vol. 430, pp. 210–244, 1999.

[61] K. Abe *et al.* [T2K], "*The T2K Experiment*", *Nucl. Instrum. Meth. A*, vol. 659, pp. 106–135, 2011. arXiv:1106.1238 [physics.ins-det].

[62] D. S. Ayres *et al.* [NOvA], "*NOvA: Proposal to Build a 30 Kiloton Off-Axis Detector to Study $\nu_\mu \to \nu_e$ Oscillations in the NuMI Beamline*", arXiv:hep-ex/0503053.

[63] A. Acharya *et al.* [NA61/SHINE], "*Addendum to the NA61/SHINE Proposal: A Low-Energy Beamline at the SPS H2*", tech. rep., CERN, Geneva, 2021, CERN-SPSC-2021-028, SPSC-P-330-ADD-12, https://cds.cern.ch/record/2783037.

[64] A. Acharya *et al.* [NA61/SHINE], "*Report from the NA61/SHINE experiment at the CERN SPS*", tech. rep., CERN, Geneva, 2021, CERN-SPSC-2021-027, SPSC-SR-298, https://cds.cern.ch/record/2783036.

[65] J. Abraham *et al.* [Pierre Auger], "*Properties and performance of the prototype instrument for the Pierre Auger Observatory*", *Nucl. Instrum. Meth. A*, vol. 523, pp. 50–95, 2004.

[66] G. Schatz [KASCADE], "*The KASCADE cosmic ray experiment*", *Nucl. Phys. B Proc. Suppl.*, vol. 43, pp. 261–264, 1995.

[67] A. Acharya *et al.* [NA61/SHINE], "*Report from the NA61/SHINE experiment at the CERN SPS*", tech. rep., CERN, Geneva, 2020, CERN-SPSC-2020-023, SPSC-SR-278, https://cds.cern.ch/record/2739340.

[68] A. Aduszkiewicz *et al.* [NA61/SHINE], "*Feasibility Study for the Measurement of Nuclear Fragmentation Cross Sections with NA61/SHINE at the CERN SPS*", tech. rep., CERN, Geneva, 2017, CERN-SPSC-2017-035, SPSC-P-330-ADD-9, https://cds.cern.ch/record/2287004.

[69] N. Amin [NA61/SHINE], "*Results from a Pilot Study on the Measurement of Nuclear Fragmentation with NA61/SHINE at the CERN SPS: $^{11}$C Production in C+p Interactions at 13.5 A GeV/c*", *PoS*, vol. ICRC2021, p. 102, 2021. arXiv:2107.12275 [nucl-ex].

[70] "NA61/SHINE library of images".

[71] C. Bov, R. Maleyran, A. Placci, and M. Placidi, "*The CEDAR (Cerenkov Differential Counters with Achromatic Ring Focus) Project*", *IEEE Transactions on Nuclear Science*, vol. 25, no. 1, pp. 572–576, 1978.

[72] P. Podlaski, "*Study of charged hadron production with tof-dE/dx identification method in central Ar+Sc collisions in NA61/SHINE experiment at CERN*". Ph.D. thesis, University of Warsaw, 2021, https://cds.cern.ch/record/2799198?ln=en.

[73] R. Renfordt [NA61/SHINE], "Introduction to NA61/SHINE Time Projection Chambers". https://indico.cern.ch/event/515331/, Accessed: 13.01.2023.

[74] F. Sauli, "Principles of operation of multiwire proportional and drift chambers". CERN, Geneva, 1977, CERN-77-09, https://cds.cern.ch/record/117989.

[75] G. Charpak and F. Sauli, "*Multiwire proportional chambers and drift chambers*", *Nucl. Instrum. Meth. A*, vol. 162, no. 1, pp. 405–428, 1979.

[76] B. Abelev *et al.* [ALICE], "*Upgrade of the ALICE Time Projection Chamber*", tech. rep., CERN, Geneva, 2013, CERN-LHCC-2013-020, ALICE-TDR-016, https://cds.cern.ch/record/1622286.

[77] B. Rumberger *et al.*, "*The Forward TPC system of the NA61/SHINE experiment at CERN: a tandem TPC concept*", *J. Inst.*, vol. 15, no. 07, p. P07013, 2020. arXiv:2004.11358 [physics.ins-det].

[78] W. Brylinski [NA61/SHINE], "*Charm physics in NA61/SHINE*", *PoS*, vol. HardProbes2018, p. 156, 2019.

[79] W. Brylinski [NA61/SHINE], "*News from the strong interactions program of NA61/SHINE*", *EPJ Web Conf.*, vol. 258, p. 05007, 2022.

[80] A. Aduszkiewicz *et al.* [NA61/SHINE], "*Report from the NA61/SHINE experiment at the CERN SPS*", tech. rep., CERN, Geneva, 2018, CERN-SPSC-2018-029, SPSC-SR-239, https://cds.cern.ch/record/2642286.

[81] A. Dorokhov *et al.*, "*High resistivity CMOS pixel sensors and their application to the STAR PXL detector*", *Nucl. Instrum. Meth. A*, vol. 650, no. 1, pp. 174–177, 2011.

[82] M. Deveaux *et al.*, "*Radiation tolerance of a column parallel CMOS sensor with high resistivity epitaxial layer*", *J. Inst.*, vol. 6, no. 02, pp. C02004–C02004, 2011.

[83] G. Aglieri Rinella [ALICE], "*The ALPIDE pixel sensor chip for the upgrade of the ALICE Inner Tracking System*", *Nucl. Instrum. Meth. A*, vol. 845, pp. 583–587, 2017.

[84] A. Aduszkiewicz *et al.* [NA61/SHINE], "*Beam momentum scan with Pb+Pb collisions*", tech. rep., CERN, Geneva, 2015, CERN-SPSC-2015-038, SPSC-P-330-ADD-8, https://cds.cern.ch/record/2059811.

[85] A. Aduszkiewicz, "*Energy dependence of negatively charged pion production in proton-proton interactions at the CERN SPS*". Ph.D. thesis, University of Warsaw, 2015, https://cds.cern.ch/record/2135329.

[86] K. Werner, "*The hadronic interaction model EPOS*", *Nuclear Physics B - Proceedings Supplements*, vol. 175-176, pp. 81–87, 2008.

[87] R. Brun, R. Hagelberg, M. Hansroul, and J. C. Lassalle, "*Geant: Simulation Program for Particle Physics Experiments. User Guide and Reference Manual*", tech. rep., CERN, Geneva, 1978, CERN-DD-78-2-REV, CERN-DD-78-2, `https://cds.cern.ch/record/118715`.

[88] D. Banas, A. Kubala-Kukus, M. Rybczynski, I. Stabrawa, and G. Stefanek, "*Influence of target material impurities on physical results in relativistic heavy-ion collisions*", *Eur. Phys. J. Plus*, vol. 134, no. 1, p. 44, 2019.

[89] A. Acharya *et al.* [NA61/SHINE], "*Measurements of $\pi^-$ production in $^7$Be+$^9$Be collisions at beam momenta from 19A to 150AGeV/c in the NA61/SHINE experiment at the CERN SPS*", *Eur. Phys. J. C*, vol. 80, no. 10, p. 961, 2020 [Erratum: *Eur. Phys. J.* C 81, 144, 2021]. arXiv:2008.06277 [nucl-ex].

[90] E. Kaptur, "*Analysis of collision centrality and negative pion spectra in $^7$Be+$^9$Be interactions at CERN SPS energy range*". Ph.D. thesis, University of Silesia, 2017, `https://edms.cern.ch/document/2004086/1`.

[91] A. Seryakov [NA61/SHINE], "PSD acceptance maps for event selection". `https://edms.cern.ch/document/1867336/1`.

[92] A. Bialas, M. Bleszynski, and W. Czyz, "*Multiplicity Distributions in Nucleus-Nucleus Collisions at High-Energies*", *Nucl. Phys. B*, vol. 111, pp. 461–476, 1976.

[93] "*RooFit*". `https://root.cern/manual/roofit/`, Accessed: 23.09.2022.

[94] K. Werner, L. Karpenko, M. Bleicher, and T. Pierog, "*The Physics of EPOS*", *EPJ Web Conf.*, vol. 52, p. 05001, 2013.

[95] J. Mohs, S. Ryu, and H. Elfner, "*Particle Production via Strings and Baryon Stopping within a Hadronic Transport Approach*", *J. Phys. G*, vol. 47, no. 6, p. 065101, 2020.

[96] J. Weil *et al.*, "*Particle production and equilibrium properties within a new hadron transport approach for heavy-ion collisions*", *Phys. Rev. C*, vol. 94, no. 5, p. 054905, 2016.

[97] H. Adhikary *et al.* [NA61/SHINE], "*Measurements of $\pi^{\pm}$, $K^{\pm}$, $p$ and $\bar{p}$ spectra in $^{40}$Ar+$^{45}$Sc collisions at beam momenta from 13A to 150A GeV/c with the NA61/SHINE spectrometer at the CERN SPS*", *paper in preparation*.

[98] B. I. Abelev *et al.* [STAR], "*Systematic measurements of identified particle spectra in pp, $d$+$Au$ and $Au$+$Au$ collisions from STAR*", *Phys. Rev. C*, vol. 79, p. 034909, 2009. arXiv:0808.2041 [nucl-ex].

[99] B. Abelev *et al.* [ALICE], "*Centrality dependence of $\pi$, K, p production in Pb-Pb collisions at $\sqrt{s_{NN}}$ = 2.76 TeV*", *Phys. Rev. C*, vol. 88, p. 044910, 2013. arXiv:1303.0737 [hep-ex].

[100] J. Adamczewski-Musch *et al.* [HADES], "*Deep sub-threshold $\phi$ production in Au+Au collisions*", *Phys. Lett. B*, vol. 778, pp. 403–407, 2018. arXiv:1703.08418 [nucl-ex].

[101] G. Agakishiev *et al.* [HADES], "*$\phi$ decay: A Relevant source for $K^-$ production at SIS energies?*", *Phys. Rev. C*, vol. 80, p. 025209, 2009. arXiv:0902.3487 [nucl-ex].

[102] P. Gasik *et al.* [FOPI], "*Strange meson production in Al+Al collisions at 1.9A GeV*", *Eur. Phys. J. A*, vol. 52, no. 6, p. 177, 2016. arXiv:1512.06988 [nucl-ex].

[103] W. Brylinski, M. Gazdzicki, F. Giacosa, M. Gorenstein, R. Poberezhnyuk, S. Samanta, and H. Stroebele, "*Large isospin symmetry breaking in heavy ion collisions*", *paper in preparation*.

[104] S. A. Bass *et al.*, "*Microscopic models for ultrarelativistic heavy ion collisions*", *Prog. Part. Nucl. Phys.*, vol. 41, pp. 255–369, 1998. arXiv:nucl-th/9803035.

[105] M. Bleicher *et al.*, "*Relativistic hadron hadron collisions in the ultrarelativistic quantum molecular dynamics model*", *J. Phys. G*, vol. 25, pp. 1859–1896, 1999. arXiv:hep-ph/9909407.

[106] M. Bleicher and E. Bratkovskaya, "*Modelling relativistic heavy-ion collisions with dynamical transport approaches*", *Prog. Part. Nucl. Phys.*, vol. 122, p. 103920, 2022.

[107] A. Aduszkiewicz *et al.* [NA61/SHINE], "*Study of Hadron-Nucleus and Nucleus-Nucleus Collisions at the CERN SPS: Early Post-LS2 Measurements and Future Plans*", tech. rep., CERN, Geneva, 2018, CERN-SPSC-2018-008, SPSC-P-330-ADD-10, `https://cds.cern.ch/record/2309890`.

[108] A. P. Kostyuk, M. I. Gorenstein, H. Stoecker, and W. Greiner, "*Statistical coalescence model analysis of $J/\psi$ production in Pb+Pb collisions at 158 A GeV*", *Phys. Lett.*, vol. B531, pp. 195–202, 2002. arXiv:hep-ph/0110269 [hep-ph].

[109] O. Linnyk, E. L. Bratkovskaya, and W. Cassing, "*Open and hidden charm in proton-nucleus and heavy-ion collisions*", *Int. J. Mod. Phys.*, vol. E17, pp. 1367–1439, 2008. arXiv:0808.1504 [nucl-th].

[110] R. V. Gavai, S. Gupta, P. L. McGaughey, E. Quack, P. V. Ruuskanen, R. Vogt, and X.-N. Wang, "*Heavy quark production in $pp$ collisions*", *Int. J. Mod. Phys.*, vol. A10, pp. 2999–3042, 1995. arXiv:hep-ph/9411438 [hep-ph].

[111] P. Braun-Munzinger and J. Stachel, "*(Non)thermal aspects of charmonium production and a new look at $J/\psi$ suppression*", *Phys. Lett.*, vol. B490, pp. 196–202, 2000. arXiv:nucl-th/0007059 [nucl-th].

[112] P. Levai, T. S. Biro, P. Csizmadia, T. Csorgo, and J. Zimanyi, "*The Production of charm mesons from quark matter at CERN SPS and RHIC*", *J. Phys.*, vol. G27, pp. 703–706, 2001. arXiv:nucl-th/0011023 [nucl-th].

[113] R. V. Poberezhnyuk, M. Gazdzicki, and M. I. Gorenstein, "*Open charm production in central Pb+Pb collisions at the CERN SPS: statistical model estimates*", *Acta Phys. Polon.*, vol. B48, p. 1461, 2017. arXiv:1708.04491 [nucl-th].

[114] M. C. Abreu *et al.* [NA50], "*Evidence for deconfinement of quarks and gluons from the $J/\psi$ suppression pattern measured in Pb + Pb collisions at the CERN SPS*", *Phys. Lett.*, vol. B477, pp. 28–36, 2000.

[115] "*C++*". https://en.cppreference.com/w/, Accessed: 23.09.2022.

[116] "*ZeroMQ*". https://zeromq.org/, Accessed: 23.09.2022.

[117] "*influxDB*". https://www.influxdata.com/, Accessed: 23.09.2022.

[118] "*Grafana*". https://grafana.com/, Accessed: 23.09.2022.

[119] H. Adhikary *et al.* [NA61/SHINE], "*Addendum to the NA61/SHINE Proposal: Request for oxygen beam in Run 3*", tech. rep., CERN, Geneva, 2022, CERN-SPSC-2022-021, SPSC-P-330-ADD-13, https://cds.cern.ch/record/2810689.